The role of the chloride-proton exchanger 3

ClC-3 in pain perception

Inaugural-Dissertation

zur Erlangung des Doktorgrades

der Mathematisch-Naturwissenschaftlichen Fakultät

der Heinrich-Heine-Universität Düsseldorf

vorgelegt von

Juan David Sierra Márquez

aus Sampués, Kolumbien

Jülich, März 2021

aus dem Institut für Biologische Informationsprozesse 1 (IBI-1)

des Forschungszentrums Jülich

und der Mathematisch-Naturwissenschaftlichen Fakultät

der Heinrich-Heine-Universität Düsseldorf

Gedruckt mit der Genehmigung der

Mathematisch-Naturwissenschaftlichen Fakultät der

Heinrich-Heine-Universität Düsseldorf

Berichterstatter:

Referent: Prof. Dr. Christoph Fahlke

Korreferent: Prof. Dr. Christine R. Rose

Tag der mündlichen Prüfung: 05. Juli 2021

Dedicated to my family

Contents

List of figures

List of tables

HEINRICH-HEINE-UNIVERSITÄT DÜSSELDORF

Abstract

The role of the chloride-proton exchanger 3 ClC-3 in pain perception

The chloride transport activity, the main function of intracellular Cl^-/H^+ exchangers, is evolutionary conserved and regulates a variety of physiological processes. It supports the acidification of intracellular organelles by regulating luminal chloride homeostasis. ClC-3 is highly expressed in the central nervous system (CNS) and the peripheral nervous system (PNS). *Clcn3*$^{-/-}$ mouse model shows severe neurodegeneration and exhibits a behavioral phenotype of hyperalgesia, highlighting the physiological relevance of this transporter within both systems. This work studied the role of ClC-3 in regulating pain perception using the *Clcn3*$^{-/-}$ mouse model. *Clcn3*$^{-/-}$ animals display hyperalgesia for high-threshold thermal and chemical noxious stimuli. Dorsal root ganglion (DRG) neurons from mutant mice show enhanced neuronal excitability due to altered Na^+ and K^+ current densities. Moreover, neuronal degeneration was neither observed in the DRG nor the dorsal horn of the spinal cord (DHSC) of *Clcn3*$^{-/-}$. However, the increased expression of CC-chemokine ligand 2 (CCL2), accompanied by the detection of reactive microglia, suggests a central sensitization. To study the importance of Cl^-/H^+ activity of ClC-3 in neuronal excitability, a double mutant mouse model *Clcn3*^{E281Q}/*Clcn4*$^{-/-}$ was generated. These mice are virtually devoid of any ClC-3/4-mediated chloride transport. *Clcn3*^{E281Q}/*Clcn4*$^{-/-}$ mice show no signs of altered neuronal excitability. Action potential properties were not different from the control condition, suggesting a function that is independent of the protein exchanger activity of ClC-3. This work demonstrates the importance of ClC-3 in hyperalgesia and reports a novel unexpected function for ClC-3 that is essential to maintain the intrinsic electrical properties of sensory neurons.

Zusammenfassung

Die Rolle des Chlorid-Protonen-Austauschers 3 ClC-3 bei der Schmerzwahrnehmung

Die Chlorid-Transportaktivität, die Hauptfunktion des intrazellulären Cl-/H+-Austauschers, ist evolutionär konserviert und reguliert eine Vielzahl von physiologischen Prozessen. Sie unterstützt die Ansäuerung der intrazellulären Organellen, indem sie die luminale Chlorid-Homöostase reguliert. ClC-3 ist im Zentralnervensystem (ZNS) und im peripheren Nervensystem (PNS) hoch exprimiert. Das *Clcn3*$^{-/-}$ Mausmodell zeigt schwere Neurodegeneration und weist einen Verhaltensphänotyp der Hyperalgesie auf, was die physiologische Relevanz dieses Transporters in beiden Systemen verdeutlicht. In dieser Arbeit wurde die Rolle von ClC-3 bei der Regulierung der Schmerzwahrnehmung anhand des *Clcn3*$^{-/-}$ Mausmodells untersucht. *Clcn3*$^{-/-}$ Tiere zeigen Hyperalgesie für überschwellige, thermische und chemische schädliche Reize. Neuronen des Dorsalwurzelganglions (DRG) von mutierten Mäusen zeigen eine erhöhte neuronale Erregbarkeit aufgrund von veränderten Na^+ und K^+ Stromdichten. Außerdem wurde weder im DRG noch im Dorsalhorn des Rückenmarks (DHSC) von *Clcn3*$^{-/-}$ eine neuronale Degeneration beobachtet. Die erhöhte Expression von CC-Chemokin-Ligand 2 (CCL2), begleitet vom Nachweis reaktiver Mikroglia, deutet jedoch auf eine zentrale Sensibilisierung hin. Um die Bedeutung der Cl^-/H^+-Aktivität von ClC-3 für die neuronale Erregbarkeit zu untersuchen, wurde ein doppelt mutiertes Mausmodell *Clcn3*^{E281Q}/ *Clcn4*$^{-/-}$ generiert. Bei diesen Mäusen fehlt praktisch jeglicher ClC-3/4-vermittelter Chlorid Transport. *Clcn3*^{E281Q}/*Clcn4*$^{-/-}$ Mäuse zeigen keine Anzeichen einer veränderten neuronalen Erregbarkeit. Die Eigenschaften des Aktionspotentials unterschieden sich nicht von der Kontrollbedingung, was auf eine Funktion hindeutet, die unabhängig von der Protein-Austauscher-Aktivität von ClC-3 ist. Diese Arbeit zeigt die Bedeutung von ClC-3 bei Hyperalgesie und berichtet über eine neuartige, unerwartete Funktion für ClC-3, die für die Aufrechterhaltung der intrinsischen elektrischen Eigenschaften sensorischer Neuronen wesentlich ist.

Chapter 1. Introduction

1.1 Overview of CLC Family

Chloride channels and transporters are expressed in various cell types from bacteria to humans. They have a well-conserved molecular architecture and are structurally unrelated to other known ion channels. They fulfill many different cellular functions, ranging from the stabilization of the resting potential, transport of salts across epithelia in kidneys to the acidification of intracellular organelles (Chen, 2004; Dutzler, 2006; Jentsch and Pusch, 2018).

ClC-0 was the first member of the CLC family to be cloned from the electric organ of *Torpedo californica* (Jentsch et al., 1990). Thereafter, nine members were identified in mammalian cells, which are divided into two groups, the chloride channels ClC-1, ClC-2, ClC-Ka, and ClC-Kb (Chen, 2004; Jentsch and Pusch, 2018), and the transporters ClC-3, ClC-4, ClC-5, ClC-6 and ClC-7. Intra- and extracellular Cl^- concentrations, as well as the pH, affect the function and gating properties of the CLC channels that are present at the plasma membrane. In skeletal muscle cells, ClC-1 contributes to the resting membrane conductance and plays an important role in membrane repolarization (Pedersen et al., 2016) and transepithelial transport on the kidney and inner ear (Gradogna and Pusch, 2010; Simon et al., 1997).

CLC transporters can be found in intracellular membrane systems and function as anion/proton exchangers. ClC-3, ClC-4, and ClC-5 reside along of the whole endosomal/lysosomal system (Guzman et al., 2017; Guzman et al., 2013; Guzman et al., 2015; Picollo and Pusch, 2005). They share a high degree of sequence similarities ~80%, but have only 30% amino acid identity to other members of the gene family (Chen, 2004; Steinmeyer et al., 1995). The last branch of anion/proton exchangers is composed of ClC-6 and ClC-7, which share ~40% sequence identity, but only around 25–30% with the other CLC members. These exchangers are ubiquitous but predominantly found in the brain (Steinmeyer et al., 1995). This classification is represented in Figure 1.1.

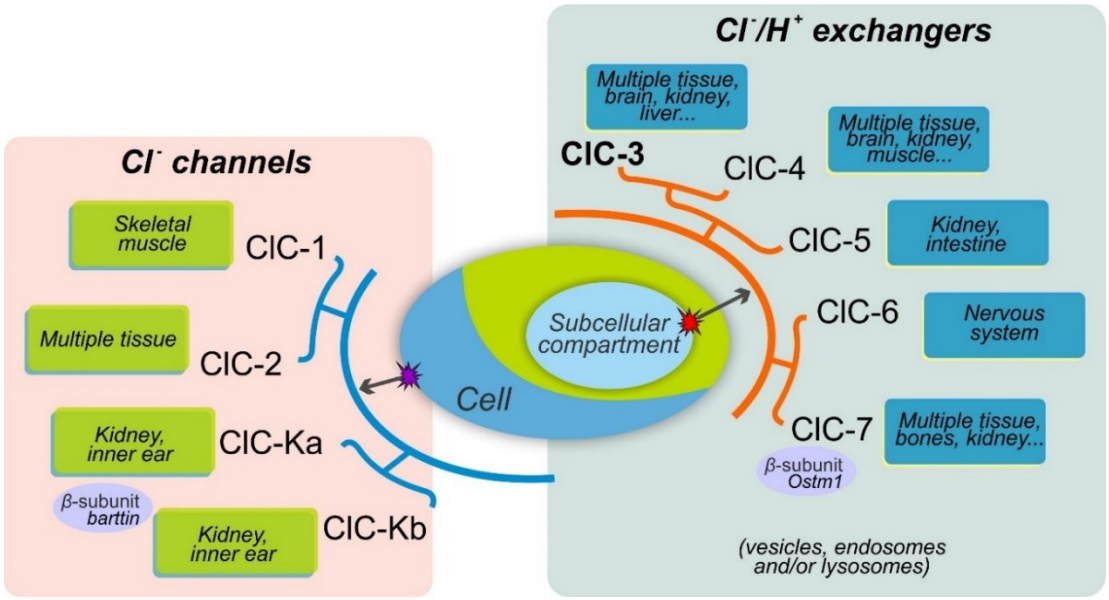

Figure 1.1. Schematic representation of the CLC family of anion channels and transporters and their cellular localization. Two groups can be identified, the first group is formed by ClC-1, CLC-2, ClC-Ka, and ClC-Kb proteins that are situated at the plasma membrane and work as anion channels. The second group of CLC proteins is composed of the anion/proton exchangers ClC-3 to ClC-7, localized to intracellular organelles. The figure was drawn with the information obtained from Jentsch and Pusch (2018).

1.2 Importance of the intracellular ClC transporters

Cl^-/H^+ antiporters localize to intracellular organelles, such as large dense-core vesicles, endosomes, lysosomes, and to a lesser extent in synaptic vesicles, (Accardi and Miller, 2004; Guzman et al., 2013; Taoufiq et al., 2020). They have been proposed to fulfill diverse sub-cellular functions by controlling the pH and Cl^- concentration in the intracellular compartments where they reside. The physiological importance of these transporters is highlighted by Cl^-/H^+ knock-out animal models as well as by naturally occurring mutations in CLCN genes (Hu et al., 2016; Li et al., 2019a; Palmer et al., 2018; Poët et al., 2006; Thakker, 1998) that lead to impaired function in different tissue, neuronal degeneration, and numerous neurological disorders.

1.2.1 ClC-3

ClC-3 is ubiquitously expressed and shares about 80% sequence identity with ClC-4 and ClC-5 (Steinmeyer et al., 1995). In humans, it is encoded in the 4th chromosome (chr4:169620521-169723187), and in mice in the 8th chromosome (Chr8:60910389-60983300 bp), accession code NC_000074.6 from the National Center for Biotechnology Information. *CLCN3* mouse gene splices in different variants with different lengths and compositions of the

N- and C-terminal amino acid sequences. ClC-3a, ClC-3b, ClC-3c, and ClC-3e have been identified in mammalians, however, six spliced gene products are predicted, ClC-3a to ClC-3f in total (Borsani et al., 1995; Guzman et al., 2015; Ogura et al., 2002). The sequence differences of these variants are illustrated in Figure 1.2.

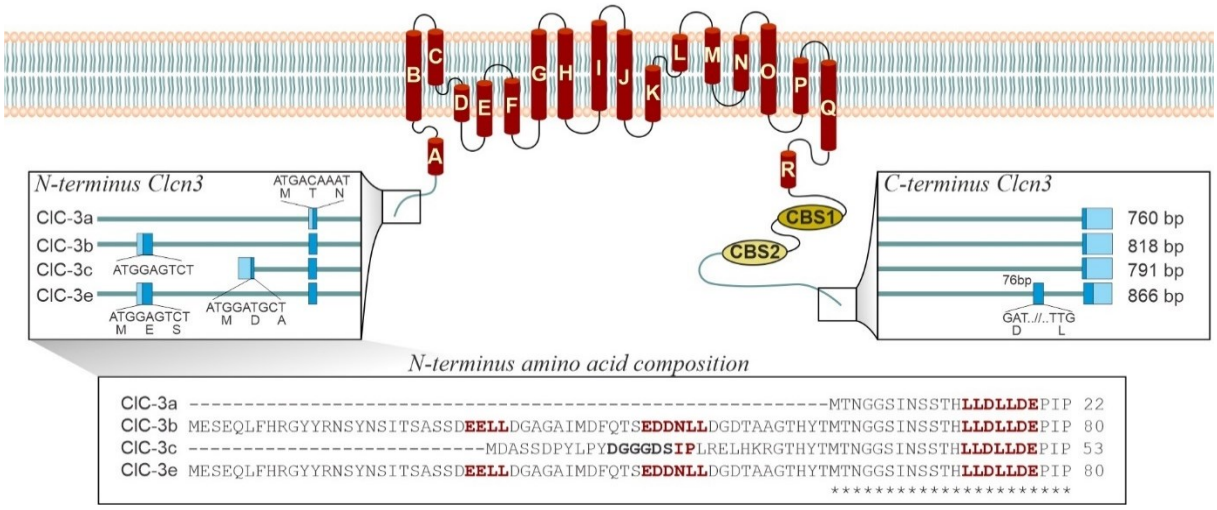

Figure 1.2. Membrane topology of the ClC-3 and the amino acid composition in the N- and C-terminus show various dileucine clathrin binding motifs among the splice variants. ClC-3a (Genebank Nr. NM_007711.3), ClC-3b (Genebank Nr. NM_173873.1), ClC-3c (Genebank Nr. NM_173876.3), and ClC-3e (Genebank Nr. NM_173874.1).

The splicing in the N-terminal region of these variants modifies their subcellular distribution. Guzman et al (2015), showed that upon heterologous expression ClC-3a and -3b exhibit a similar distribution pattern to the lysosomal marker LAMP1 and ClC-3c shows a high degree of co-localization with recycling endosomal markers RAB11 and TfR. ClC-3c can also be found on the plasma membrane upon overexpression in HEK 293T cells.

1.2.1.1 ClC-3 in the central nervous system (CNS)

Clcn3$^{-/-}$ mice show a severe phenotype characterized by progressive postnatal degeneration of the retina and hippocampus which is evidenced shortly before the third postnatal week of development. By 12 months of age, the hippocampal formation is completely lost (Figure 1.3) (Stobrawa et al., 2001). *Clcn3*$^{-/-}$ mice are smaller than littermates. They show a pronounced abnormal wedge-shaped of the upper back of the vertebrae, a condition called kyphosis, and enhanced motor activity. Despite these severe phenotype effects, the animal is viable for more than a year.

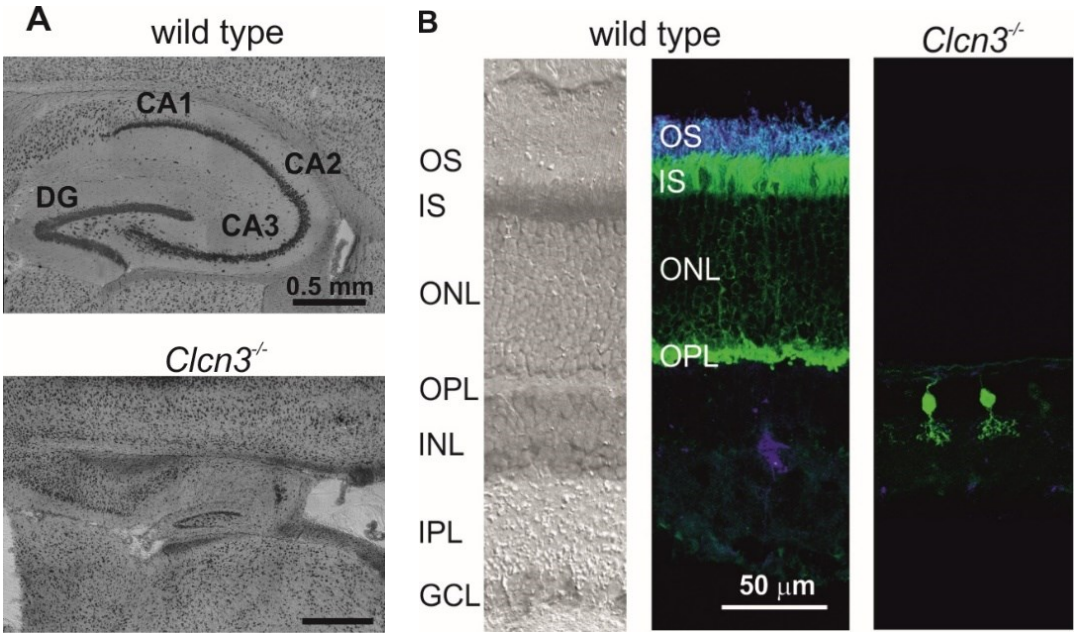

Figure 1.3. Histological analysis shows massive hippocampal, as well as retinal degeneration in the *Clcn3*$^{-/-}$ mice at P60. A. Nissl staining of the different regions of the hippocampus shows no identifiable structures in mutant mice. B. *Clcn3*$^{-/-}$ animals show only selective loss of the photoreceptors. OS: outer segments, IS: inner segments, ONL: outer nuclear layer, OPL: outer plexiform layer, INL: inner nuclear layer, IPL, inner plexiform layer: GCL: Ganglion cell layer. The confocal pictures were taken by Dr. Jana Gehlen from the Institute for Biological Information Processing (IBI-1).

The underlying mechanisms by which the absence of ClC-3 leads to neurodegeneration are so far not known, however, the high expression levels of both ClC-3 and ClC-4 in the hippocampal region suggest a fundamental role of Cl^-/H^+ in the maintenance of neuronal viability. Several hypotheses have been postulated referring to the molecular and physiological function of the ClC-3 in the CNS at pre-and postsynaptic levels. From the postsynaptic site, it is thought to regulate neuronal excitability by enhancing the time course of N-methyl-D-aspartate (NMDA) receptor-mediated miniature excitatory postsynaptic potentials (mEPSPs) (Wang et al., 2006). Moreover, electrophysiological recordings on hippocampal slices in the CA1 region from young animals showed a substantial decrease in the amplitude and frequency of miniature inhibitory postsynaptic currents (mIPSC) inferring that ClC-3 might affect GABAergic synaptic transmission in the hippocampus (Riazanski et al., 2011).

Lately, our group showed that ClC-3 modulates fast excitatory synaptic transmission by regulating the amount of neurotransmitter as well as the release probability of synaptic vesicles (SV). These conclusions were drawn after observing a significant increment in the amplitude

and frequency of miniature excitatory postsynaptic currents (mEPSC) as well as the amplitudes of action-potential evoked EPSCs in hippocampal cultures from newborn *Clcn3*$^{-/-}$ mice (Guzman et al., 2014). Together, this evidence suggests that ClC-3 plays a fundamental role in hippocampal neuronal excitability, providing an important level of regulation in the modulation of synaptic communication. Despite these important findings, the underline molecular mechanism by which ClC-3 regulates neuronal excitability remains unclear.

1.2.1.2 ClC-3 in neuroendocrinal tissue

ClC-3 is also found in the neuroendocrinal system (Deriy et al., 2009; Li et al., 2009; Maritzen et al., 2008) and its function here has been difficult to demonstrate in part due to the absence of experimental correlation between functional and co-localization data. Moreover, the lack of commercially available antibodies that allow differentiation of the different ClC-3 splice variants, has hindered an assignment of a role of ClC-3 in neurosecretion. Data from *Clcn3*$^{-/-}$ chromaffin and beta-pancreatic cells suggest a contribution of this transporter in the establishment of vesicles for exocytosis and the regulation of their catecholamine content (Maritzen et al., 2008; Wang et al., 2006).

Recently, co-localization experiments using a lentivirus-mediated expression of the ClC-3 splice variants in chromaffin cells demonstrate the presence of ClC-3c to secretory vesicles that are positive for VAMP3/cellubrevin, VAMP4, chromogranin A and neuropeptide Y, markers for LDCVs. This finding is in accordance with previous studies that state the presence of ClC-3 in insulin-containing LDCV in pancreatic β-cells (Deriy et al., 2009; Li et al., 2009) but apparently in disagreement with earlier reports (Maritzen et al., 2008) that claimed the absence of ClC-3 on LDCVs. The discrepancy most probably originates from using different experimental strategies. While Deriy (2009) and Li (2009) used a self-made antibody that does not differentiate between splice variants, Maritzen (2008) used Semliki-Forest-Virus to mediate the expression of ClC-3b, the lysosomal splice variant. Indeed, we confirmed the presence of ClC-3b in lysosomes in chromaffin cells. Additionally, capacitance measurements showed defective granular exocytosis in mouse chromaffin as well as in pancreatic β-cells from *Clcn3*$^{-/-}$ mice (Deriy et al., 2009; Li et al., 2009; Maritzen et al., 2008). Combining carbon fiber amperometry to estimate the granular catecholamine content with rescue experiments, it was demonstrated that ClC-3c but not ClC-3b or ClC-5, was able to rescue the catecholamine content of secretory granules in perfect correlation with the co-localization data. From this

research it can be concluded that genetic ablation of ClC-3 not only reduces the catecholamine content of secretory granules but also contribute to the establishment of vesicles for exocytosis in wild type chromaffin cells (Comini, M., **Sierra-Marquez J**., *et al*, *EMBO reports*, in revision).

1.2.1.3 ClC-3 in the peripheral nervous system (PNS)

Intracellular Cl^-/H^+ exchangers are highly expressed in the PNS; however, their function in sensory neurons is poorly understood. A recent report links ClC-3 with a role in nociception. The report shows that a rat model of mechanical hypersensitivity after spared nerve injury (SNI) recovered normal nociceptive response by intrathecal injection of adenovirus harboring ClC-3. Moreover, *Clcn3*$^{-/-}$ mouse model showed decreased mechanical sensitivity but no changes in paw withdrawal latencies induced by heat or chemical stimulation were observed. Using electrophysiological experiments, the authors found significant changes in the properties of the action potential (AP) from *Clcn3*$^{-/-}$ dorsal root ganglion (DRG) neuronal cultures. They reported a reduction in the rheobase and voltage thresholds accompanied by an increase in the input resistance of the membrane, and the frequency of action potentials (Pang et al., 2016). This evidence indicates that Cl^-/H^+ exchangers, ClC-3 in this case, play an important role in the development and/or in the regulation of nociception. However, it is still unclear how an intracellular chloride transporter regulates the electrical properties of sensory neurons.

1.2.2 ClC-4

ClC-4 is expressed in different tissue including skeletal muscle, liver, kidney, intestine, heart, and with high expression within the CNS. ClC-4 is a strongly outwardly rectifying $2Cl^-/H^+$ exchanger with similar biophysical properties to its homologs ClC-3 and ClC-5 (Alekov and Fahlke, 2009; Guzman et al., 2013). It is thought to fulfill a similar function as ClC-3 and ClC-5 by regulating pH in endosomes (Mohammad-Panah et al., 2003); however, homodimers of ClC-4 are highly retained in the endoplasmic reticulum (Okkenhaug et al., 2006). Our group has recently shown that ClC-3 targets ClC-4 to different endosomal/lysosomal compartments where the different splice variants of ClC-3 are localized (Guzman et al., 2017). This evidence implies that ClC-4 may not work independently but only by association with ClC-3(Guzman et al., 2014; Jentsch and Pusch, 2018).

The physiological role of ClC-4 is less known, in part due to the lack of phenotype upon disruption of the *Clcn4* gene in mice (Rickheit et al., 2010). However, in humans naturally

occurring *CLCN4* mutations have been associated with different neurological problems. For example, the G544R mutation identified in 2013 was implicated in intellectual disability and refractory early-onset epileptic encephalopathy (Veeramah et al., 2013). Later, N15SFs*18, G731R, L221V, V536M, and G78S were associated with epilepsy, dysmorphic face, scoliosis, and strabismus (Hu et al., 2016). Since then, a growing number of mutations that very likely affect ClC-4 function has been reported (Palmer et al., 2018). Recently, three newly reported ClC-4 mutations V455I, T532K, and L625F have been characterized. These mutations lead to a loss of function of ClC-4 and are associated with early-onset epileptic encephalopathy, intellectual disability, language delay, behavioral disorders, and dysmorphic features (He, H., … **Sierra-Marquez et al.,** *Epilepsia*, in revision). These new related diseases point out an essential physiological role for ClC-4 within the CNS.

1.2.3 ClC-5

The physiological function of ClC-5 is best understood among ClC-3 and ClC-4. It mediates outwardly rectifying chloride currents that are activated by strong depolarizing voltages (Picollo and Pusch, 2005; Smith and Lippiat, 2010). Furthermore, ClC-5 might also associate with other transporters like ClC-3 or ClC-4 (Suzuki et al., 2006). Mutations on the *CLCN5* human gene cause Dent's disease, an X-linked renal disorder characterized by proteinuria, hyperphosphaturia, and hypercalciuria (Lloyd et al., 1996) (Gianesello et al., 2020; Günther et al., 2003; Piwon et al., 2000; Smith et al., 2009; Wright et al., 2008). A similar phenotype is observed in the *Clcn5*$^{-/-}$ mouse model. *Clcn5*$^{-/-}$ mice show an endocytosis defect in the renal proximal tubules, a segment of the nephron responsible for the reabsorption of small molecules. ClC-5 function is crucial to maintain the Cl^- and H^+ homeostasis in endosomes where it resides (Günther et al., 1998; Mohammad-Panah et al., 2003; Piwon et al., 2000), to regulate the trafficking and processing of the megalin/cubilin endocytic receptor complex, and other proteins as the sodium/proton exchanger NHE3 and the sodium/phosphate cotransporter NPT2a (Christensen et al., 2003; Moulin et al., 2003a; Piwon et al., 2000).

1.2.4 Other ClC exchangers

Other CLC exchangers have been associated with different neurological disorders. For example, ClC-6 is expressed in endosomes of neuronal cell bodies in the CNS and the PNS. Upon deletion, *Clcn6*$^{-/-}$ shows a mild form of lysosomal storage disease called neuronal ceroid lipofuscinosis (NCL), characterized by an axonal accumulation of lipofuscin, a material that

causes swelling of proximal axons. Additionally, *Clcn6*$^{-/-}$ mice show a pronounced decrease in pain sensitivity upon thermal noxious stimuli, indicating a role in nociception (Poët et al., 2006). More recently, a gain-of-function mutation, Y533C in the *CLCN6* gene has been associated with an early onset of neurodegeneration (Polovitskaya et al., 2020). Finally, data obtained from *Clcn7*$^{-/-}$ mice suggest that ClC-7 plays an important role in the maintenance and neuronal viability and for osteoclast-mediated bone reabsorption (Kornak et al., 2001; Poët et al., 2006).

1.3 Neuropathic pain

According to the **I**nternational **A**ssociation for the **S**tudy of **P**ain (IASP), pain can be defined as "An unpleasant sensory and emotional experience associated with, or resembling, actual or potential tissue damage" and can be influenced by biological, psychological, and social factors (IASP Task Force on Taxonomy, 1994). Pain is perceived by the nociceptors, which are high-threshold sensory receptors of the peripheral somatosensory nervous system that are capable of transducing and encoding noxious stimuli (IASP Task Force on Taxonomy, 1994). These neurons express a variety of ion channels that function as molecular sensors to detect temperature, mechanical or chemical noxious or non-noxious stimuli, and to convert them into action potentials or electrical signals (Oh and Jung, 2020).

1.3.1 Contribution of ion channels in nociception

Ligand-gated and voltage-gated ion channels have a crucial role in the detection, generation, and transmission of high-threshold stimuli by nociceptors (Bennett and Woods, 2014). Peripheral nerve endings express chemo-, mechano-, and thermosensitive ion channels such as transient receptor potential channels (TRPs), acid-sensitive ion channels (ASIC), adenosine triphosphate (ATP) gated ion channels (P2X) among others (Khan et al., 2019; Marics et al., 2014). Other receptors such as GABA-, Glycine- (in immature neurons), Glutamate-, receptors as well as Ca^{2+}-activated Cl^- channel (TMEM16A) can depolarize the nociceptors, resulting in excitation of the sensory neurons. The depolarization of the nerve terminals generates potential differences that are converted into action potentials by voltage-gated Na^+ and Ca^{2+} channels (Dubin and Patapoutian, 2010; Oh and Jung, 2020).

Mammalian voltage-gated sodium channels exhibit a 220- to 260-kDa alpha subunit that encompasses the conduction pore and the gating machinery. Nine known genes coding for sodium channels have been identified, and many of them have been implicated in nociceptive

pain. These isoforms are $Na_v1.1$, $Na_v1.2$, $Na_v1.3$, $Na_v1.4$, $Na_v1.5$, $Na_v1.6$, $Na_v1.7$, $Na_v1.8$, $Na_v1.9$. In mammals, isoforms of these channels are expressed in different tissue including the PNS, where almost all of them can be found except for $Na_v1.4$. Some of them such as $Na_v1.7$, $Na_v1.8$, $Na_v1.9$ are preferentially expressed in nociceptive neurons making them important targets for potential analgesics (Cummins et al., 2019; Goldin et al., 2000). Changes in the surface expression or their biophysical properties have been associated with several nociceptive disorders. For example, $Na_v1.7$-A1632G or I848T gain-of-function mutations lead to inherited erythromelalgia, a disorder in which render dorsal root ganglia (DRG) neurons hyperexcitable due to a reduction voltage threshold of the action potential firing where $Na_v1.7$ plays a key role (Meents et al., 2019; Yang et al., 2016) (Figure 1.4). On the other hand, loss of function mutations on the $Na_V1.7$ and $Na_V1.9$ are associated with congenital insensitivity to pain (Bennett and Woods, 2014; Goldberg et al., 2007), and the downregulation of the SCN9A, the gene encoding the $Na_V1.7$ inhibits the activation of astrocytes and microglia in rats model of cancer pain (Pan et al., 2015). While $Na_v1.8$ a channel is crucial for transmission of nociceptive information because it carries most of the current underlying the depolarizing phase of the action potential, dysregulation in this channel can contribute to neuropathic pains, mall-fiber neuropathy which consists of persistent burning pain, Brugada syndrome, and kidney stone diseases (Bennett and Woods, 2014).

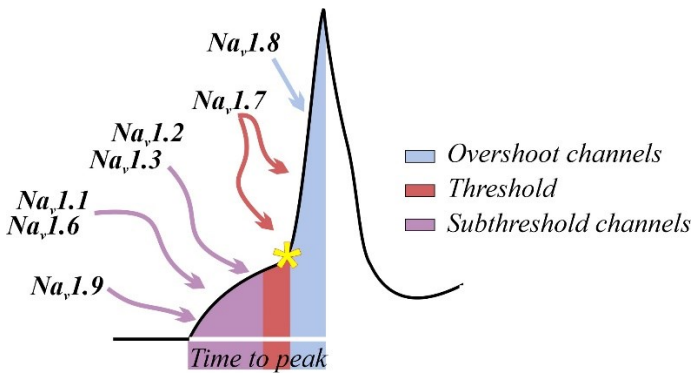

Figure 1.4. Distribution of the different voltage-gated sodium channels (VGSC) during action potential generation. Three phases can be differentiated, the subthreshold composed by hyperpolarized voltage dependence of $Na_v1.1$, $Na_v1.2$, $Na_v1.3$, $Na_v1.6$, and $Na_v1.9$, the voltage threshold that is mainly set by the action of the $Na_V1.7$ and the action potential upstroke that is controlled also by $Na_v1.7$ and the $Na_V1.8$ which has very depolarized activation. The figure was taken and modified from Meents et al. (2019).

The potassium channels are one of the largest families of ion channels, composed of about 40 different channels subdivided into several large groups. Voltage-gated K^+ channels,

(K_v) are composed of 12 distinct groups based on their amino acid sequence homology (K_v1–K_v12) (Aria, 2020; Catterall, 2013; Du and Gamper, 2013; Gutman et al., 2003). They are expressed in almost all cells of the body, being involved in major cell functions such as cell proliferation, contributing to the release of neurotransmitters and hormones, on the control of the generation, shape, and frequency of action potentials (Aria, 2020; Mathie and Veale, 2009). Cells usually have an equilibrium potential for potassium near or below -80 mV due to the higher concentration of this ion in the intracellular medium and for that, they conduct the efflux of K^+ through the membrane (Aria, 2020; Ramahi and Ruff, 2014), resulting in a hyperpolarization of the plasma membrane. In DRG neurons, they are highly expressed, being the subtype 1, the most abundant $K_v1.1$, $K_v1.2$, and $K_v1.4$, but also K_v2, K_v3, K_v7, among others (Busserolles et al., 2020). Potassium channels have been associated with the development of various human diseases including the growth of tumor cells in cancer (Brevet et al., 2009; Ko et al., 2019), and some neuropathies have been proposed as candidates as targets for novel analgesics in chronic pain (Tsantoulas and McMahon, 2014). Other groups have been associated with pain signaling such as the two-pore domain (K_{2P}) "leak" K^+ channels that are responsible for the resting membrane potential and input resistance in polymodal sensory neurons (Alloui et al., 2006; Li and Toyoda, 2015); calcium-sensitive potassium channels K_{Ca}, which are active in myelinated and unmyelinated DRG neurons being important modulators of inflammatory and neuropathic pain, and nociceptive neuron hyperexcitability (Laumet et al., 2015). Other members as G protein-coupled inwardly rectifying potassium channels (GIRK) or $K_{ir}3.1$ can be activated by μ-opioid receptor agonist in mouse peripheral sensory neurons following nerve injury (Seitz et al., 2021). Finally, some members of A-Type K_v channels, which are downregulated in neuropathic pain and bone cancer pain models have been involved in mechanical allodynia phenotypes (Conner et al., 2016; Duan et al., 2012). Undoubtedly, potassium channels play a key role in neuronal activity and are a key determinant in controlling nociceptive information across the nervous system.

Additionally, a process that plays an important role in the regulation of neuronal excitability is the balance between the cytosolic and the extracellular chloride concentration. In sensory neurons, the intracellular [Cl^-] concentration is about 77 mM in newborn mice and lowered in the third postnatal week, to about 62 mM (Gensch et al., 2015; Gilbert et al., 2007; Kaneko et al., 2002). The [Cl^-] is mainly maintained by two membrane proteins, the sodium-potassium-chloride cotransporter 1 (NKCC1) and the potassium-chloride cotransporter 2

(KCC2). The contribution of NKCC to pain is evidenced in a rat model of chronic constriction injury, which shows a decrease in thermal withdrawal latencies. Sensory neurons displayed an increase in the protein expression levels of NKCC1 together with higher cytosolic chloride concentrations. Resting membrane potential, action potential firing, rheobase, and action potential threshold were significantly altered in DRG from these animals, suggesting an important role in nociception (Tan et al., 2020).

1.4 Pain signaling pathway

After a nociceptive stimulus has reached the peripheral nerve ending, supra-threshold nociceptor depolarization generates action potentials that are transmitted along sensory fibers to the cell bodies of corresponding primary sensory neurons in the DRG. Electrical signals are converted into chemical signals and result in the secretion of neurotransmitters or neuropeptides. In the dorsal horn of the spinal cord (DHSC) signals are processed within the first two layers of the spinal cord with secondary neurons and interneurons. Subsequently, the information is transmitted to projection neurons that project their efferents on the brain. The major targets of dorsal horn projection neurons include the thalamus, the periaqueductal gray (PAG) matter of the midbrain, the lateral parabrachial area in the Pons, and various nuclei in the medulla and finally to the cortex where the response to the stimuli is transmitted back through the different descending pathways (Cheng, 2010; Todd and Wang, 2020) (Figure 1.5).

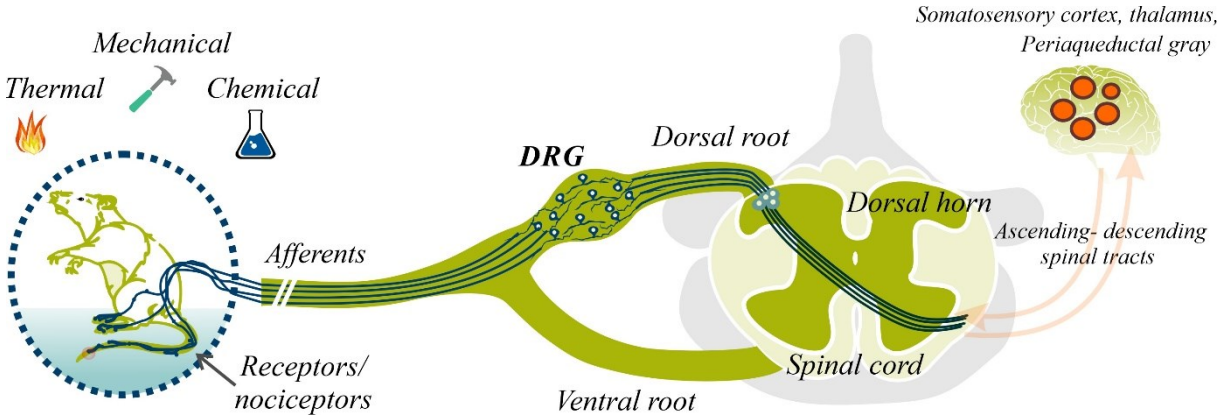

Figure 1.5. Pain signaling pathway in the mammal nervous system. Signals are obtained by the corpuscles, a complex combination of tissue and afferents that receive the noxious stimuli and transmit the action potentials to the DRG and then to the spinal cord. Signals are modulated in the DHSC and then sent to the different regions of the brain to promote a complex response to the event.

1.4.1 Sensory neurons from the dorsal root ganglia

Dorsal root ganglia (DRG) are the cell bodies of the sensory neurons, located within the intervertebral foramina, near the posterior horn of the spinal cord. They decode the pain signal and transmit it to the central nervous system (Devor, 1999; Lemes et al., 2018). They can be classified into three categories according to their function, size, and conduction velocity in Aα/β- type, Aδ-type, and C-type neurons. Aα and β- type fibers are myelinated and conduct action potentials at more than 12 m/s. The low myelinated Aδ-type neurons have a conduction velocity between 2-12 m/s, and the unmyelinated nociceptive C-type neurons have a conduction velocity of less than 1.3 m/s (Lawson and Waddell, 1991; Usoskin et al., 2015) (Figure 1.6). These data are not the same for all species and may vary with the recording method (Djouhri et al., 2020; Fang et al., 2002).

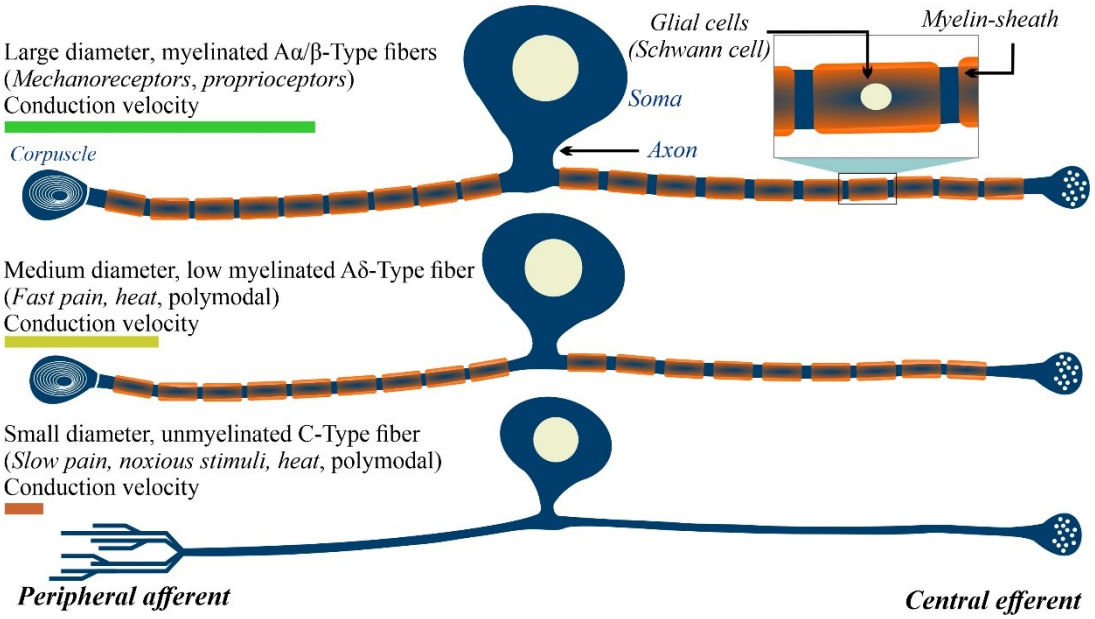

Figure 1.6. Classification of different types of dorsal root ganglion neurons according to the size and related function. Three types of DRG neurons according to their size, myelination degree and conduction velocity can be differentiated, the Aα/β-type, Aδ-Type, and the C-type, which is responsible for conducting slow-persistent pain that is associated with neuropathic/inflammatory pain.

Aα and β-neuron have terminals such as Meissner's, Pacinian's, Merkel's disks, and Ruffini's corpuscles. They are specialized to perceive and propagate proprioceptive information and innocuous touch sensation. Aδ- and C-type peripheral terminals are responsible for conducting nociceptive stimuli. The Aδ-type rapidly conducts the signal and pinpoint very precisely the localization of the noxious stimulus, meanwhile, C-type nociceptors mediate

persistent pain. However, this classification does not consider neurons that have a polymodal nature of transmitting different stimulus-response, or silent neurons which do not transmit any signal (Djouhri and Lawson, 2004; Emery and Ernfors, 2020; Usoskin et al., 2015).

1.4.2 The dorsal horn of the spinal cord (DHSC)

Nociceptive neurons detect stimuli and transfer the information to the spinal cord. DRG Aδ- and C-type neurons convert electrical into chemical signals by secreting neurotransmitters and neuropeptides into layers I and II of the dorsal horn of the spinal cord (DHSC) (Cheng, 2010), whereas non-nociceptive Aβ-fibers predominantly innervate laminae III-VI (Sugiura et al., 1986). Excitatory and GABA- glycinergic inhibitory interneurons from the DHSC modulate the input information that later is transferred to the projecting neurons. This balance between small and large fiber input is what would be interpreted as "pain" and the output signal is sent by the projection neurons to the brain once the critical preset level is exceeded. This mechanism is called the "Gate theory of pain". The important targets of the dorsal horn projection neurons include the thalamus, the periaqueductal gray matter of the midbrain (PAG), and the somatosensory cortex (D'Mello and Dickenson, 2008; Mendell, 2014; Todd and Wang, 2020).

1.5 Importance of glial activation in neuropathic pain

It has been recently demonstrated that neural cells are not the only ones that contribute to pain. Both types of glial cells, astroglia, and microglia in the spinal cord are implicated in mediating inflammatory processes. Upon extreme noxious stimuli, microglia can become activated and contribute to the development of pain in models of peripheral nerve injury, sciatic nerve ligation, or formalin injection (Hains and Waxman, 2006). Glia support neurons, synapse remodeling, maintaining brain ion homeostasis, protecting neurons from excitotoxicity and cell death (Li et al., 2019b), for example, developing astrocytes produce interleukin-33 (IL-33) required for normal synapse and neural circuit function in the spinal cord and thalamus (Vainchtein et al., 2018). Microglia also produces immune factors that have an important role in nociceptive transmission. These mediators are both pro-and anti-inflammatory cytokines such as IL-1alfa, IL-1beta, IL-2, IL-4, IL-6, IL-10, IL-15, IL-18, TNFalpha, IFNgamma, TGF-beta 1, fractalkine and CCL2, and many other factors on the spinal cord and DRG level under neuropathic pain (Mika et al., 2013; Vallejo et al., 2010).

Increasing evidence shows that cysteine-cysteine motif ligand 2 (CCL2) and its receptor (CCR2) are upregulated in different tissue in the PNS and CNS in some pain conditions. For example, it was found that levels of CCL2 were significantly elevated after administration of complete Freund's adjuvant into the plantar surface of the hind paw in mice (Menetski et al., 2007) or by oxaliplatin-induced mechanical hypersensitivity (Illias et al., 2018) in rats. Nevertheless, the neutralization of CCL2 using antibodies reduces mechanical allodynia induced by chronic constriction injury (CCI) of the sciatic nerve, spinal nerve ligation (SNL), or surgical incision (Peters and Eisenach, 2010; Thacker et al., 2009). Besides, $CCR2^{-/-}$ mice exhibited a substantial reduction in mechanical allodynia after partial ligation of the sciatic nerve (Moulin et al., 2003b). Therefore, CCL2/CCR2 signaling pathway plays an important role in the modulation of nociceptive pain.

1.6 Working hypothesis

ClC-3 is highly expressed within the CNS but is also found in the PNS. Its genetic disruption in mice causes severe neurodegeneration and alters pain sensitivity, suggesting a fundamental role of this protein role within both systems. Additionally, the work carried out in chromaffin cells suggests an important role of ClC-3 in trafficking, maturation of neurotransmitter-containing vesicles, and exocytosis of dense-core vesicles. Therefore ClC-3 might be regulating the trafficking and sorting of membrane proteins required for the initiation and propagation of electrical signals in the sensory system, affecting thus, the balance in the release of pro- and anti-inflammatory mediators along the pain pathway.

To contribute to the understanding of the function of ClC-3, this work aimed to investigate the physiological role of ClC-3 in the sensory system and its contribution to the development of neuropathic pain using a genetically modified *Clcn3*$^{-/-}$ mouse model. Furthermore, I investigated the physiological importance of chloride transport activity in the regulation of sensory signals using a ClC-3 *Knock-in* mouse in which the chloride transport of ClC-3 is completely abolished

Chapter 2. Materials and Methods

2.1 Reagents and materials

Table 2.1. List of reagents and Kits used in PCR and genotyping.

Reagents and Kits	**Catalog N°**
Hot Start PCR Master Mix	
SuperScript ™ III Reverse transcriptase, Thermo Fisher Scientific	18080044
SuperScript ™ III One-Step RT-PCR System with Platinum ™ Taq DNA Polymerase, Invitrogen	12574026
DNase Amplification Grade I, Thermo Fisher Scientific	18068015
RNAseOUT™ recombinant ribonuclease inhibitor, Thermo Fisher Scientific	10777019
Oligo-dT primers, Qiagen	79237
KAPA Hot-Start Mouse Genotyping Kit, KAPA Biosystems	KK5609
SYBR™ safe DNA gel Stain, Thermo Fisher Scientific	S33102
TRIzol™ Reagent, Thermo Fisher Scientific	15596026

Table 2.2. Reagents and materials used in cell culture of the DRG neurons.

Reagents for cell culture	**Catalog N°**
DPBS (1X), Dulbecco's Phosphate-Buffered Salines, Thermo Fisher	14190094
TrypLe™ Express Enzyme (1X), no phenol red, Thermo Fisher	12604013
Liberase™ DH Research Grade, Merk	5401054001
5-Fluoro-2-deoxyuridine, Thymidylate synthase inhibitor, Merk	F0503-250mg
URIDINE, 1-ß-D-Ribofuranosyluracil, Uracil-1-ß-Dribofuranoside, Merk	U3003-5G
Poly-D-lysine hydrobromide, Merk	P6407-5MG
B-27® Supplement (50x), serum-free, Thermo Fisher	17504044
Neurobasal-A Medium, Thermo Fisher	10888022
Fetal bovine serum, Gibco	10270-106
GlutaMAX™ Supplement 100X, Gibco	35050038
Penicillin-Streptomycin, Gibco	15070-063
Materials	**Catalog N°**
Acrodisc Syringe Filters with Support Membrane, Pall	4658
Dumont #5sf Forceps – Inox Superfine, Finescience	11252-00
Vannas Spring Scissors - 2.5mm Blades, Finescience	15002-08
Spring Scissors - Curved Up, Finescience	15017-10
Microscope cover glasses – 25 mm diameter, Assistant®	41001125
Microscope cover glasses – 25 mm diameter, Assistent®	41001113

Table 2.3. Reagents and materials used in IHC and Western blot experiments.

Reagents for Western blot	**Catalog N°**
Super Signal™ West Pico PLUS Chemiluminescent Substrate	34580
N,N,N′,N′-Tetramethylethylenediamine (TEMED), Merck	T-9281
PVDF membrane, Immobilon-P Membrane, Merck	IPVH00010
APS, Ammonium Persulfate, Thermo Fischer Scientific	17874
Acrylamide/bisacrilamide solution, 37.5:1, Serva	10688.01
cOmplete™ EDTA-free Protease Inhibitor Cocktail, Merk	5056489001
Protease inhibitor cocktail 1:500, Merk	P8340
Tween®-20, Merk	P1379
ECL Super Signal™ West Pico PLUS Chemiluminescent Substrate, Thermo Fischer Scientific	34580
Pierce™ BCA Protein Assay Kit, Thermo Fischer Scientific	23225
Materials	
Semi-Dry-Blotter, 20×20 cm, VWR	700-7156
ImmEdge™ Pen, Vector Laboratories, CA, USA	H-4000
Aqua-Polymount, Polysciences, Inc	18606-20
Cryostat-Series Microm, Thermo Scientific	HM 650
Frozen Section Medium (OCT), Epredia™ Richard-Allan Scientific™	Neg-50™

Table 2.4. List of antibodies used in immunohistochemistry and Western blot experiments.

First antibodies	**Catalog N°**	**Dilution**	**RRID***
Anti-Actin IgG, rabbit, Merk	A2103	1:500	AB_476694
Goat-α-Rabbit IgG-Peroxidase, Merk	A6154	1:25000	AB_258284
Anti-mouse α-Tubulin	T9026	1:1000	AB_477593
Anti-rabbit $Na_v1.8$ (SCN10A), Alomone	ASC-016	1:500	AB_2040188
CGRP Anti-rabbit, Millipore	AB15360	1:4000	AB_672958
NeuN Anti-rabbit, Abcam	AB104225	1:1000	AB_10711153
NeuN Anti-mouse, Millipore	MAB377	1:500	AB_2298772
CD11b Anti-rabbit, Abcam	AB133357	1:500	AB_2650514
GFAP anti chicken, Novus	NB110-58368	1:500	AB_921444
Isolectin GS-IB4 Biotin-XX, Invitrogen	I21414	1:500	AB_2314665
MCP-1 (CCL2) Anti-mouse, Merk	SRP4207	1:500	
Secondary antibodies and markers			
Donkey anti mouse Cy3 Dianova	715-165-150	1:200	AB_2340813
Donkey anti rabbit Cy2 Dianova	711-225-152	1:400	AB_2340612
Donkey anti rabbit Cy5 Dianova	711-175-152	1:400	AB_2340607
Donkey anti chicken Cy2 Dianova	703-545-155	1:500	AB_2340375
Streptavidin A488, Thermo Fisher	S11223	1:1000	
TO-PRO™-3 A642, Thermo Fisher	T3605	1:1000	

*RRID: Research resource identifiers.

2.2 Animals

2.2.1 Animal handling and maintenance

Animals were kept in-house by breeding heterozygous mice. All mice were housed with a maximum of five mice in the home-cage (green line IVC GM500, Tecniplast, Buguggiate, Italy) with food and water *ad libitum* and under controlled conditions with a 12-12 h light-dark cycle, air humidity of 55 ±10 % and a constant room temperature (RT) of 22 °C.

All animal experiments were performed in agreement with the German Animal Welfare Act (TierSchG §§7–9) and with permission by the authorities (LANUV, North Rhine Westphalia) and the local Animal Protection Committee (Permission numbers 84-02.04.2015.A108 and 84-02.04.2015.A307).

2.2.2 ClC-3 knock-out (*Clcn3*$^{-/-}$) mouse model

Clcn3$^{-/-}$ knock-out mice used in this study were kindly provided by T. Jentsch (Leibniz-Institut für Molekulare Pharmakologie (FMP) and Max-Delbrück-Centrum für Molekulare Medizin (MDC), Berlin, Germany) and *Clcn3* gene disruption was described by Stobrawa et al., (2001). Animals were maintained as heterozygous in a C57BL/6 background. *Knock-out* animals were obtained by mating heterozygous because homozygous were not fertile. Primers for genotyping are listed in table 2.5.

2.2.3 ClC-3 E281Q knock-in (*Clcn3*^{E281Q}) mouse model

Heterozygous *Clcn3*$^{+/E281Q}$ were generated by Cyagen Biosciences Inc. To generate *Clcn3*^{E281Q}, the *mCLCN3* gene (GenBank accession number: NM_173876.3) located in chromosome 8 was used as a template. The sequence contains 12 exons, on which a glutamic acid located in position 281 of the exon 7 in the ClC-3a variant was mutated for glutamine (Q) (E281Q). The corresponding amino acid is also found in position E339 in ClC-3b and E312 for ClC-3c variants. GAG to CAG mutation was introduced into exon 7 in 3' homology arm by site-directed mutagenesis in a C57BL/6 background. Homozygous animals were obtained by mating heterozygous animals and primers for genotyping are listed in table 2.5. A schematic representation of the mutation strategy is shown in Figure 2.1.

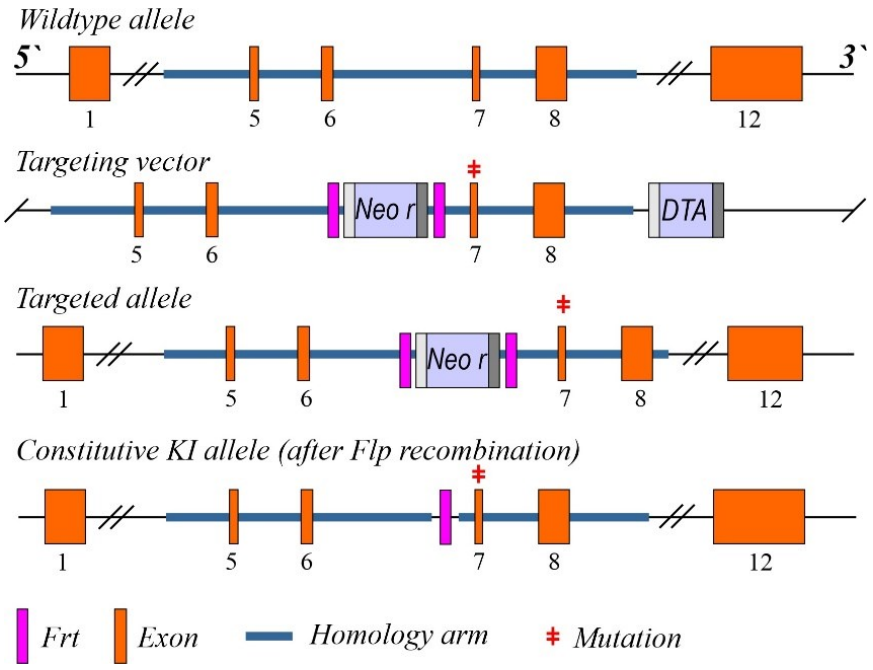

Figure 2.1. Schematic representation of the strategy used to generate the knock-in mice *Clcn3*^{E281Q}.

2.2.4 ClC-4 knock-out (*Clcn4*$^{-/-}$) mouse model

Heterozygous *Clcn4*$^{-/-}$ mice were bought from Deltagen and generated by TransGenic Inc. To generate *Clcn4*$^{-/-}$, *mClcn4* gene (GenBank accession number: NM_011334.4) located on chromosome 7 was used as a template. Disruption of the gene was made by deleting 33 bp from base 289 to base 322 by site-directed mutagenesis on a C57BL/6 background. Homozygous animals were obtained by mating heterozygous animals and primers for genotyping are listed in table 2.5.

2.2.5 ClC-3 E281Q knock-in (*Clcn3*^{E281Q}) / ClC-4 knock-out (*Clcn4*$^{-/-}$) mouse model

Double mutant mice, *knock-in* in the *Clcn3* gene, and ClC-4 *knock-out* were generated by mating homozygous of each transgenic line. Homozygous *Clcn3*^{E281Q} mice are homozygotes on chromosome 7 (BB) and wild type on chromosome 8 where *Clcn4* is located (aa). Homozygous *Clcn4*$^{-/-}$ mice are homozygotes on chromosome 8 (AA) and wild type on chromosome 7 where *Clcn3* is located (bb). The line was started with 6 males *Clcn4*$^{-/-}$ and 6 females *Clcn3*^{E281Q} to obtain the first generation F1. The F2 generation was obtained by mating F1. Since the double mutant *Clcn3*^{E281Q}/*Clcn4*$^{-/-}$ are not fertile, the line was maintained using males and females homozygous for *Clcn4*$^{-/-}$ and heterozygous for *Clcn3*^{E281Q}. The scheme of breeding strategy to obtain the double mutant is shown in Figure 2.2. Double mutant animals

were identified by using a genotype PCR reaction. A set of primers for both mouse lines are listed in table 2.5.

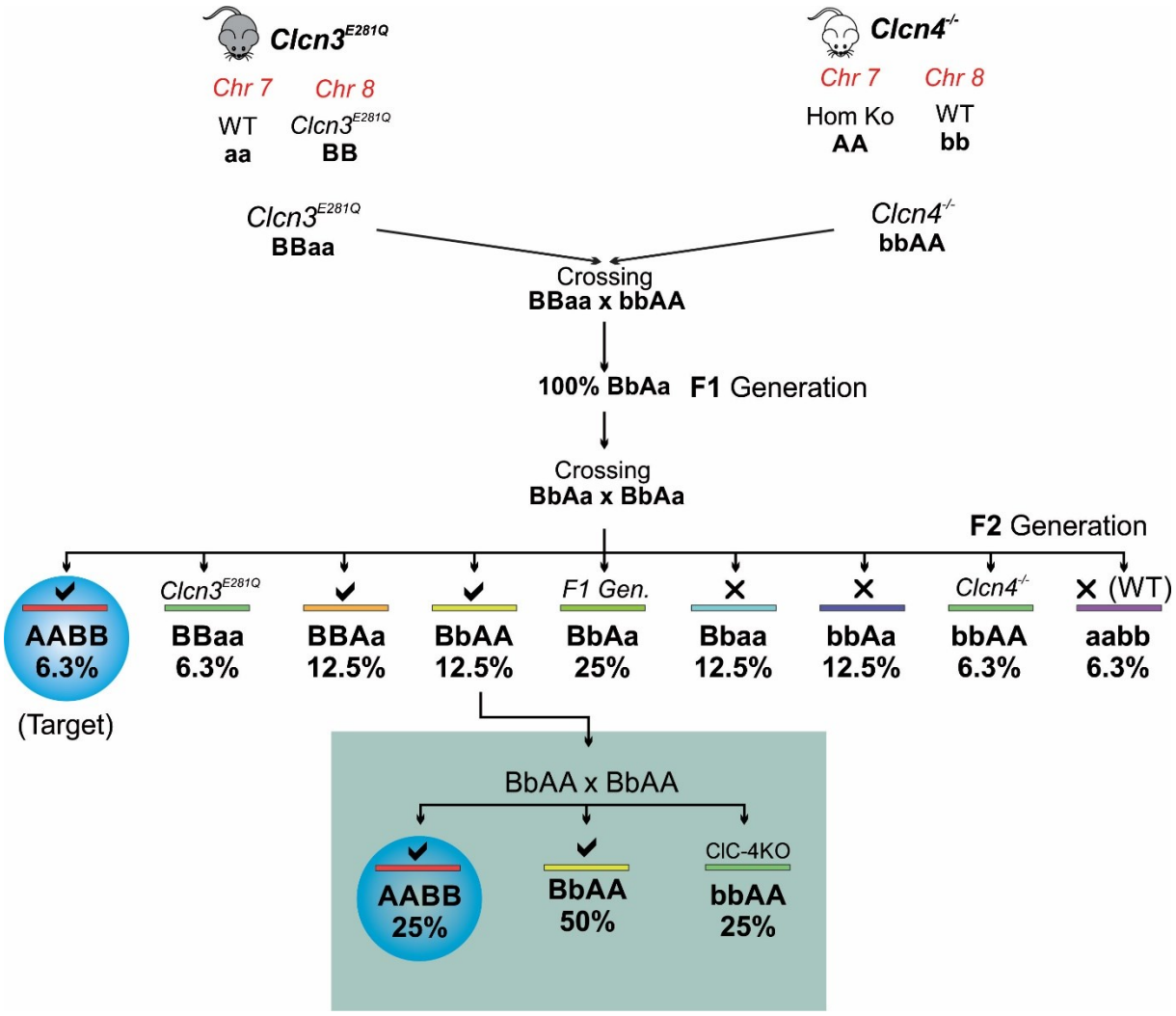

Figure 2.2. Schematic representation of the breeding strategy used to obtain the double mutant *Clcn3*^{E281Q}/*Clcn4*$^{-/-}$ mice.

2.2.6 Genotyping

Clcn3$^{-/-}$, *Clcn3*^{E281Q}, and *Clcn4*$^{-/-}$ were identified by PCR using the KAPA Mouse Genotyping Kit (KAPA Biosystems/Roche, KK-7302, Wilmington, Massachusetts, USA) following the recommended conditions. *Clcn3*^{E281Q}/*Clcn4*$^{-/-}$ was identified using both sets of primers (Table 2.5) at the same time. In brief, tubes-containing mice tail biopsies from postnatal day 0 to 1 (P0-1) or ear puncture samples were taken at P20 were kept on ice and 100 µl of extracting solution (88 µl of PCR-grade water, 10 µl of 10X extract buffer and 2 units of KAPA express extract enzyme) were added to each tube. Biopsies were enzymatically digested at 75°C

for 10-15 minutes and continuous shaking at 600rpm. Thereafter, to inactivate the enzyme, samples were incubated for 5 minutes at 95°C and later centrifuged at 11.000 RCF for 1 minute to collect the cellular debris. Finally, supernatant containing-DNA was transferred to a new tube.

The PCR reaction was performed by mixing 1 µl of DNA template with 24 µl of a master mix containing 9 µl of PCR-grade water, 2X KAPA2G Hot start Genotyping Mix, 1.25 µl of the forward primer, and 1.25 µl of the reverse primer. Forward primers were designed separately to identify the wild type and the *Clcn3*$^{-/-}$ mice. The PCR reaction protocol consists of an initial denaturation at 95°C for 3 minutes, followed by 39 cycles of denaturation at 95°C for 15 s, annealing of the primers at 58°C for 15 s and extension at 72°C for 15 s, with a final extension step of 72°C for 2 minutes.

Table 2.5. List of primers used for genotyping.

Primer	Sequence	Product size (bp)
S for WT	GATCTAATTCTGCCTTCCTC	550 WT
S for *Clcn3*$^{-/-}$	GGAAGACAATAGCAGGCATGC	650 Mut
AS for WT/*Clcn3*$^{-/-}$	ACTCTGCCCATGTTTTCCACT	***
S for WT	TCTTGCGGCGTGGCCGTCCACCCGG	329 WT
S for *Clcn4*$^{-/-}$	GACGTTGTTTGTCTTCAAGAAGCTTC	628 Mut
AS for WT/*Clcn4*$^{-/-}$	CAAGGGGATGACCGCGAGTGACTGTC	***
S for WT/ *Clcn3*^{E281Q}	CACGGGATCACAGTAGTGAAAGG	250 WT
AS for WT/ *Clcn3*^{E281Q}	CGCTGCAGTCCATTAAACAGTTTC	332 Mut

*S: sense primer, or forward primer. AS, antisense primer, or reverse primer.

Half of the PCR reaction products were then loaded in a 1.5% agarose-based gel (Agarose) containing 1:10000 SYBR^{TM} safe DNA gel Stain and ran at 120 V for 25 minutes. Bands were then visualized using UV-transillumination.

2.3 Nociceptive tests

Nociceptive behavior of female and male heterozygous (Het) and homozygous (Hom) mice was compared to their wild type littermates (WT) at two different developmental stages; at the age of 21±2 days (P21) and 60±5 days (P60). The number of animals used is given in table 2.6. Before the behavioral test was performed, mice were weighted and subsequently habituated to the testing room for 30 min in clean single cages. P21 mice were habituated to the room together with their littermates in their home cages.

Table 2.6. The number of mice used for each behavioral test in both young and adult animals.

Experiment	Number of mice		
	WT	**Het**	**Hom**
Nociceptive tests P21			
Tail flick	8	8	9
Hotplate	7	6	8
Formalin	8	8	9
Nociceptive tests P60			
Tail flick	8	8	9
Hotplate	11	12	13
Formalin	6	7	8

2.3.1 Tail flick test

The tail-flick test, first described by D'amour and Smith (1941), allows measurement of the nociceptive sensitivity of the animal by radiant heat on the tail, or tail immersion in hot water. Thus, the tail was drawn in three different sessions into a water bath (Julabo GmbH, Germany) with controlled temperatures of 46 °C, 48 °C, 50 °C, while the mouse itself was loosely restrained in the experimenter's hand. The time when the mouse showed a withdrawal of its tail was recorded. Each temperature was evaluated with three repetitions and 15 min inter-trial intervals. Between two different sessions of temperature, a break of 1 h was given.

2.3.2 Hotplate test

For the determination of thermal nociception, the hotplate test was utilized. Mice were placed onto a metal surface of a heating plate (Ugo Basile S.R.L., Italy), delimited with a 20 cm high transparent Plexiglas cylinder, allowing free movement inside. The metal surface was maintained at controlled temperatures in different sessions (46 °C, 48 °C, 50 °C, and 52 °C) (Marics et al., 2014). Time was measured until the tested mice showed discomfort, licking, or shaking of the paws.

2.3.3 Formalin test

Reaction to chemical stimulation of nociceptors was measured by injection of formalin into the hind paw. The reaction can be distinguished into two different phases (Hunskaar and Hole, 1987). In the first, acute phase, which lasts about 10 min, intensive licking of the injection site can be observed. A second, chronic phase follows 30 min after the injection due to a secondary inflammation reaction, also caused by peripheral inflammation and functional

alterations in the spinal cord. After injection of 5 µL of either concentration, 0.5 % v/v formalin solution with a Hamilton® microliter-syringe (Merck KGaA, Germany) into the right hind paw, each mouse was placed individually into a transparent box (19 cm x 19 cm x 11 cm) with three mirror walls. Subsequently, after injection, the time of licking was evaluated, as well as shaking the right hind paw was counted. Measurements were repeated every 5 min for 1 min in a period of 40 min. Pain experiments were performed with the contribution of Dr. Antje Willuweit, Carina Balduin, Michael Schöneck, and Verena Graf from the Institute of Neuroscience and Medicine, Medical Imaging Physics (INM-4), Forschungszentrum Jülich.

2.4 Cell culture

2.4.1 Coating of coverslips

Glass coverslips 25 mm or 13 mm in diameter were placed in six-well or four-well plates respectively under sterile laminar flow cabinet and coating with 0.5 mg/ml of poly-D-lysine hydrobromide solution, plates were covered with parafilm and kept overnight. The next day the solution was removed, and glass coverslips were washed three times with double distilled sterile water and dried. Before use, six-well or four-well plates containing glass coverslips were UV-radiated.

2.4.2 Cultured Dorsal root ganglion (DRG) neurons

The protocol used for the extraction and culturing of DRG neurons was kindly provided by Dr. Ute Becherer and slightly modified from (Bost et al., 2017). Two-month-old (P60) and three-weeks old (P21) mice were used for the experiments. Since the *Clcn3*$^{-/-}$ shows a complex phenotype including hippocampal and retinal degeneration, loss of weight, and hyperactivity (Stobrawa et al., 2001), all the animals, including the wild type and the heterozygous were monitored and scored every week according to the Tierversuchsantrag (AZ: 84-02.04.2015.A108). Food was supplemented with glucose gels pads to decrease the lethality of the mutants.

One mouse at a time was placed in a special container and anesthetized by adding 500 µl of isoflurane. The breathing of the animal was monitored until normalization. Once the mouse was unconscious, it was sacrificed via decapitation according to the German Animal Welfare Act, followed by exsanguination to improve the visibility of the procedure. The procedure of the culture of DRG neurons is described as follows and it is represented in Figure 2.3.

Once the animal is decapitated, the front and hind paws were extended and fixed to a clean gel plate with needles. The fur over the body was removed and the tissue and muscles surrounding it were cut away. The spine was transected at the level of the hind legs located between L5 and S1 vertebrae, cut off the upper part of the spine, and removed the spinal narrow carefully. Around 30 dorsal roots were dissected and placed into iced-cold Locke's solution (in mM, 154 NaCl, 5.6 KCl, 3.6 $NaHCO_3$, 5 Hepes, 6 Glucose, pH 7.3 with NaOH) within 30 minutes post-mortem.

Once extracted, DRGs were treated enzymatically with 200 µl of TrypLE™ Express Enzyme for 5 minutes at room temperature. Subsequently, the samples were transferred to a tube containing 20 µl of freshly thawed Liberase, 1 mL of Neurobasal-A medium (final concentration of 2.3 units/ml of collagenase). The tube then was placed in a water bath at 37°C with gentle agitation before dissociation. The dissociation of the neurons was performed in three steps: 7 minutes of incubation followed by 10 times trituration with a 1000 µl pipette tip, 5 minutes of incubation followed by 10 times trituration, and finally 5 minutes of incubation followed by 15 to 17 times trituration. Inactivation was done by adding 200 µl of pure FCS and keeping the tube at 37°C with gentle agitation for 3 minutes.

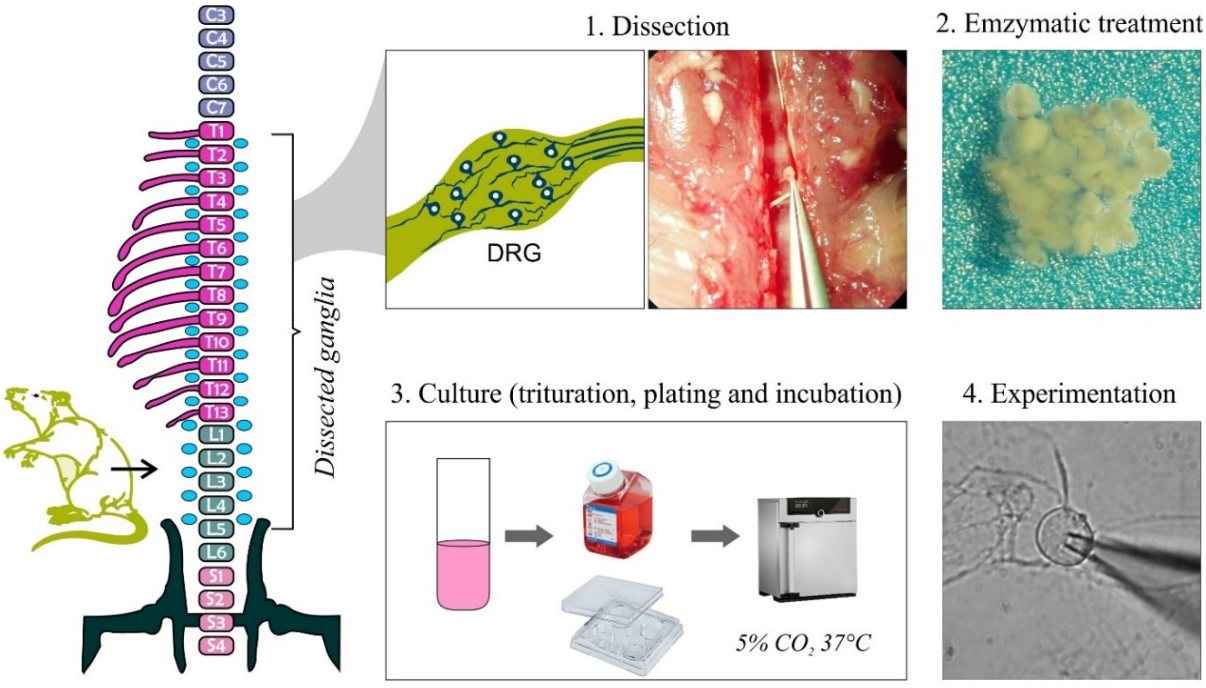

Figure 2.3. Extraction and culturing procedure of DRG neurons for electrophysiology.

The cell suspension was then collected at 400 RCF for 4 minutes, the supernatant was discarded and 700 µL of Dulbecco's Phosphate-Buffered Salines (DPBS) was added to the cells to wash out the enzymatic solution. Cells were pelleted again (400 RCF for 4 minutes), DPBS was replaced by a freshly prepared NBA culture medium, and cells were resuspended. Cell debris was allowed to sediment for 1-2 minutes. Complete neuronal suspension, around 700 µl was collected and diluted in 3.5 ml of NBA. Around 500 µl of cell suspension were seeded onto the coated coverslips and maintained at 37°C, 5% CO_2, 90% humidity for 1-5 days.

2.4.3 Enriched culture NBA medium for DRG neurons

DRG were supplemented with NBA-based medium containing 1% B-27® supplement, 1% Glutamax, 0.4% Penicillin/Streptomycin, 5% Fetal bovine serum FBS, and FUDR, a cocktail of 40 mM Uridine and 100 mM Floxuridine thymidylate synthase inhibitor. After 12 hours culture medium was replaced by an enriched NBA medium without FUDR.

2.5 Real-time PCR

Total RNA was extracted from freshly dissected DRG neurons from two-month-old mice using the TRIzol™-chloroform method. One µg of total RNA was converted into cDNA using One-Step SuperScript™ III® Reverse transcriptase in a Gradient Thermocycler (Biometra GmbH, Göttingen, Germany). A master mix was used by adding 12.5 µl of 2X reaction Mix (buffer containing 0.4 mM of each dNTP and 3.2 mM of MgSO4), 1 µl of the enzyme, 0.5 µl of 10 mM sense/antisense primers (specific for each isoform), 1 µg of template RNA and RNA-free water up to 25 µl (Kawasaki et al., 1999; Wacker and Godard, 2005). To synthesize the specific cDNA the following conditions were used: 30 minutes incubation at 55 °C, followed by 2 minutes at 94 °C. 15 seconds at 94 °C (denaturation), 30 seconds at 55-65 °C (annealing), and 5 minutes at 68 °C for the extension, these steps were repeated 40 times and a final steps of 1 min at 68°C. These conditions were adapted from Wacker and Godard (2005). As reference gene 18S was used. Primers to identify the ClC isoforms are listed in table 2.7. The PCR products were checked via gel electrophoresis using 1% agarose gel containing SYBR™ safe staining and ran for 35 minutes at 120 V. To verify the correct size of the PCR bands a GeneRuler 100 bp DNA Ladder was used parallel.

Table 2.7. List of primers used to identify the ClC exchangers in DRG.

Isoform	Sequence	Type	Size (bp)
ClC-3a	5'-CGCCCAGCTTGCTATGCCTCTGAG-3'	Forward	324
	5'-AGCTAGTGCCCCTGATGCCAGTC-3'	Reverse	
ClC-3b	5'-CGCCCAGCTTGCTATGCCTCTGAG-3'	Forward	500
	5'-AGCTAGTGCCCCTGATGCCAGTC-3'	Reverse	
ClC-3c	5'-ATGGATGCTTCTTCTGATCC-3'	Forward	379
	5'-AGCTAGTGCCCCTGATGCCAGTC-3'	Reverse	
ClC-4	5'-GACGTGGGGACCTACGAGGACTTCC-3'	Forward	508
	5'-CACTCAAAATAGTCTTTATCTCGGGTATGCC-3'	Reverse	
ClC-5	5'-CAGAGGCTTTCATCAGGGGAGTTTTAG-3'	Forward	499
	5'-CTCAGAATTCCAGCAACAGTGCTCATG-3'	Reverse	
ClC-6	5'-CTTCCAAGGAAAGACTATGAGAGTCTGGAC-3'	Forward	463
	5'-CAAAGAGCCCTCCAGACACACTGAAC-3'	Reverse	
ClC-7	5'-GAGGAGGAAAGACGAATCAACCACAC-3'	Forward	501
	5'-GATCTTGAAATCTCGCTTGAGTGATGTTG-3'	Reverse	
18S	5'-CAGTATGACTCCACTCACGGCAAATTC-3'	Forward	~530
	5'-CACAGTCTTCTGGGTGGCAGTGATG-3'	Reverse	

2.6 Immunohistochemistry

Dissected spinal cord and at least 4 dorsal roots from the L2-L5 were fixed with 4% PFA for 45 minutes. Subsequently, to cryoprotect the samples, tissues were immersed in 10% sucrose solution for 1 hour at room temperature followed by overnight incubation in 30% sucrose at 4°C. Once samples were cryoprotected, they were embedded into the Optimal Cutting Temperature (OCT) compound. A 5 mm section of spinal cord tissue dissected from the thoracic/lumbar segments from T10 to L2 was used.

About 4 to 5 thin sections of 20 µm from each tissue were cut using a cryostat, and mounted onto single slides, dried for 5 minutes at room temperature, and stored at -20°C until use. Sections were surrounded with ImmEdge^{TM} Pen, a water-repellent marker. To unmask antigens and epitopes that have been formed by cross-linking on formalin-fixed tissue, sections were treated with sodium citrate buffer (10 mM of sodium citrate, 0.05% Tween 20, pH 6.0 adjusted with NaOH) at 80°C for 30 minutes, followed by a blocking step with a solution containing 10% FCS, 1% BSA in PBS-T (0.5% Triton X-100) for 2 h at room temperature to reduce non-specific binding.

The blocking solution was washed out with 0.1 M PB (phosphate buffer containing 100 mM Na_2HPO_4 and 100 mM NH_2PO_4, pH 7.2 with NaOH) and incubated with primary antibodies diluted in blocking solution for 72 hours at 4°C in a moist sealed chamber. Then, slides were washed 5 times with 0.1 M PB 10 min each and incubated with the secondary antibodies diluted in blocking solution for 1.5 hours at room temperature in a dark humidified chamber. Finally, slides were washed 5 times with 0.1 M PB and embedded with Aqua-Polymount in a glass coverslip. Slides were stored overnight at room temperature until they were completely dry and stored at -20°C until scanning.

2.7 Confocal microscopy and image analysis

Single or multiple cans were made in a confocal microscope (TCS SP5 II, Leica Microsystems, Germany) which provides an Argon laser for 458 nm (for CFP) and 488 nm (for Cy2 and GFP), and three Helium-Neon lasers for 543 nm (for Cy3), 594 nm (for Alexa594) and 633 nm (for Cy5 and TO-PRO®3). Laser intensities and filter settings were controlled by the Leica LAS AF software. Optical images were acquired using 20x/0.70 or 63x/1.32-0.6 oil immersion objectives, and pictures were digitalized with a resolution of 1024x1024 pixels, 200 Hz velocity, and 6-line average in sequential scanning mode to rule out crosstalk between the fluorescence detection channels in samples with multiple staining. For large tissue imaging, a tile scan procedure was applied with a 10% stitching threshold and stacks of pictures at different focal planes were obtained with a distance between different focal planes set in 1 μm. Same conditions for laser intensity and digital gain were applied for both phenotypes. Images were processed with FIJI (Image J v.1.53c, Wayne Rasband, National Institutes of Health, USA) (Rueden et al., 2017; Schindelin et al., 2012), and automated analysis of fluorescence, area, shape and the number of events was done in a self-made pipeline in CellProfiler™ cell image analysis software (v.3.1.9 Broad Institute, Cambridge, MA, USA) (Lamprecht et al., 2007; McQuin et al., 2018).

2.8 Western blot experiment

Wild type and *Clcn3*$^{-/-}$ mice at the postnatal day 60±5 days (P60) were sacrificed and spinal cord and bilateral T1 to L5 DRG were rapidly collected by using the extraction procedure previously described (section 2.4.2). The tissue was frozen by immersion in liquid nitrogen and stored at -80°C until use.

Whole tissue from two animals was resuspended in 20-times its volume on iced-cold homogenizing buffer containing 2 mM EDTA pH 8.0, 1 mM of cOmplete™, and protease inhibitor cocktail 1:500. The tissue was homogenized around 10 to 20 times using a sterile glass homogenizer and maintained on ice to avoid protein degradation. The homogenized samples were transferred into a safe ultracentrifuge tube using a glass Pasteur pipette and centrifuged at 100.000 RCF for 15 minutes at 4°C.

The supernatant containing cytosolic proteins was discarded and the pellet containing the fraction of membrane proteins was resuspended in 10-times the original tissue volume in solubilization buffer and incubated for 10 minutes at room temperature. The solubilization buffer contains the following components: 1% SDS, 10 mM NaPOi (Phosphate buffer solution composed of 92.2 mmol of Na_2HPO_4 and 6.8 mmol of NaH_2PO_4), and 1 mM cOmplete™.

The membrane suspension was centrifuged at 15000 RCF for 10 minutes to precipitate large, insolubilized material. Subsequently, the supernatant was transferred into a new tube and protein concentration was determined by using the BCA-assay.

A maximum of 25 µg of total protein per lane was loaded in a 50 µl pocket of a polyacrylamide gel with a stacking phase made of 5% acrylamide (Tris-Cl 0.5 M, pH 6.8, SDS 0.1%, ammonium persulfate (APS) 0.2%, N,N,N′,N′-Tetramethylethylenediamine (TEMED) 0.1%) and a separation phase of 7.5% acrylamide (Tris-Cl 1.5 M, pH 8.8, 0.1% SDS, 0.2% APS and TEMED 0.1%) to allow the resolution of proteins above 250 kDa.

Samples were previously treated at 95°C for 5 minutes with 4x loading buffer (200 mM Tris-Cl, pH 6.8, 8% SDS, 4% 2-mercaptoethanol, 50% glycerin, and 0.04% bromophenol blue), and bands were resolved by electrophoresis at 18 mA for 1.5 hours. Thereafter, proteins were transferred from the SDS gel to a polyvinylidene difluoride (PVDF) membrane at 200 mA for 25 minutes using the semi-dry transfer technique. PVDF membranes were dried overnight and blocked for 2 hours in 5% nonfat milk solution in PBS-t (phosphate buffer saline with 0.05% Tween®-20) for sodium channel or in a solution containing 3% of BSA in PBS-t for control antibodies β-Actin or α-Tubulin.

PVDF membranes were incubated overnight at 4°C with gentle agitation with primary antibodies Anti-rabbit $Na_v1.8$ sodium channel (1:500), anti-β-Actin rabbit (1:1000, 42 kDa), or with anti-α-Tubulin produced in mouse (1:1000, 50 kDa). A peptide control that binds to the antibody was used in the wild-type condition to test the specificity. Membranes were washed 3

times with PBS-t for 5-10 minutes and subsequently incubated for 1 hour with slow agitation at room temperature with Goat-α-Rabbit IgG-Peroxidase secondary antibody (1:10.000). After incubation and washing protocol as previously described, membranes were exposed to an equal amount of ECL Super Signal™ West Pico PLUS Chemiluminescent Substrate, and the exposure time was adjusted depending on the abundance of the proteins, between 1-10 minutes to maximize the visibility and decrease the background level.

2.8.1 BCA-Assay

Total protein concentration was determined by the bicinchoninic acid (BCA) method. It uses colorimetric detection and quantitation of total protein after the reduction of Cu^{+2} to Cu^{+1} by proteins in an alkaline medium or so-called the Biuret reaction (Walker, 1996). In brief, 9 dilutions of a BSA-containing solution were prepared to elaborate a calibration curve. Solutions were prepared in the same resuspension solution for our sample, containing 1% SDS. All the concentrations are shown in Table 2.8.

Table 2.8. Preparation of diluted BSA standards.

Tube	Final concentration (µg/µl)	Volume of BSA (stock of 2 µg/µl)	Volume of buffer (µl)
1	0.00	0.00	10.00
2	0.25	1.25	8.75
3	0.50	2.50	7.50
4	0.75	3.75	6.25
5	1.00	5.00	5.00
6	1.25	6.25	3.75
7	1.50	7.50	2.50
8	1.75	8.75	1.25
9	2.00	10.00	0.00
10	Sample of interest	10 µl of suspension	

A working reagent (WR) containing BCA and cupric sulfate was prepared by diluting reagent A and B in a proportion of 1:50 until it forms a green coloration according to the specifications. 200 µl of freshly prepared WR were added to each tube and kept at 50°C for 5 minutes until a purple-colored reaction is developed. Calibration curves were made by colorimetric measurement on a pedestal nanodrop using a wavelength of 555-562 nm, once the calibration reached an R^2 of 0.9998, our sample of interest was measured.

2.9 Electrophysiological experiments

2.9.1 Whole-cell patch-clamp recordings in voltage-clamp mode

To measure sodium and potassium currents, whole-cell patch-clamp recordings were performed within the first 24 hours after neuronal plating. To decrease the space-clamp errors healthy DRG neurons with no obvious processes were measured. For sodium currents the following bath solution was used: (in mM) 10 NaCl, 105 Choline-Cl, 3 KCl, 1 $MgCl_2$, 1 $CaCl_2$, 10 Hepes, 10 D-glucose, 20 TEA-Cl, 0.1 $CdCl_2$, 3 4-aminopyridine (4-AP), 305 mOsm/kg, pH 7.4 with Choline-OH. And a pipette solution containing (in mM): 7 NaCl, 105 CsF, 10 EGTA, 10 Hepes and 50 D-glucose and 300 mOsm/kg, pH 7.4 with CsOH was used. To block fast inactivation TTX-sensitive sodium channels tetrodotoxin (TTX) at 300 nM was applied extracellularly to the cells. Recordings were acquired before and after the application of TTX (Fischer et al., 2017; Meents and Lampert, 2016). Osmolality was adjusted with D-glucose and measured with a freezing point osmometer (Osmomat 3000 basic, Gonotec). For potassium currents the bath solution contained (in mM): 150 Choline-Cl, 5 KCl, 1 $MgCl_2$, 2 $CaCl_2$, 10 Hepes, 1 $CdCl_2$, 10 D-glucose, 320 mOsm/kg, pH 7.4 with Choline-OH. And Pipette solution containing (in mM): 120 K-gluconate, 20 KCl, 2 $MgCl_2$, 1 $CaCl_2$, 10 EGTA, 10 HEPES, 5 Mg-ATP, 0.3 Na_2GTP, 315 mOsm/kg, pH 7.4 with NaOH was used. 5 mM of 4-AP was added to the bath to block fast inactivated potassium currents. Cells were measured before and after the application of the blocker.

Recordings were filtered at 10 kHz and sampled at 100 kHz using an EPC10 double patch amplifier, controlled by PatchMaster (HEKA Elektronik, GmbH). Borosilicate pipettes (GC150F-10, Harvard Apparatus, USA) were pulled with resistance typically from 1.9-2.9 MΩ. Pipettes were coated with a thin layer of wax to reduce fast capacitance, which was compensated after seal formation. Cell capacitance (C_m) and series resistance (R_s) were also compensated. Currents were compensated with 80-85% R_s, 100 µs, and P/4 leak subtraction with a baseline of -80 mV was used to cancel linear capacitances.

Peak currents for sodium and mean steady-state currents were plotted against the test voltage in an I/V relationship. Activation curves for sodium currents were derived by plotting normalized G_{Na} as a function of test potential and fitted with the Boltzmann equation (Favre et al., 1995; Körner et al., 2018), according to the following equations:

$$G = \frac{I_{(Na^+)}}{V - V_{(rev)}}$$

$$I_{Na^+} = \frac{(V - V_{rev}) \cdot G_{max}}{1 + e^{(V - V_{half})/dV}}$$

$$G/G_{Max} = \frac{1}{1 + e^{(V - V_{half})/k}}$$

Where the $I_{(Na^+)}$ is the peak sodium current elicited by the voltage pulse, V is the test potential, $V_{(rev)}$ is the reversal potential, G is the conductance, G_{Max} is the maximal conductance, V_{half} is the voltage for half-maximal current activation, and k is equal to the slope factor in mV.

Additionally, inactivation currents were normalized to the maximal value and curves were fit with single (TTX-R) and double (total current) Boltzmann function:

$$\text{For total current: } I = \left[\frac{f}{1+e^{(V - V_{half1})/k1}} + \frac{1-f}{1+e^{(V - V_{half2})/k2}}\right]$$

$$\text{For TTX-R current: } I/I_{Max} = \frac{1}{1+e^{(V - V_{half})/dV}}$$

With I being the inactivated current, I_{Max} the recorded current at -10 mV after the most hyperpolarizing prepulse, V the test potential, V_{half} the voltage for half-maximal current inactivation (*half1* and *half1* correspond to first and the second midpoint), and k the slope factor in mV (*k1* and *k1* correspond to first and the second component).

2.9.2 Action potentials generation in current-clamp mode

For action potential measurements, DRG neurons were used between DIV 3-4. Neurons were patched in voltage-clamp mode and after breaking in through the cell membrane it was switched to current-clamp mode. Recordings were performed under physiological saline solutions. Bath solution (330 mOsm/kg, pH 7.4 with NaOH) contained (in mM): 130 NaCl, 4 KCl, 1 $MgCl_2$, 2 $CaCl_2$, 10 Hepes, 48 D-glucose. Pipette solution (310 mOsm/kg, pH 7.4 with NaOH) contained (in mM): 135 K-gluconate, 7 NaCl, 2 $MgCl_2$, 2 Na-ATP, 0.3 Na_2-GTP, 10 Hepes, 0.2 EGTA. These solutions were adapted from (Hoerauf et al., 2015; Liu et al., 2010b). Passive and active properties of the cells were measured using a rectangular current pulse

injection for 1 s with an increase in step size of 10 pA from -70 pA with a pre-and post-pulse of 500 ms.

Analysis of passive membrane properties

Resting membrane potential (RMP) was measured a few minutes after obtaining the whole-cell configuration in stable neurons to allow the dialysis of the intracellular solution and before applying the first protocol to elicit the first action potential. The RMP was obtained as the average voltage of 10 ms before the first current injection. Only neurons with a stable resting membrane potential between -60 mV and -75 mV and with a series resistance less than <12 MΩ were included for data analysis to guarantee a high recording quality (Figure 2.4A).

To evoke the first action potential, current steps starting from -70 pA in 10 pA increments were applied (1 s duration) to cells. For a more precise calculation, voltage response was recorded using 2 pA increments of current injection from 20 pA less than the necessary current when the first AP was observed. Properties of single AP (Figure 2.4B) such as current threshold (rheobase) defined as the minimum current required for the initiation of the first spike was recorded. Input resistance (R_{in}) was calculated as the slope of the relationship between the voltage response to current injection in a range from -60 pA to 20 pA before the first AP. The membrane time constant (Tau) indicates the time that takes for the neuron to change from the steady-stated potential during the injection of -50 pA to the RMP. It is calculated by the fitting of the hyperpolarizing voltage response as a monoexponential function (Lazarus and Huang, 2011; Tripathy and Gerkin, 2013).

AP time and AP threshold (mV) are defined as the time of the event, and the membrane potential when the AP is initiated. AP threshold is calculated using the first derivative of the voltage response when the rate of rising is equal to 10 mV/ms (Lazarus and Huang, 2011). AP amplitude was calculated as the difference between AP peak and AP threshold voltages. AP half-width was established by the difference between rising phase time and decaying phase time at the half-maximum amplitude of the AP (Tripathy and Gerkin, 2013). After hyperpolarization amplitude (AHP) is defined as the difference between the AP threshold and the minimum voltage response after the peak maximum. All the AP properties were analyzed from the first-ever action potential using a custom-written Igor-based macro (Igor Pro 7.01 software, Wavemetrics) kindly provided by Dr. Karlijn van Aerde and Dr. Dirk Feldmeyer, INM-10, Forschungszentrum Jülich.

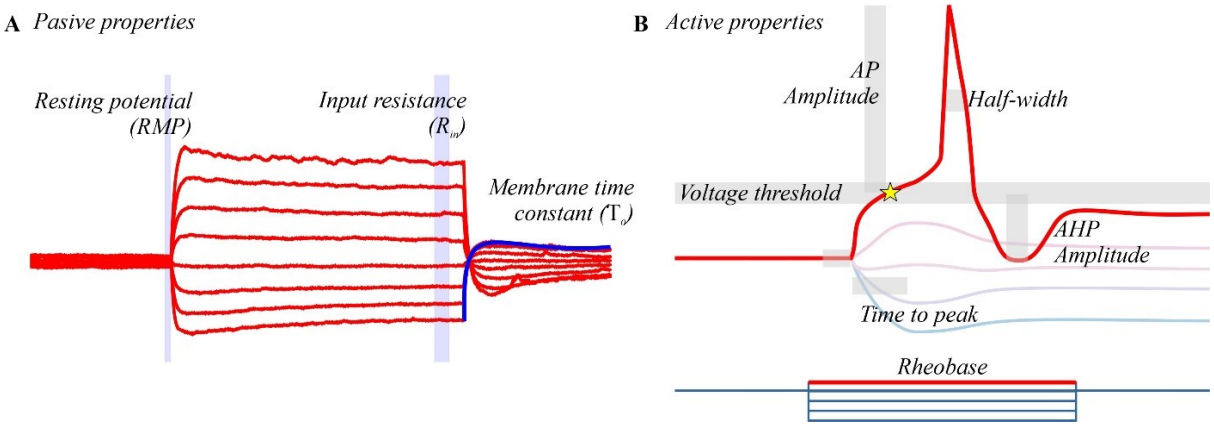

Figure 2.4. Analysis of passive and active action potential properties of DRG neurons. A) Passive properties such as resting membrane potential, input resistance, and membrane time constant, blue line: monoexponential fit of the membrane time constant. B) Shows how the active properties of the action potential are calculated.

Firing properties were then measured with a larger increase in step size of 20 pA from -40 pA to +700 pA for 1 s. Cells with at least one train of a minimum of 3 action potentials were used for analysis. For an estimation of the excitability of the neuron, an index to evaluate the intrinsic excitability was used as described by Lazarus and Huang (2011). A lower excitability index (EI) would reflect a more excitable cell, and vice versa (Lazarus and Huang, 2011). This index includes properties as RMP, AP threshold and R_{in}, in the following equation:

$$EI = \left(\frac{AP\ threshold - RMP}{R_{in}}\right)$$

2.9.3 Solutions used for electrophysiological measurements

All the solutions presented in this section were prepared totally or partially in advance, pH calibrated, osmolality measured and sterile filtered using 0.22 µm pore filter and stored at 4°C or -20°C accordingly. These solutions were adapted from (Borisovska et al., 2005; Hoerauf et al., 2015; Ishihara, 2018; Meents and Lampert, 2016; Vydyanathan et al., 2005) and the concentration for each compound listed in Tables 2.9 and 2.10.

Intracellular solutions were prepared partially in advance at 1.1x concentration without the ATP. However, the pH was calibrated, and the osmolality was measured using the final version of the solution. Mg-ATP and Na_2-GTP solution was prepared separately and stored at -20°C. On the day of the experiments, 180 µl of the pipette solution was mixed with 20 µl of thawed ATP solution and kept on ice.

Table 2.9. Extracellular solution for action potentials and ion channel recordings.

Compound	MW (mg/mmol)	Action potentials [mM]	Na^+ currents [mM]	K^+ currents [mM]	IRK currents [mM]
NaCl	58.44	130	10	-	-
Choline-Cl	139.60	0	105	150	135
KCl	74.55	4	3	5	20
$MgCl_2$	203.30	1	1	1	1
$CaCl_2$	147.00	2	1	2	2
Hepes	238.30	10	10	10	10
Glucose	180.16	48	10	10	10
TEA-Cl	165.70	-	20	-	-
$CdCl_2$ (H_2O)	201.23	-	0.1	1	1
4-AP	94.11	-	3	5*	-
TTX	319.27	-	0.0003*	-	0.0003
Adjusted pH		7.3 with NaOH	7.3 with Choline-OH	7.3 with Choline-OH	7.3 with Choline-OH
Expected osmol. (mOsmol/Kg)		330-335	300-305	320-330	320-330

* Perfusion solution to block specific channels was prepared using ringer solution and the desired blocker in each case.

Table 2.10. The pipette solution for action potentials and ion channel recordings.

Compound	MW (mg/mmol)	Action potentials [mM]	Na^+ currents [mM]	K^+ currents [mM]	IRK currents [mM]
NaCl	58.44	7	7	-	-
CsF	151.90	-	105	-	-
KCl	74.55	-	-	20	20
K-Gluconate	234.25	135	-	120	60
$MgCl_2$	203.30	2	-	2	2
$CaCl_2$	147.00	-	-	1	1
Mg-ATP	507.18	2	-	5	5
Na_2-GTP	523.18	0.3	-	-	-
EGTA	380.35	0.2	10	10	10
Hepes	238.30	10	10	10	20
Glucose	180.16	-	50	-	120
Adjusted pH		7.3 with NaOH	7.4 with CsOH	7.4 with KOH	7.4 with KOH
Expected osmol (mOsmol/Kg)		310-315	294-300	315-320	300-305

2.10 Data analysis and statistics

Data are presented as the average mean ± standard error of the mean (SEM). For *in vivo* experiments, Statistical analysis was performed using the Single Measure and Repeated Measures Parametric Analysis module of InVivoStat (version 3.7.0, Clark RA, Shoaib M, Hewitt KN, Stanford SC, Bate ST 2012) (Clark et al., 2011). Power analysis was performed to assure experiments were not statistically underpowered. GraphPad PRISM 5 (Version 5.0, GraphPad Software, Inc., USA) was utilized for statistical calculations of unpaired students t-test (two-tailed) and two-way ANOVA. Values with $p>0.05$ were considered as not significant (n.s.).

For *in vitro* experiments statistical calculations were performed using Origin(Pro) version 2018b (OriginLab Corporation, Northampton, MA, USA) and Microsoft® Excel® for office 365. For mean or median comparison, the Shapiro Wilk normality test and Levene's test for assessing variances were applied. After passing the assumption of normality and variances, either one-way ANOVA or non-paired t-test of means were performed. If normality and homogeneity of variances tests failed, Mann-Whitney or Kruskal-Wallis analysis of variances non-parametric tests were applied.

Chapter 3. Results

3.1 Acute thermal pain threshold is altered in *Clcn3*$^{-/-}$ mice

To study the role of ClC-3 in pain perception thermal withdrawal thresholds in *Clcn3*$^{-/-}$, heterozygous (*Clcn3*$^{+/-}$) and wild type (WT) were determined at two different developmental stages, at postnatal day 21 (P21, the age at which *Clcn3*$^{-/-}$ shows a phenotype) and postnatal day 60 (P60, the age at which mice are mature, and where photoreceptors and hippocampal neurons have degenerated). Tail immersion, hot plate, and formalin tests were used to evaluate peripheral mechanisms of pain perception.

In the hot plate test, the P21 *Clcn3*$^{-/-}$ showed reduced paw withdrawal latencies to the heat stimulus especially at temperatures over 48 °C (Figure 3.1A and 3.2A). *Clcn3*$^{+/-}$ shows similar reaction times to the wild type in all the temperatures tested and significant differences at 48°C, 50°C, and 52°C when compared with the *Clcn3*$^{-/-}$. The tail immersion assay confirms that *Clcn3*$^{-/-}$ mice are more sensitive to a noxious thermal stimulus than wild type and *Clcn3*$^{+/-}$. The threshold for a withdrawal reflex to thermal stimulation was dramatically reduced in the absence of ClC-3. For all temperatures tested in this study, young *Clcn3*$^{-/-}$ mice displayed a significant reduction in the latency to tail-flick reactions when compared to the wild type littermates and *Clcn3*$^{+/-}$ (Figure 3.1B and 3.2B).

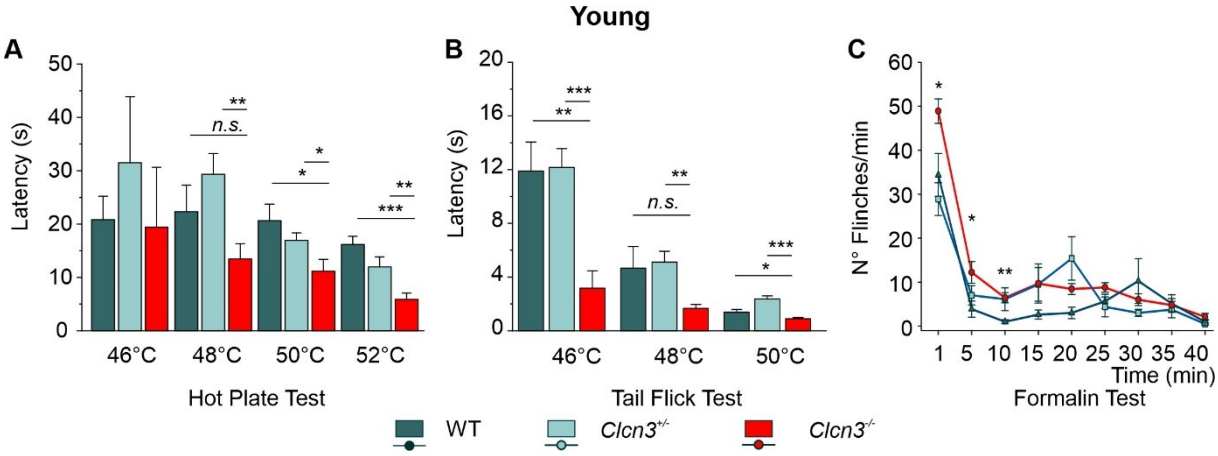

Figure 3.1. Acute thermal pain experiments in young P21 mice show increased thermal sensitivity and lower latencies in mutant than in WT animals. **A** Hot plate test experiment at different temperatures, WT (*n=7*); *Clcn3*$^{+/-}$ (*n=6*); *Clcn3*$^{-/-}$ (*n=8*). **B** Tail flick test at different temperatures, WT (*n=8*); *Clcn3*$^{+/-}$ (*n=8*); *Clcn3*$^{-/-}$ (*n=9*). **C** Formalin test applied to the animal's hind paw. WT (*n=8*); *Clcn3*$^{+/-}$ (*n=8*); *Clcn3*$^{-/-}$ (*n=9*). Significance levels are given as *p<0.05, **p<0.01, ***p<0.001. * *Clcn3*$^{-/-}$ differs from WT.

The response of young mice to subcutaneous injection of formalin (0.5%) into the hind paw of the mice was also examined. This stimulation triggers a biphasic pain reaction, first an early-phase paw-licking response due to direct stimulation of peripheral nociceptors, and second, an inflammatory late-phase reaction caused by a persistent input of pain signals at the supraspinal level (Abbadie et al., 1997; Taylor et al., 1995). Biphasic licking responses in *Clcn3*$^{-/-}$ and wild type mice were recorded over time. *Clcn3*$^{-/-}$ mice showed an increased reaction to the noxious stimulus at one, five, and ten minutes after injection, when the number of flinches was significantly different from the wild type. The reaction in heterozygous mice was similar to the wild type condition. From the second inflammatory phase, from 15 to 30 minutes, all three animals showed an increased reaction, but significant differences were not observed (Figure 3.1C).

To test whether ClC-3 dependent hyperalgesia is developmentally regulated, pain behavior experiments were performed in P60 animals. The results were then compared to the previous results obtained from P21 mice. Results from both, hot plate and tail-flick thermal tests show a faster reaction in the *Clcn3*$^{-/-}$ when compared to wild-type mice. Statistical differences between wild type and *Clcn3*$^{-/-}$ mice were found at temperatures above 48°C for hot plate test, and between *Clcn3*$^{+/-}$ and *Clcn3*$^{-/-}$ mice only at 48°C and 50°C, but not at 52°C but still a faster reaction tendency is observed.

Adult *Clcn3*$^{-/-}$ mice have a faster reaction in the tail-flick test in all temperatures tested when compared with the wild type and *Clcn3*$^{+/-}$ (Figure 3.2A and 3.2B). The noxious response observed in the *Clcn3*$^{+/-}$ mice is similar to the one obtained in the control condition for all temperatures tested. When applying the formalin test in adult animals, the reaction to the noxious stimuli was greater in the *Clcn3*$^{-/-}$ for the acute phase, between 5-10 minutes and immediately after, a rising phase corresponding to the inflammatory response was observed over the whole recording period (15-40 minutes after injection) which significantly differs from the reaction observed in control mice.

In this experiment, differences were only observed in the licking reaction in the heterozygous mice at 30, 35, and 40 minutes when compared to the wild type (Figure 3.2C). By comparing both sets of experiments, P21 and P60, it can be concluded that the enhanced reaction of the *Clcn3*$^{-/-}$ mice is not only maintained but progress over time especially in the

inflammatory response observed in the formalin test. Pain experiments data are presented in Tables 3.1 and 3.2.

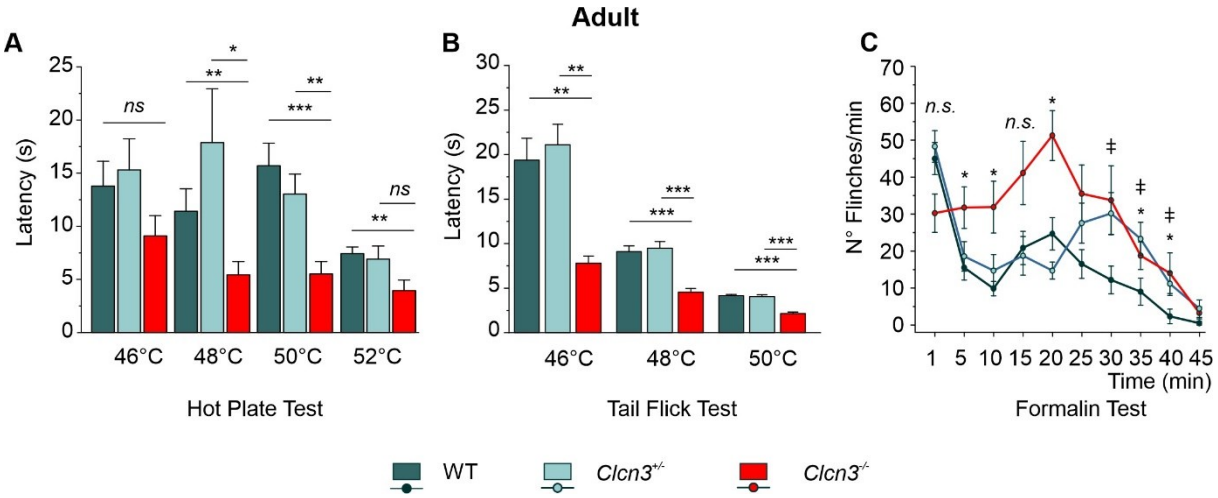

Figure 3.2. Acute thermal pain experiments in adult P60 mice show increased thermal sensitivity and significantly lower latencies in mutant than in WT animals. **A** Hot plate test experiment at different temperatures, WT (*n=11*); *Clcn3*$^{+/-}$ (*n=12*); *Clcn3*$^{-/-}$ (*n=13*). **B** Tail flick test at different temperatures, WT (*n=8*); *Clcn3*$^{+/-}$ (*n=8*); *Clcn3*$^{-/-}$ (*n=9*). **C** Formalin test applied to the animal's hind paw. WT (*n=6*); *Clcn3*$^{+/-}$ (*n=7*); *Clcn3*$^{-/-}$ (*n=8*). Significance levels are given as **p*<0.05, ***p*<0.01, ****p*<0.001. * *Clcn3*$^{-/-}$ differs from WT; ǂ WT differs from the heterozygous *Clcn3*$^{+/-}$.

These data show that the lack of ClC-3 in mice alters behavioral pain perception and highlights the importance of chloride/proton transporters in the regulation of pain signaling. Moreover, the observed increase in behavioral pain reaction in *Clcn3*$^{-/-}$ mice triggered by different noxious stimuli indicates an alteration in the specialized terminals from the sensory neurons that detect the noxious stimuli and at the modulatory process in the ascending spinothalamic pathway (Emery and Ernfors, 2020).

3.2 Deletion of ClC-3 *does not* alter the excitability of neurons in young animals

The observed alterations in behavioral pain perception in *Clcn3*$^{-/-}$ animal might arise from changes in the electrical properties of small-diameter unmyelinated DRG neurons. Membrane properties and action potential characteristics were therefore examined from isolated DRG neurons from P21 and P60, *Clcn3*$^{-/-}$, and wild type littermates through whole-cell patch-clamp recordings. Action potentials (AP) were measured under current-clamp configuration and triggered by injections of depolarizing currents rising from -70 pA up to +140 pA, for 1 second in 10 pA step increments. These experiments allowed evaluation of the passive

and active properties of the cell membrane such as the resting membrane potential (RMP), input resistance (R_{in}), and current threshold (rheobase), as well as the properties of the action potentials (Figure 3.3 and 3.4).

Although young *Clcn3*$^{-/-}$ mice exhibit a behavioral pain phenotype (Figure 3.1) the properties of the action potentials of cultured neurons, are not altered when compared with the wildtype littermates (Figure 3.3). There are no differences in the number of action potentials between wild type and mutant mice for any tested injected current amplitude (Figure 3.4A and 3.4B). The average of action potentials upon 100 pA and 200 pA current injection in both wild type and *Clcn3*$^{-/-}$ are 4 and 8, respectively. This protocol was performed starting from a hyperpolarizing current of -40 pA by 20 pA increments. These results were estimated from cells that elicited more than 3 action potentials, about 73.6% for wild type and 78.9% for mutant neurons. Input resistance (R_{in}) is higher in knock-out neurons than in wild type (WT 743.35±50.18 MΩ vs *Clcn3*$^{-/-}$ 1017.24±79.59 MΩ, MW p=0.007). Neither rheobase, which is defined as the minimal current required to evoke the first AP (Figure 3.4D), nor the resting membrane potential (Figure 3.4I) are altered.

Voltage threshold and amplitude are also not different from the control condition (Figure 3.4F and 3.4G). However, there is a significant increase in the after-hyperpolarization amplitude (AHP) in *Clcn3*$^{-/-}$ neurons (WT 23.98±1.23 mV vs *Clcn3*$^{-/-}$ 27.89±0.94 mV, t-test p<0.05). Moreover, following a depolarizing current step at fixed amplitude, around 34% of the measured cells showed a delay of around 100 ms before AP onset. The time to event is much longer in knock-out animals (WT 57.73±17.59 ms vs *Clcn3*$^{-/-}$ 228.51±53.74 ms, MW p=0.044).

Since the excitability of the neurons depends on a variety of factors associated with the properties of the membrane, the excitability index (EI in pA) described by Lazarus and Huang (2011) was estimated. Cultured *Clcn3*$^{-/-}$ DRG neurons from young animals have a lower EI value compared to wild-type cells (WT 0.058±0.004 pA vs *Clcn3*$^{-/-}$ 0.047±0.003 pA, t-test p=0.05), suggesting that mutant cells are more excitable. Since neither the AP threshold nor the RMP are significantly affected in *Clcn3*$^{-/-}$, the only parameter that produces a lower EI according to the equation is the input resistance of the cell membrane. However, only changes in the input resistance cannot fully explain the behavioral pain phenotype of *Clcn3*$^{-/-}$ mice. Action potential properties of young animals are summarized in Table 3.3.

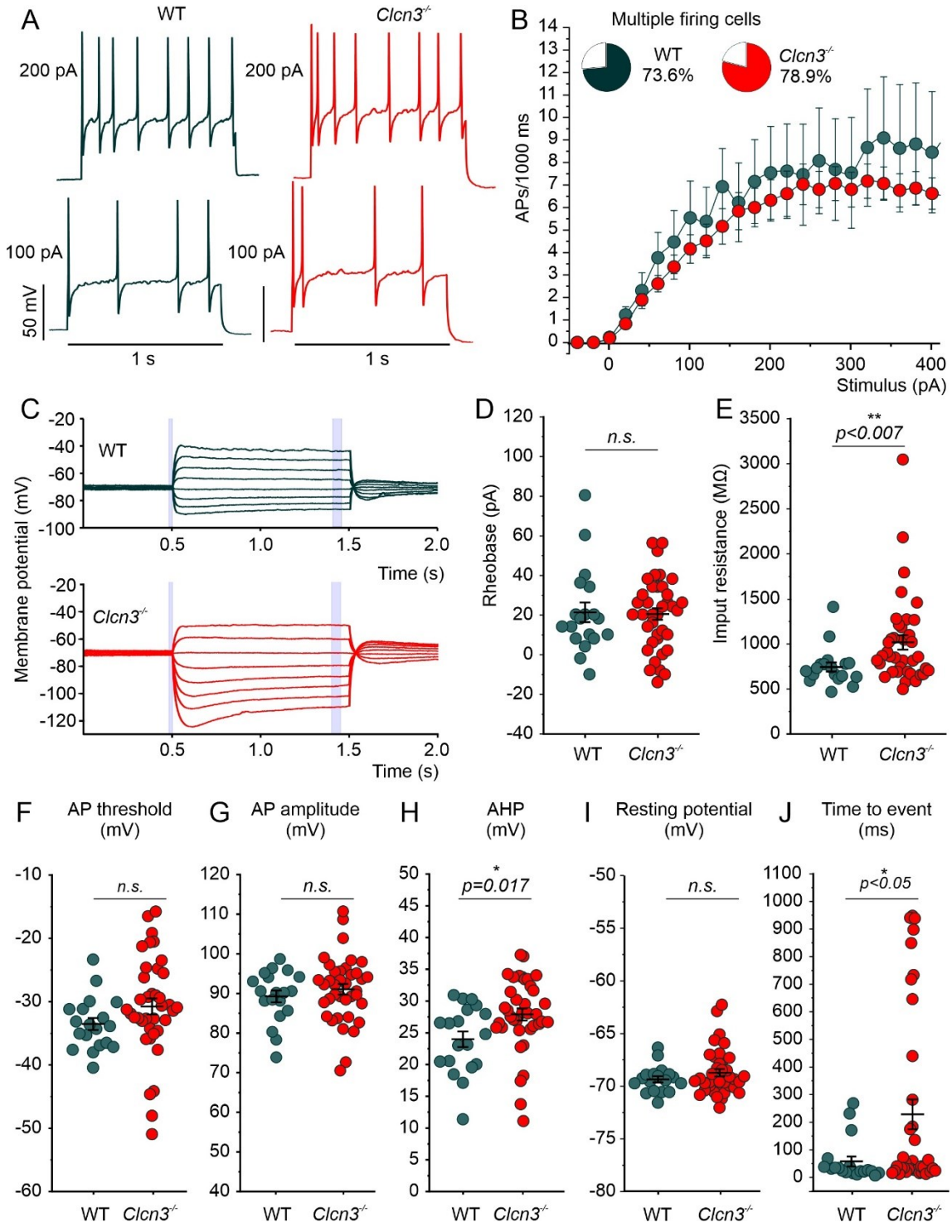

Figure 3.3. DRGs neurons from young *Clcn3*$^{-/-}$ animals show small changes in action potential properties. **A**. Representative traces of action potentials elicited by the current injection of 100 pA (lower traces) and 200 pA (upper traces) recorded from WT and *Clcn3*$^{-/-}$ neurons. **B**. Average firing frequencies are similar in both conditions after progressively increasing current pulses from -40 pA in 20 pA increments. Insert shows that 73,6 % of the WT and 78,9 % of the mutant cells exhibited repetitive firing. **C**. Representative traces of membrane potential upon hyperpolarized currents between -70 pA to 0 pA were used to calculate the passive properties of the membrane.

Purple bars within the traces show where the resting membrane potential (thin bar) and the input resistance (thick bar) were calculated. **D**. Current threshold necessary to elicit the first action potential is not altered (WT 24.63±5.12 pA vs *Clcn3*$^{-/-}$ 24.97±2.99 pA). **E**. Average input resistance is increased in *Clcn3*$^{-/-}$ DRG. **F.** Neither AP threshold nor (**G**) AP amplitude and (**I**) resting membrane potential are changed, despite the small but significant change present in the after-hyperpolarization amplitude AHP (**H**). **J**. Time to event in mutant cells is longer than in the control condition. Wild type (*n=19 cells*), *Clcn3*$^{-/-}$ (*n=38 cells*).

3.3 The excitability of dorsal root ganglia neurons is enhanced in adult *Clcn3*$^{-/-}$ mice

Action potential properties of *Clcn3*$^{-/-}$ in adult mice (P60) were then examined. Analysis of firing frequency shows an increased number of action potentials in the *Clcn3*$^{-/-}$ cells when compared to the wild type. For example, *Clcn3*$^{-/-}$ DRG neurons elicited on average a two-fold increase in the number of action potentials at 200 pA when compared to the wild type (Figure 3.4A). The number of measured cells that elicited more than 3 action potentials was comparable between phenotypes.

Consistent with an increased firing rate, the rheobase was significantly reduced in the *Clcn3*$^{-/-}$ DRG neurons (WT, 39.62±6.13 pA vs *Clcn3*$^{-/-}$, 17.67±2.86 pA, t-test $p<0.001$) (Figure 3.4D). Similar to young animals, deletion of ClC-3 in adult mice caused a significant increase in the input membrane resistance (R_{in}) in the *Clcn3*$^{-/-}$ cells when compared to the wild type (WT 746.15±67.41 MΩ vs 1144.85±81.95 MΩ, MW $p<0.001$), suggesting the presence of a large fraction of closed leak channels in *Clcn3*$^{-/-}$. These channels might increase neuronal excitability as is reflected by the changes in the rheobase.

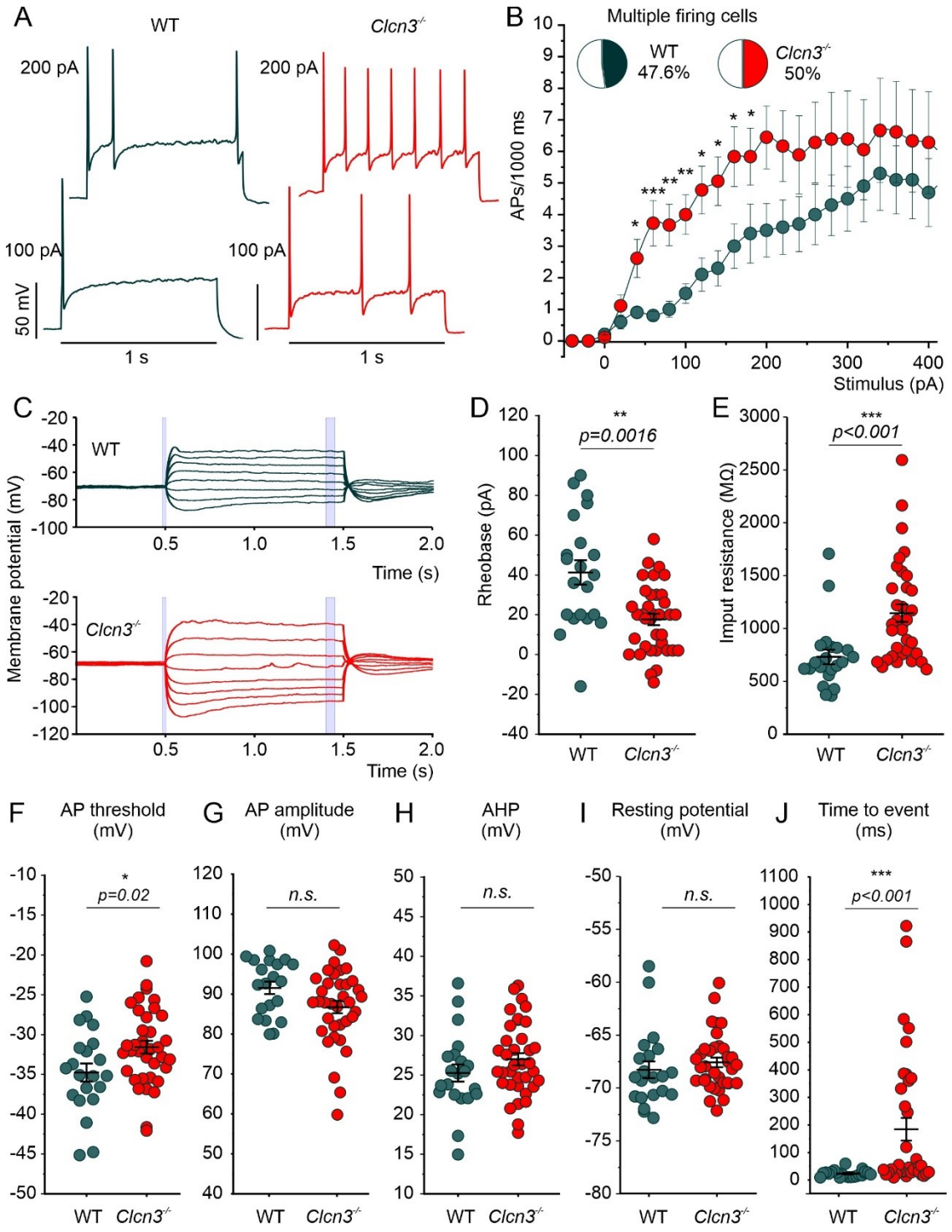

Figure 3.4. Ablation of ClC-3 changes the excitability of a population of small-diameter DRG neurons from adult mice. **A**. Representative traces of action potentials generated in WT and *Clcn3*$^{-/-}$ neurons by current injection of 100 pA (lower traces) and 200 pA (upper traces) for 1 second. **B**. Average firing frequencies show an increased rate on the *Clcn3*$^{-/-}$ after progressively increasing current pulses in the range between 40 and 180 pA. Insert shows the percentage of repetitive firing cells. **C**. Representative traces of membrane potential upon hyperpolarized currents between -70 pA and 0 pA were used to calculate the passive properties of the membrane. Purple bars

within the traces show where the resting membrane potential and the input resistance were calculated, respectively. **D**. Rheobase is significantly decreased in mutant neurons than in control neurons (WT 39.62±6.13 pA vs *Clcn3*$^{-/-}$ 17.67±2.86 pA, p=0.0016). **E**. Average input resistance is increased in *Clcn3*$^{-/-}$ DRG neurons (WT 746.15±67.41 MΩ vs *Clcn3*$^{-/-}$ 1144.85±81.95 MΩ, MW p<0.001), **F.** Mean of AP threshold is shifted to slightly more positive potentials in the *Clcn3*$^{-/-}$ neurons (WT -34.76±1.13 mV vs *Clcn3*$^{-/-}$, -31.58±0.80 mV, p=0.023). Neither the AP amplitude (**G**), AHP (**H**), nor resting membrane potential (**I**) are affected. **J**. Time to event in mutant cells is longer in mutant cells than in control condition. Wild type (*n=21 cells*), *Clcn3*$^{-/-}$ (*n=36 cells*).

Regarding the active properties of the action potentials, it could be observed that the AP threshold was significantly higher in the mutant neurons (Fig. 3.4F, around 3.18 mV towards more depolarized potentials, WT -34.76±1.13 mV vs *Clcn3*$^{-/-}$ -31.58±0.80 mV, t-test p=0.023). In contrast, the action potential amplitude, the after-hyperpolarization potential, and the resting membrane potential in the knock-out condition were not different from the control cells (Fig 3.4G-I). Similar to neurons from young animals, the excitability index EI suggests that DRG neurons from adult *Clcn3*$^{-/-}$ mice are more excitable than wild-type cells (WT 0.074±0.009 pA vs *Clcn3*$^{-/-}$, 0.042±0.003 pA, MW p=0.0017). Together, this set of data indicate changes in the excitability of *Clcn3*$^{-/-}$ DRG neurons contribute to the alteration on Behavioral pain n *Clcn3*$^{-/-}$ mice. All the action potential properties measured from adults are listed in Table 3.4.

3.4 Action potential properties are not altered in ClC-3^{E281Q} knock-in (*Clcn3*^{E281Q})/ClC-4 knock-out (*Clcn4*$^{-/-}$) mouse model

The mechanism of synaptic transmission regulation by ClC-3 in the CNS remains unclear. ClC-3 has been proposed to enhance the excitatory postsynaptic potentials (Wang et al., 2006), to regulate the amount of neurotransmitter in synaptic vesicles (SV) and their release probability (Guzman et al., 2014) as well as to modify the rate of SV acidification (Riazanski et al., 2011). These hypotheses suggest a direct role of the transport Cl^-/H^+ function in SV. However, ultra-definition subcellular proteomics of the fraction-containing synaptic vesicles revealed a low copy number of ClC-3, indicating that either ClC-3 is present only in a small subpopulation of SVs or possibly not present at all (Taoufiq et al., 2020), suggesting an indirect role of ClC-3 in synaptic transmission.

To test whether the transport activity of ClC-3 is essential for the regulation of cell excitability in DRG neurons, a knock-in mouse model, in which the chloride transport activity of ClC-3 was abolished, was generated. In this animal, the conserved glutamate at position 281 in ClC-3a (339 and 312 in ClC-3b and ClC-3c, respectively) was substituted by glutamine.

Since this substitution abolishes chloride transport but leaves the ability to heterodimerize with ClC-4 unaffected (Guzman et al., 2017), and ClC-4 mRNA expression is high in the DRG in adult mice (Figure 3.5), a double mutant *Clcn3*^{E281Q}/*Clcn4*$^{-/-}$ was then generated by crossbreeding both transgenic lines over two generations, to obtain a double homozygous *Clcn4*$^{-/-}$ (on chromosome 8) and *Clcn3*^{E281Q} (on chromosome 7) mice.

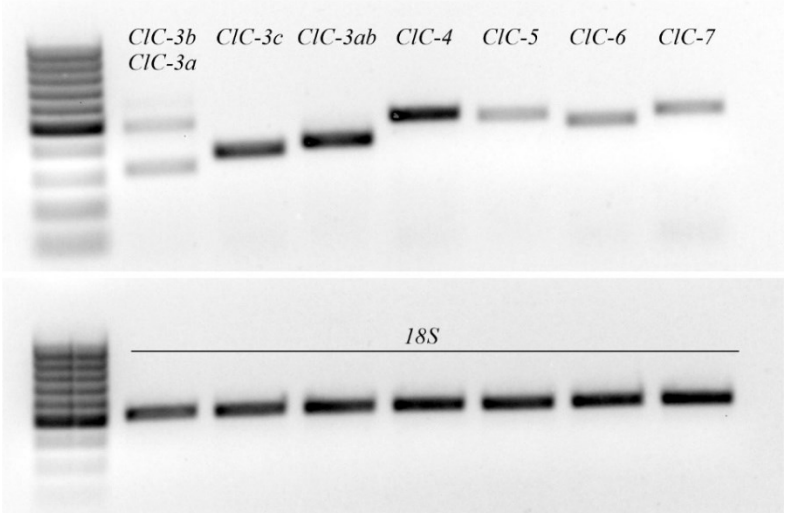

Figure 3.5. DNA expression of the different ClC chloride/proton exchangers in adult DRG. 18S was used as a housekeeping gene. The set of primers used in this experiment are listed in Table 2.7.

Both *Clcn4*$^{-/-}$ and *Clcn3*^{E281Q} knock-in have no obvious phenotype. They develop normally, show comparable bodies to the wild type, and do not exhibit hippocampal degeneration. Unexpectedly, *Clcn3*^{E281Q} presents a loss of photoreceptors before the 21st day of life, suggesting the absence of ClC-4 in this tissue. In contrast, the double mutant *Clcn3*^{E281Q}/*Clcn4*$^{-/-}$ shows enhanced motor activity, loss of photoreceptors, and neuronal degeneration of the hippocampus, similar to *Clcn3*$^{-/-}$ mice (Figure 3.6).

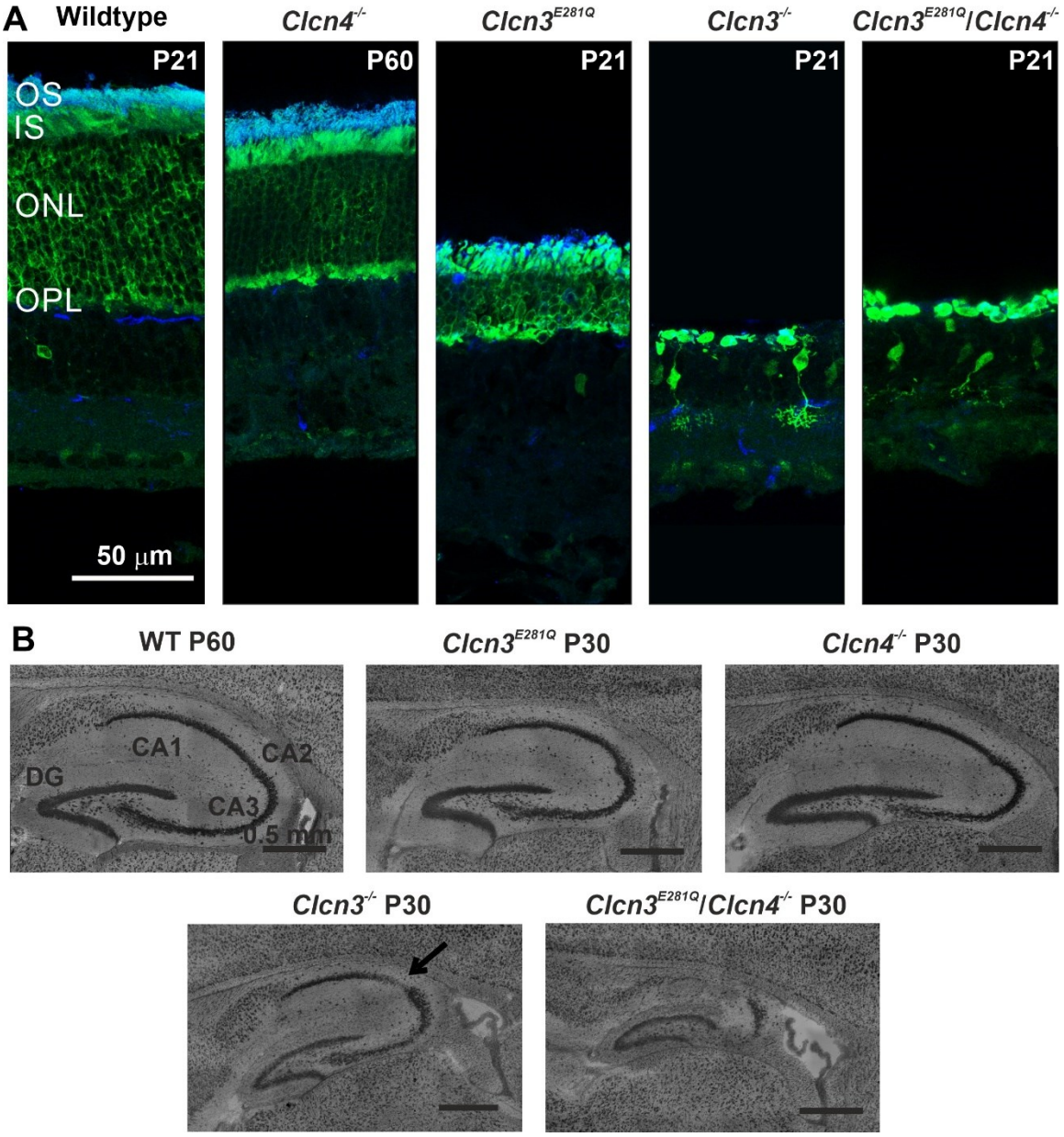

Figure 3.6. The onset of hippocampal and retinal degeneration across chloride/proton exchangers phenotypes. A. Confocal pictures of the retinal layers in different mouse lines show no degeneration in the *Clcn4*$^{-/-}$. However, In the knock-in mouse *Clcn3*^{E281Q,} most of the photoreceptors are lost at postnatal day 21. The greater effect is observed in the *Clcn3*$^{-/-}$ and in the *Clcn3*^{E281Q}*/Clcn4*$^{-/-}$, where the nuclear layer is already lost at P30. B. Confocal pictures of the onset of hippocampal degeneration in *Clcn3*$^{-/-}$ and the *Clcn3*^{E281Q}*/Clcn4*$^{-/-}$. Scale bar 50 µm for retina and 0.5 mm for hippocampal pictures. Confocal pictures were taken by Dr. Jana Gehlen from the Institute for Biological Information Processing (IBI-1).

Surprisingly, the electrical properties of the DRG neurons from adult *Clcn3*^{E281Q}*/Clcn4*$^{-/-}$, *Clcn3*^{E281Q,} and *Clcn4*$^{-/-}$ were similar to the observed in wild type condition (Figure 3.7). AP frequencies in all three mutant mice are slightly higher than in the control condition. Only a

small increment in the number of AP events can be observed; nevertheless, significant differences were not found in any of the current injection steps. Moreover, the input resistance and the current threshold in DRG neurons were not different from wild type for all three mutants, despite being the most affected parameters in the *Clcn3*$^{-/-}$. Other action potential properties such as AP threshold, AP amplitude, AHP amplitude, time to event were similarly unaffected (Figure 3.7).

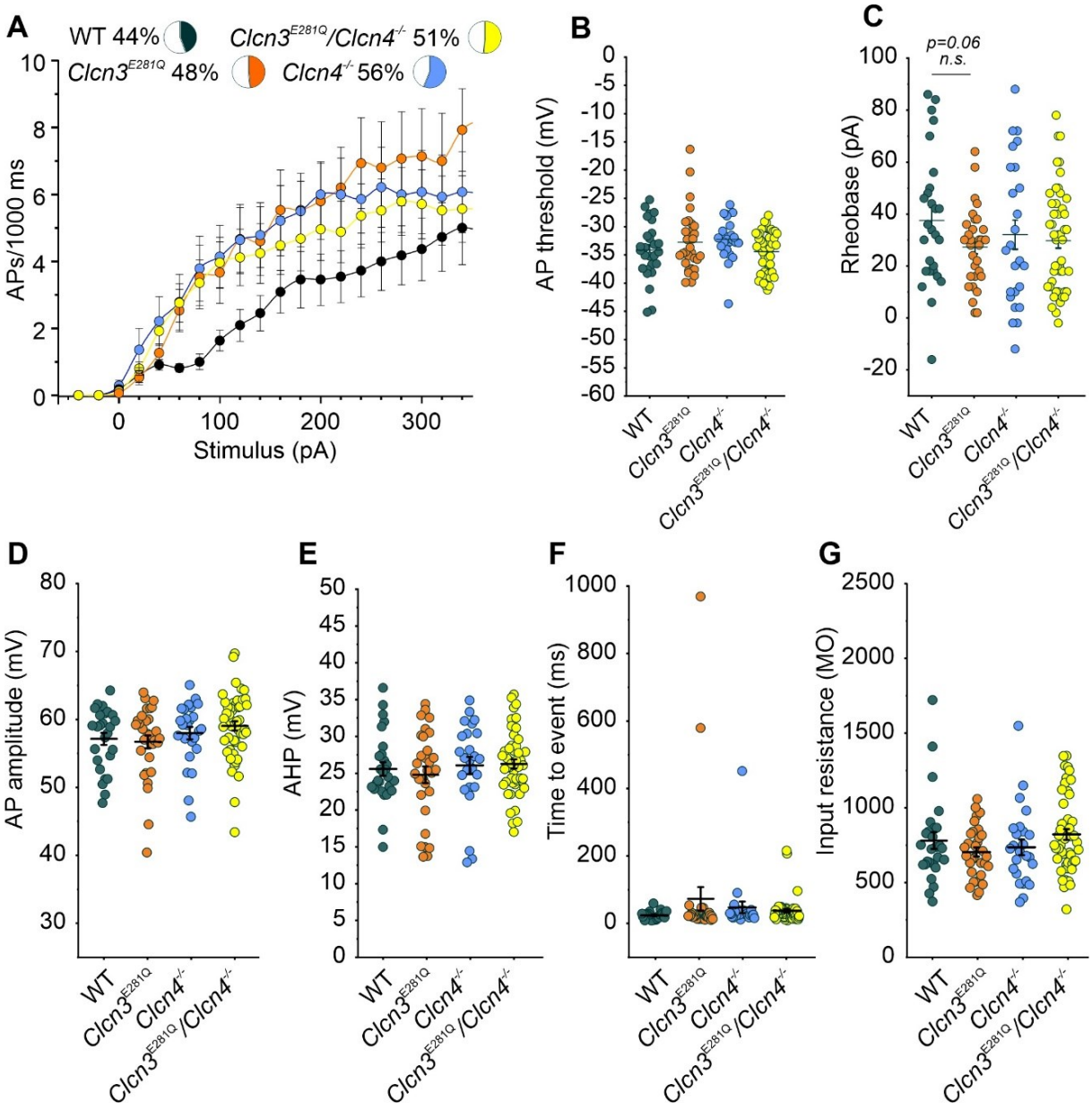

Figure 3.7. Comparison of action potential properties of *Clcn3*^{E281Q}, *Clcn4*$^{-/-}$, and the double mutant *Clcn4*$^{-/-}$/*Clcn3*^{E281Q} mice. **A**. Evaluation of the AP frequencies shows an increase in the number of action potentials in these mutant neurons, but significant differences were not observed. **B**. AP threshold is not altered in these

phenotypes as observed in the *Clcn3*$^{-/-}$ mice. **C**. Reduction of the rheobase is not observed in the double mutant *Clcn3*^{E281Q}/*Clcn4*$^{-/-}$, nor in the *Clcn4*$^{-/-}$, but a small reduction is displayed in the *Clcn3*^{E281Q}. Properties as AP amplitude (**D**), AHP (**E**), the latency of action potentials upstroke (**F**), and input resistance (**G**) are not altered in any of the phenotypes evaluated in this experiment. P60 *WT (n=27); Clcn3*^{E281Q} *(n=31); Clcn4*$^{-/-}$ *(n=25); Clcn3*^{E281Q}/*Clcn4*$^{-/-}$ *(n=49)*.

These results suggest that the chloride transport activity, an essential feature of ClC exchangers, is not directly involved in the regulation of neuronal excitability in DRG. These observations raise the question of whether ClC-3 has also the ability to interact and/or interfere in the recycling pathway of other important membrane proteins such as voltage-gated sodium and potassium channels that play an essential role in the electrical properties of the neurons.

3.5 ClC-3 ablation alters Na^+ channel densities in DRG neurons

Voltage-gated sodium channels (VGSC) are essential for the generation of the action potentials in excitable cells (Hodgkin and Huxley, 1990). Na^+ currents are crucial for the initiation and propagation of APs, and alterations in channel density and function of the different VGSC isoforms occur in many pain disorders (Bernal, 2018; Dib-Hajj et al., 2010; Lampert et al., 2010) such as thermal hyperalgesia and mechanical allodynia after peripheral nerve injury (Berta et al., 2008; Cummins and Waxman, 1997). Here, the surface membrane expression of Na^+ channels in the absence of ClC-3 in adult mice was evaluated.

Small diameter C-type DRG neurons preferentially express $Na_v1.7$, a fast-inactivating isoform that is sensitive to nanomolar concentrations of a neurotoxin from the pufferfish, tetrodotoxin (TTX) (TTX-S). These neurons also express $Na_v1.8$ and $Na_v1.9$ subunits with slow inactivating and TTX resistant (TTX-R) currents (Dib-Hajj et al., 2010; Rush et al., 2007). To characterize the TTX-S and TTX-R sodium current components, patch-clamp experiments in the presence and absence of 300 nM of TTX were performed. To avoid space clamp artifacts raised by the neurite network, experiments were performed between 12 and 24 hours after plating of the neurons; moreover, neurons without obvious neurite processes were selected for electrophysiological recordings. Neurons were held in voltage-clamp mode at -70 mV for about 4-5 minutes, then for 1 minute at -100 mV before starting a voltage steps protocol. First, inactivating current were measured at -10 mV for 50 ms after a test pulse of 5 mV increments starting from -100 mV to +30 mV applied for 500 ms.

The experiments confirmed that wild-type and *Clcn3*$^{-/-}$ DRG neurons express both TTX-S and TTX-R sodium currents. The peak amplitude of the total Na^+ currents was slightly increased in *Clcn3*$^{-/-}$ compared to wild type neurons. Upon application of 300 nM of TTX, a reduction of about 40% of the TTX-resistant current was observed in the *Clcn3*$^{-/-}$ neurons compared to the wild type (Figures 3.8). This reduction was pronounced within the voltage range of -25 to +30 mV, where $Na_v1.8$ displays its peak of maximal current amplitude (Han et al., 2015). This result suggests that the densities of $Na_v1.8$ in DRG neurons are selectively affected by the absence of the ClC-3.

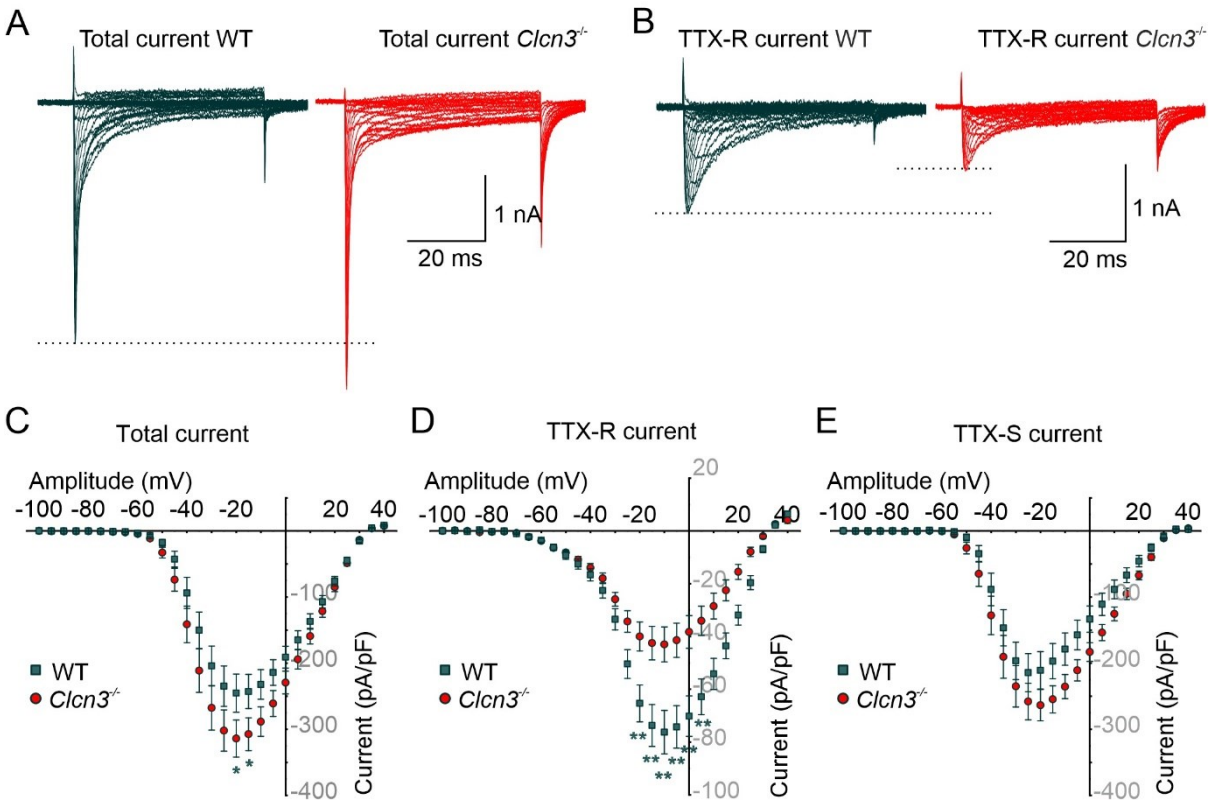

Figure 3.8. Whole-cell patch-clamp recordings of Na^+ currents in cultured WT and Clcn3$^{-/-}$ DRG neurons. **A**. Representative traces of total current in the WT and *Clcn3*$^{-/-}$, and **B.** TTX-resistant currents. **C**. Current-voltage relationship of total Na^+ currents, **D** after application of 300 nM of TTX (TTX-resistant). **E**. Current-voltage relationship of TTX-sensitive Na^+ currents obtained by subtracting the total current from ***a***, minus the TTX-resistant current from ***b***. Currents were elicited by voltage steps between -100 mV and 40 mV. Significance levels are given as *p<0.05, **p<0.01: WT (n=*24*), *Clcn3*$^{-/-}$ (n=*24*).

To evaluate the current mediated by sodium channels sensitive to TTX, a subtraction of the TTX-R current from the total Na^+ current was applied to obtain the $Na_v1.7$ current component. This calculation revealed a small increase in the peak of $Na_v1.7$-mediated Na^+

current in the *Clcn3*$^{-/-}$ cells (around 20%) (Alexandrou et al., 2016). Changes in the Na^+ current densities may account for the lower current threshold observed in current-clamp recordings (Figure 3.4D) and might explain the increased excitability observed in *Clcn3*$^{-/-}$ DRG neurons. The corresponding data is presented in Table 3.5.

Alternatively, the change in the Na^+ current densities observed in the *Clcn3*$^{-/-}$ DRG neurons might be caused by a modified voltage-dependence of gating. To evaluate whether ClC-3 ablation induces changes in the biophysical properties of the VGSC, the voltage-dependence of activation and the steady-state inactivation of the sodium current components were measured. Macroscopic sodium currents show no apparent shift in the voltage dependence of channel activation (Figure 3.9A). The half-maximal of activation is presented as insets in Figure 3.9A. TTX-resistant Na^+ channels from mutant DRG neurons show a small leftward shift in half-maximal current activation in mutant DRG neurons (Figure 3.9B) while no differences were observed for the TTX-sensitive Na^+ currents (Figure 3.9C). The tail current was obtained at -10 mV after the test pulses and plotted against the voltage.

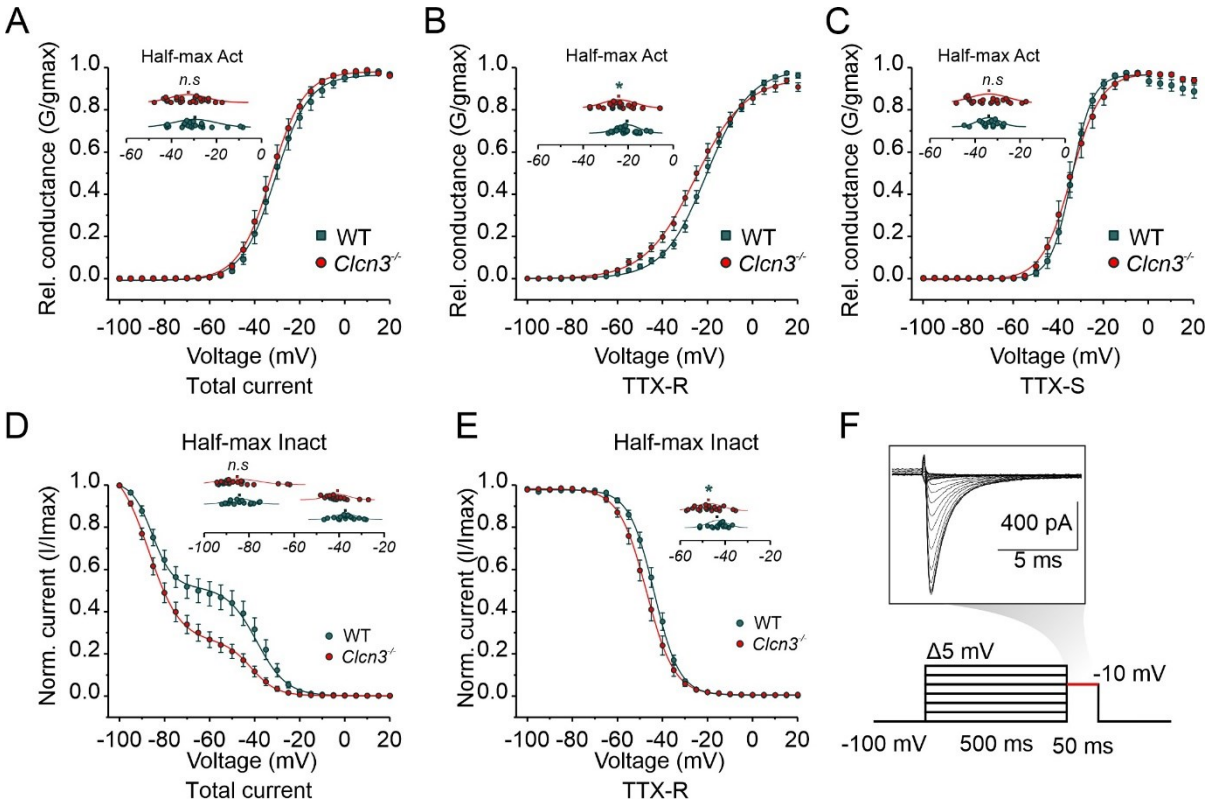

Figure 3.9. Biophysical properties of Na_v channels from in small-diameter DRG neurons. **A-C.** Estimation of the voltage dependence of activation in WT and *Clcn3*$^{-/-}$ plotted and fitted with a single Boltzmann equation for the total Na^+ currents (**A**), for the TTX-R currents (**B**); and for the TTX-S currents (**C**). Insets display the half-max of

activation for each cell. **D-E.** The steady-state of inactivation for the total Na^+ currents plotted and fitted with a double Boltzmann equation (**D**), and for the TTX-R currents fitted with a single Boltzmann equation (**E**). A leftward shift of 4.3 mV was found in the *Clcn3*$^{-/-}$ when compared to the control. Insets display the half-max of inactivation for each cell. **F**. Voltage-clamp protocol to measure sodium current inactivation consisting of a test pulse between -100 mV and 20 mV of 500 ms, followed by a short pulse of 50 ms at -10 mV. Significance levels are given as *p<0.05, WT (*n=18*), *Clcn3*$^{-/-}$ (*n=22*).

In DRG neurons from the knock-out mice, inactivation was faster only in the TTX-R component due to a small shift of the voltage dependence of steady-state channel inactivation towards more hyperpolarized potentials, but not in the component associated with TTX-S currents (Figure 3.9D and 3.9E). Furthermore, Western blot experiments showed no obvious reduction at the total protein level of the $Na_v1.8$ subunit in the *Clcn3*$^{-/-}$ roots when compared to the wild type expression. Taken together, these observations suggest that ClC-3 deletion does not interfere with *de novo* synthesis of $Na_v1.8$ in DRG neurons but rather with its trafficking (Figure 3.10).

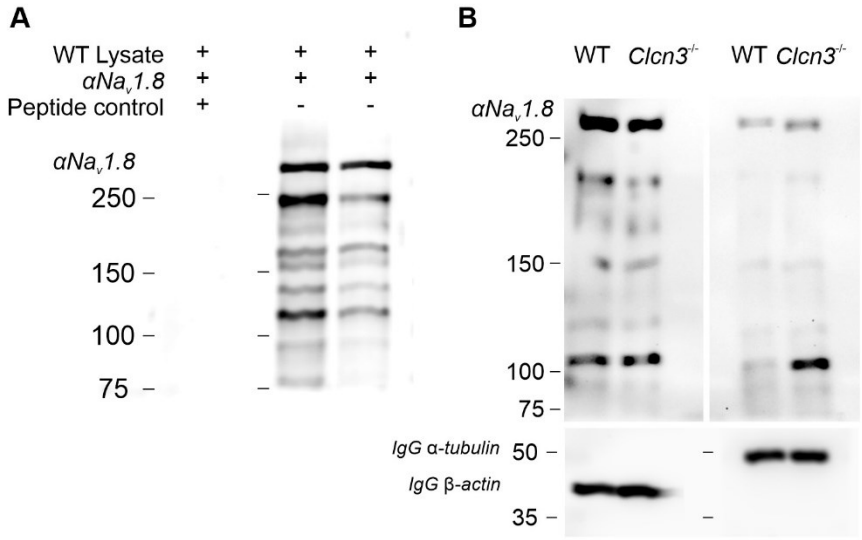

Figure 3.10. Sodium channel $Na_v1.8$ protein expression in DRG from WT and *Clcn3*$^{-/-}$. A Control experiment was used to test the specificity of the antibody. The band around 260 kDa corresponds to the $Na_v1.8$. B. Comparison of two independent experiments using lysates from dorsal roots ganglia from three animals shows no apparent reduction in the total protein expression in *Clcn3*$^{-/-}$ when compared to the control condition.

3.6 ClC-3 deletion alters plasma membrane densities of K^+ channels

Potassium channels (K_v) mediate hyperpolarizing K^+ effluxes across the plasma membrane that oppose cation influx, hyperpolarize the neuronal membrane potential and limit neuronal excitability (Tsantoulas and McMahon, 2014). They are important for setting the AP peak and the after-hyperpolarizing potentials in neuronal transmission. Changes in the surface expression of some members and changes in their biophysical properties have been associated with altered nociception (Conner et al., 2016; Duan et al., 2012; Laumet et al., 2015). To evaluate whether the surface membrane expression of K_v's is altered in *Clcn3*$^{-/-}$ adult mice, potassium currents were measured in DRG neurons. To get reliable measurements and to reduce space clamp errors, recordings were performed within the first 36 hours after neuronal plating.

Outward rectifier potassium currents in C-type DRG neurons from adult *Clcn3*$^{-/-}$ were larger than in wild-type cells. This increase was more pronounced at positive voltages. Wild type and mutant neurons differ in inactivation kinetics, most likely due to the different population of potassium channels present in different types of nociceptive neurons for example IB4+ and IB4-. Some currents activate slowly and reach the steady-state at the end of the applied protocol, but others reach the maximum within the first 30 ms but decayed faster (Figure 3.11A). 4-AP is known to block A-type fast-inactivating voltage-gated K^+ currents (I_A) and the remaining current corresponds to slow-inactivating voltage-gated K^+ currents (I_D) as well as delayed rectifier voltage-gated K^+ currents (I_K). To study the contribution of these groups of K^+ channels to the observed whole-cell currents, a perfusion solution containing 5 mM of 4-aminopyridine (4-AP) after the first measurement was applied. At a positive voltage range, I_D and I_K currents are larger in neurons from adult *Clcn3*$^{-/-}$ mice when compared to the wild type (Figure 3.11B). In contrast, I_A steady-state currents were not different among phenotypes. These currents are characterized by faster kinetics of activation and inactivation and are obtained by subtracting I_D and I_K from the total current ($I_A = I_{total} - (I_D + I_K)$, Figure 3.11C).

DRG neurons not only express potassium channels with outward currents but also inward rectifier potassium channels ($K_{ir}2.3$ and $K_{ir}2.4$) (Busserolles et al., 2020) or $K_{ir}3.1$ which can be activated in mice peripheral sensory neurons following nerve injury (Seitz et al., 2021). K^+ measurements were also performed at hyperpolarized potentials in the sensory neurons with a slightly modified driving force for potassium (Table 2.9 and 2.10, with a holding potential

of -50 mV). Electrophysiological recording of the inward rectifier potassium channels showed small currents of about 300 pA measured 5 ms before the end of the test pulse at the lowest potential applied (-160 mV, Figure 3.11D). Current-voltage relationships are not different between wild type and mutant DRGs (Table 3.6). Thus, these results suggest that ClC-3 selectively regulates the plasma membrane expression of the slow-inactivating voltage-gated K^+ currents.

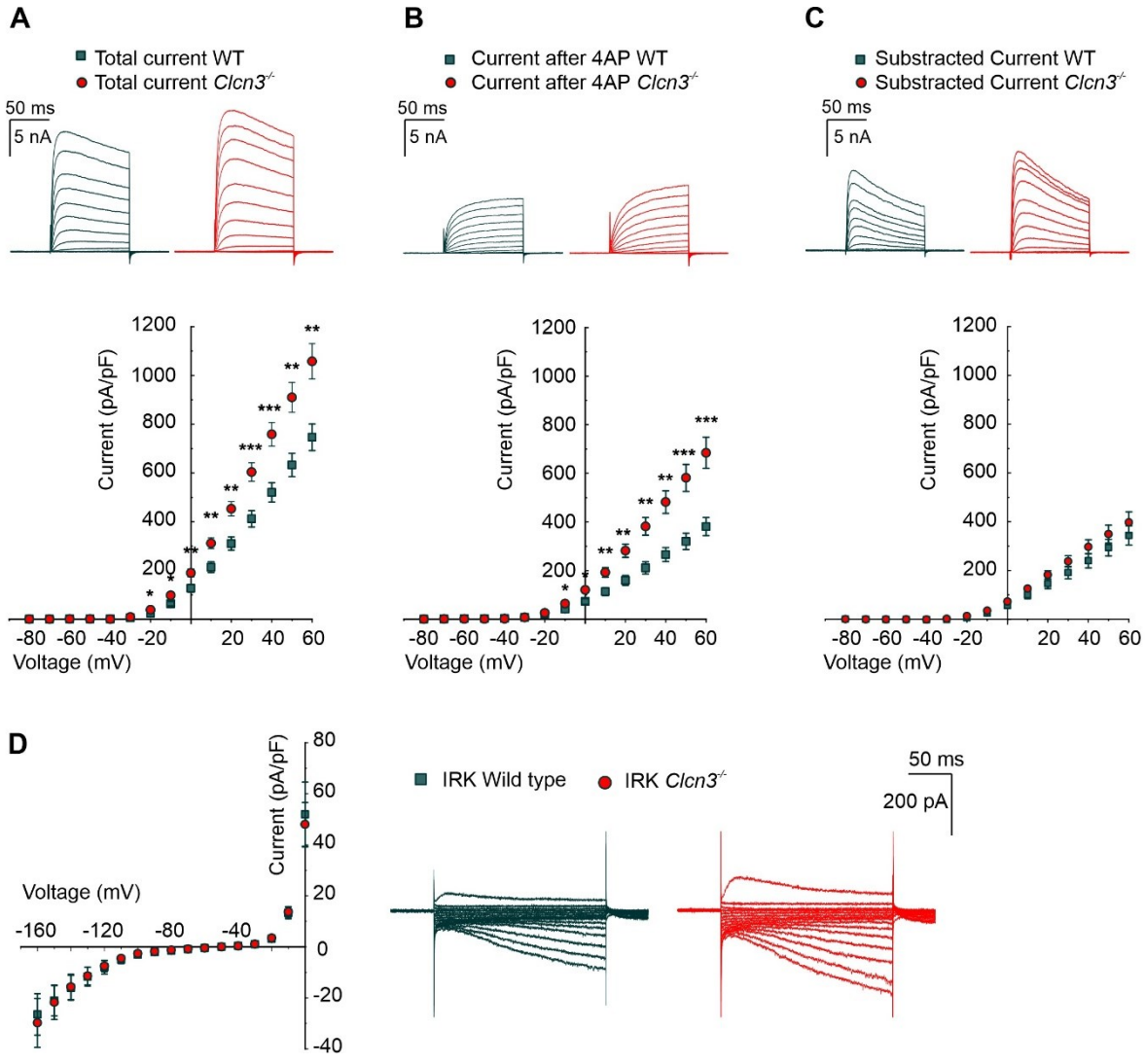

Figure 3.11. Whole-cell patch-clamp recordings of Kv currents present in small-diameter DRG neurons for WT and *Clcn3*$^{-/-}$ DRG neurons. **A**. Representative recordings of total potassium current densities recorded from WT (in blue) and *Clcn3*$^{-/-}$ (in red) DRG neurons. **B**. Slow inactivating K^+ currents obtained from the same neuron shown in (A), after application of 5 mM of 4-AP, a compound that blocks fast inactivating K^+ channels. Note that the total, as well as the slowly inactivating K^+ mediating current, are increased in the mutant cells. **C**. Current obtained by subtracting the slow inactivating (B) from the total current (A) showing the fast-inactivating K^+ currents in WT and *Clcn3*$^{-/-}$ showing no differences between them. **D**. IV-relationship and representative recordings

of inward-rectifying potassium currents obtained from small DRG neurons by applying voltages from 0 mV to -160 mV, show no differences between both cell types. Significance levels are given as *p<0.05, **p<0.01, and ***p<0.001. For outward currents WT ($n=16$), *Clcn3*$^{-/-}$ ($n=20$). For IRK currents WT ($n=15$), *Clcn3*$^{-/-}$ ($n=24$).

3.7 The absence of ClC-3 does not affect the neuronal viability in the dorsal root ganglia

The absence of ClC-3 can cause severe degeneration in some regions of the brain such as the hippocampus and the layer of photoreceptors of the retina. However, it is not known whether the different populations of neurons within the dorsal root ganglia and the spinal cord are also affected by ClC-3 deletion. DRGs from the L2 to the L4 were extracted, and 20 µm thick sections were stained against the neuronal marker NeuN, with Isolectin B4 (IB4) and with the calcitonin-gene-related peptide (CGRP). IB4 is a marker from the plant *Griffonia simplicifolia* that binds galactose residues on the cell surface and Golgi apparatus of small DRG neurons; while CGRP is one of the most abundant peptides produced in peripheral neurons and together with the Substance P are key players in neurogenic inflammation (Priestley, 2009).

Representative confocal images immunohistochemically labeled with the different antibodies from wild type and *Clcn3*$^{-/-}$ DRG are shown in Figure 3.12A. Immunohistochemical analysis using NeuN staining reveals no differences in the total number of neurons within the dorsal root ganglions from wild type and *Clcn3*$^{-/-}$ animals (Figure 3.12B(a)). However, IB4 positive cells are more abundant than those expressing CGRP in both, wild type as well as *Clcn3*$^{-/-}$. The percentage of IB4 positive from the total number of neurons positive for NeuN was not significantly different. Similar results were observed in the percentage of cells labeled with CGRP from the total number of neurons labeled with NeuN Figure 3.12B(*b*-*c*). NeuN positive neurons that were neither labeled with IB4 nor with CGRP were also counted (Figure 3.12B(*d*)). The immunohistochemical analysis demonstrates that the lack of the ClC-3 does not lead to neuronal loss in the dorsal root ganglions (Table 3.7).

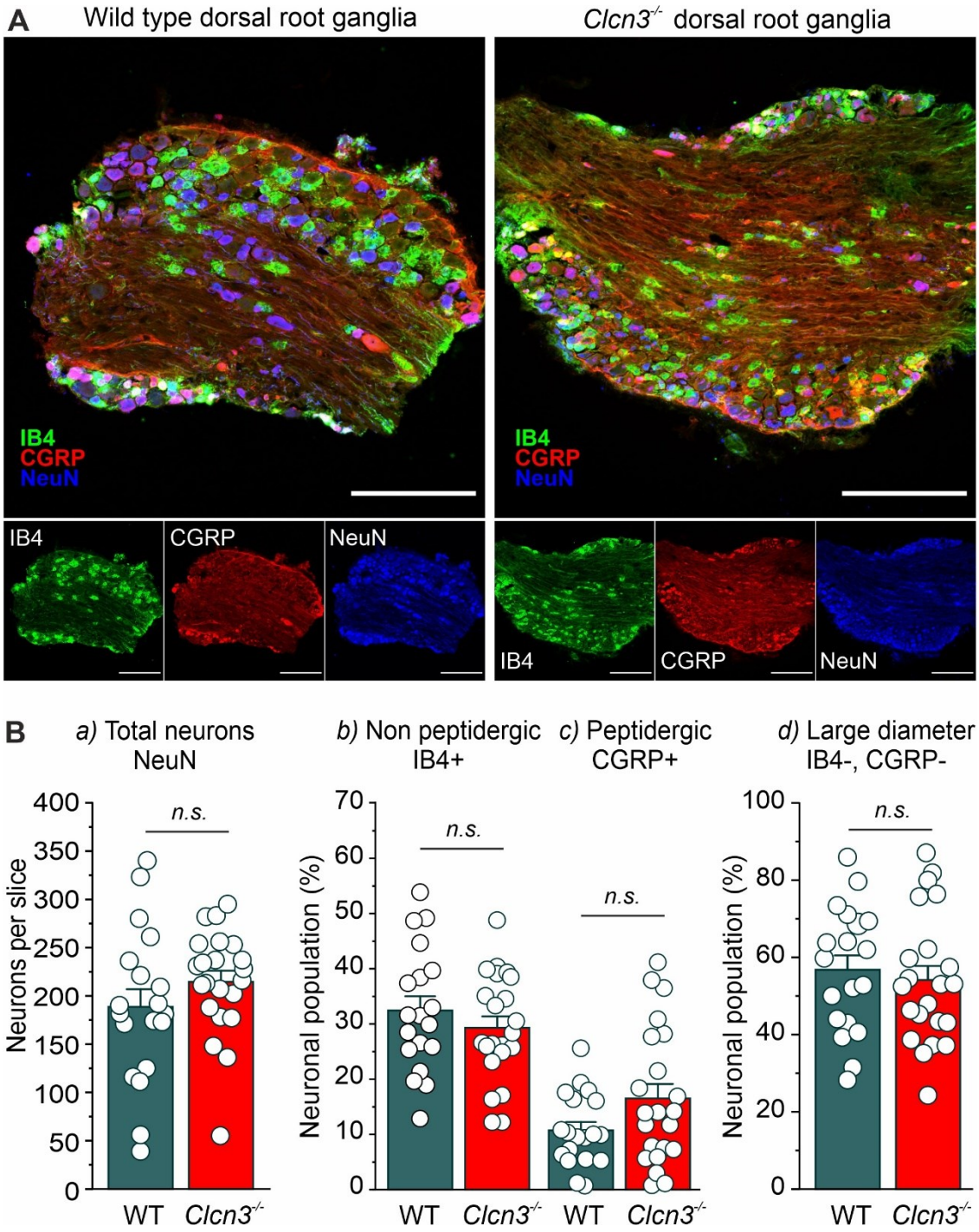

Figure 3.12. Immunohistochemical analysis of neuronal population within the dorsal root ganglion in *Clcn3*$^{-/-}$ mice. **A**. Representative confocal pictures of dorsal root ganglia from wildtype and *Clcn3*$^{-/-}$ stained with three antibodies NeuN (blue channel), IB4 non-peptidergic small-diameter neurons (green channel), and CGRP peptidergic neurons (red channel). **B**. Quantitative analysis of the total neuronal count does not show differences between the phenotypes neither the number of small-diameter neurons positive for IB4 nor those positive for CGRP were significantly different. The experiment was carried out with three different mice and at least two DRG on each one. Scale bar 200 µm.

3.8 Evaluation for neuronal viability in the dorsal horn of the spinal cord (DHSC)

Cross-sections of the lumbar spinal cord from wild type and *Clcn3*$^{-/-}$ mice show similar numbers of neurons from layers I to IV of the DHSC (Figure 3.13). These layers are characterized by receiving the nociceptive (lawyers I and II) and non-nociceptive (layers I, IV, and V) information from the small- and medium and large-diameter DRG neurons respectively (Stucky, 2007). Neurons were stained against NeuN (red channel) and counterstained with a nuclear marker TO-PRO™-3 (blue channel) and with anti-C-C motif chemokine ligand 2 (CCL2, green channel). Automated quantitative analysis of the number of neurons and the expression levels of CCL2 was performed using a custom-made pipeline in CellProfiler™. Figure 3.13B also depicts the boundaries of the dorsal horn (dashed line) obtained using the different proportions of cells labeled with NeuN and TO-PRO and delineated according to the Allen Brain Atlas of the Mouse Spinal cord (Lein et al., 2007).

Confocal pictures permitted an accurate quantification of the CCL2 fluorescence intensity in both animal models. CCL2 is a protein that, once is secreted, acts as a chemotactic factor to attract monocytes, CD4+ T cells, natural killer cells, and CCR2 expressing cells. Its expression is increased under inflammatory circumstances or injury to attract leukocytes to mediate defense, cytokine release, and repair (Gschwandtner et al., 2019). Higher expression of CCL2 in DRG neurons as well as in the spinal cord has been associated with inflammatory pain and hypersensitivity (Illias et al., 2018; Menetski et al., 2007). Dorsal horns from mutant tissue display 28% high mean fluorescence intensity than samples from wild type (Table 3.7). Fluorescence intensity was calculated using NeuN positive neurons. Additionally, the neuronal processes expressing CCL2 measured as a percentage of the area of incidence were quantified (Figure 3.13B, white arrows). The area covered by CCL2 was increased in the *Clcn3*$^{-/-}$ dorsal horn but samples taken from wild-type mice show few or almost no CCL2 positive processed (Figure 3.13C) as observed in the representative confocal pictures. Pictures were obtained from wild type and subsequently from *Clcn3*$^{-/-}$ slices with the same acquisition conditions.

In contrast to the clear neurodegeneration observed in the CNS, neither DRG nor in DHSC, are affected by the ClC-3 deletion, suggesting a different mechanism of actions of ClC-3 between these neuronal tissues. The higher expression of CCL2 in the *Clcn3*$^{-/-}$ dorsal horn might contribute to hyperalgesia in mutant mice since upregulation of this factor contributes to the

release of other pro-and anti-inflammatory cytokines, that in turn drive in microglia activation (Mika et al., 2013).

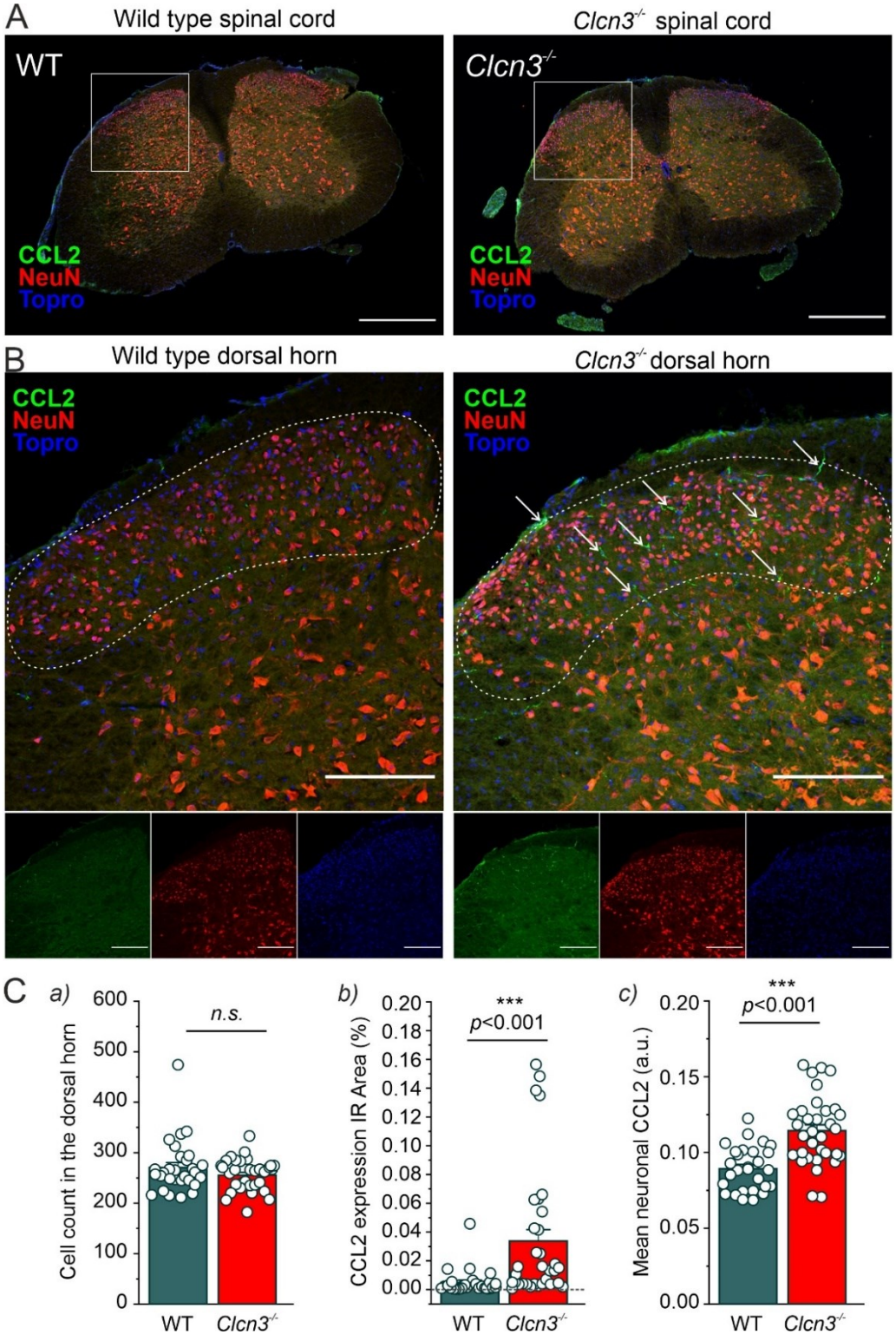

Figure 3.13. Immunohistochemical analysis of neuronal viability of DHSC in the *Clcn3*$^{-/-}$. **A**. Section of the lumbar spinal cord from both animals was stained against CCL2 (green), NeuN (red), and TO-PRO (nuclei, in blue). Scale

bar 500 µm. **B**. Layers of the dorsal horn are limited (dashed line) to perform quantitative analysis. Scale bar 150 µm. **C**. Cell counting on the dorsal horn shows no differences between phenotypes (a). Neuronal expression of the CCL2 shows a significant increase in the area of incidence (b) and the mean fluorescence intensity in the *Clcn3*$^{-/-}$ (c) when compared to the wild type. Each dot represents a single dorsal horn. A minimum of 3 animals was used per condition. At least 6 slices obtained from the lumbar section from the same animal were used. Sections from the same animal were obtained at least 100 µm apart. WT (n=29); *Clcn3*$^{-/-}$ (n=33). Significance levels are given as ***p<0.001, *n.s*., not significant. * *Clcn3*$^{-/-}$ differs from WT.

3.9 *Clcn3*$^{-/-}$ mice exhibit an increase in the number of reactive microglia at the dorsal horn of the spinal cord

Glial cells play an important role in modulating neuronal activity and neuronal excitability in different models of nociceptive pathologies. Glial cells are composed of around 5- to 10% of microglia and macroglia, which include astrocytes and oligodendrocytes (Vallejo et al., 2010). They exhibit morphological and physiological changes at different tissue upon injury, neuropathic and inflammatory pain, facilitating isolation of injured cells and eliminating potential pathogens. Glial activation can be defined as changes in proliferation, hypertrophy, production, and release of inflammatory mediators, enhanced expression of some proteins as glial fibrillary acidic protein (GFAP), or migration of macrophages (Lemes et al., 2018; Mika et al., 2013; Vallejo et al., 2010). Microglia activation can be differentiated in two phenotypes M1, pro-inflammatory or M2, anti-inflammatory. Both can be assessed by immunohistochemical analysis using antibodies targeting cell surface markers shared by microglia and macrophages such as CD11b, Iba-1, and CD68 (Lan et al., 2017).

Immunohistochemical analyses were performed to test whether glial cells in the spinal cord of the *Clcn3*$^{-/-}$ knock-out mouse are activated. 20 µm sections were taken every 100 µm apart from each other from the ticker segment of the spinal cord at the level of the T11 until L2 receives projections from the DRGs located downstream of the L1-L6. Sections were stained against GFAP and CD11b a protein from the integrin family usually expressed on the surface of monocytes, neutrophils, natural killer cells, granulocytes, and macrophages to mediate the inflammatory response.

Confocal experiments show that sections in the *Clcn3*$^{-/-}$ condition were more reactive to GFAP staining than the control, indicating an increased expression of GFAP-associated glial cells in the absence of ClC-3. Dorsal and the ventral horns, more specifically the gray matter of the spinal cord (which has a butterfly-like red shape in Figure 3.14A) show glial proliferation

in the *Clcn3*$^{-/-}$ as observed by the increase in the abundance of an astrocytic-like cell when compared to the wild type conditions. Additionally, in the lower panel it can be observed that the expression of CD11b is increased in the whole tissue, and especially abundant in the dorsal horn of the spinal cord (showed as dashed line oval-shaped). Analysis of the dorsal horn of the spinal cord containing the layers I, II, III, and IV reveals a significant increase of about 89.39% in glia expressing GFAP (green color) and of about 49.09% in the area reactive to CD11b (red color) in *Clcn3*$^{-/-}$ when compared to the wild type, (Figure 3.14B and Table 3.7). This region houses most of the interneurons that modulate the nociceptive signal, and which receives inputs from the DRG neurons.

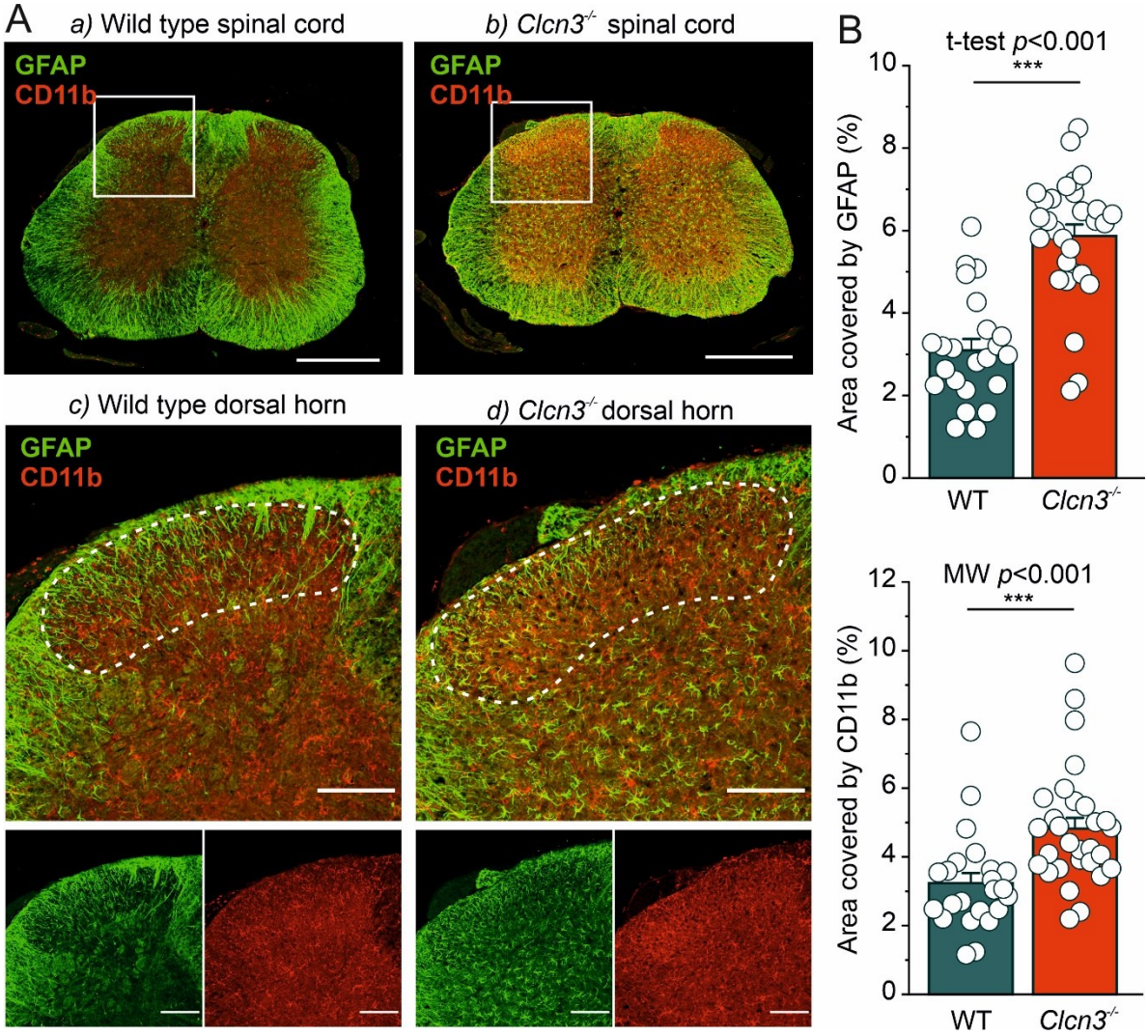

Figure 3.14. Quantification of astroglia and microglia in the DHSC in adult mice. **A**. Representative section of the thicker segment of the spinal cord from wildtype and *Clcn3*$^{-/-}$ mice show increased glia proliferation and microglia activation in the gray matter of mutant mice (upper panel). Scale bar from spinal cord section 500 µm. Dorsal horn

was identified and delineated (dashed line) to analyze the layers, I to IV (lower panel). Scale bar from dorsal horn 200 µm. **B**. Area of glia expressing GFAP (green) and activated microglia (red) is significantly increased in the *Clcn3*$^{-/-}$ mice. At least 6 slices obtained from the lumbar section from the same animal were used. Sections from the same animal were obtained at least 100 µm apart. WT (n=23); *Clcn3*$^{-/-}$ (n=*29*). Significance levels are given as ***p<0.001. * *Clcn3*$^{-/-}$ differs from WT.

While in adult *Clcn3*$^{-/-}$ mice behavioral pain, electrophysiological characterization of DRG and immunohistochemical analyses of DHSC show a clear correlation between them, the electrical properties of DRG neurons extracted from P21 animals did not provide convincing evidence that could explain nociceptive pain at that developmental stage. Therefore, immunohistochemical analyses of DHSC were performed on P21 *Clcn3*$^{-/-}$ mice. Confocal pictures obtained from young *Clcn3*$^{-/-}$ sections show an increase not only in astroglia proliferation labeled with GFAP but also in reactive microglia labeled with CD11b. The proliferation can be observed when comparing the regular staining patterns characterized by elongated somata and less developed processes in the wild type, with the increased number of long branching, thicker processes extended in all directions from the bright fluorescent stained soma in the *Clcn3*$^{-/-}$. Reactive astroglia (green channel) and microglia (red channel) are highlighted in the insets of Figure 3.15.

The presence of activated microglia together with the increased pain sensitivity in young mutant animals suggests that the increase in the release of chemokines such as CCL2 provokes microglia activation that alters the nociception in *Clcn3*$^{-/-}$ at an early developmental stage. Activated microglia triggers a cascade of the release of pro- and anti-inflammatory mediators necessary for healing under neuropathic and inflammatory pain (Mika et al., 2013; Vallejo et al., 2010). Astroglia and microglia proliferation is a clear indicator of a pathological pain condition in which these cells are involved in the modulation of neuronal sensitization and thus resulting in the prolongation of a pain state as is observed in the *Clcn3*$^{-/-}$ animals.

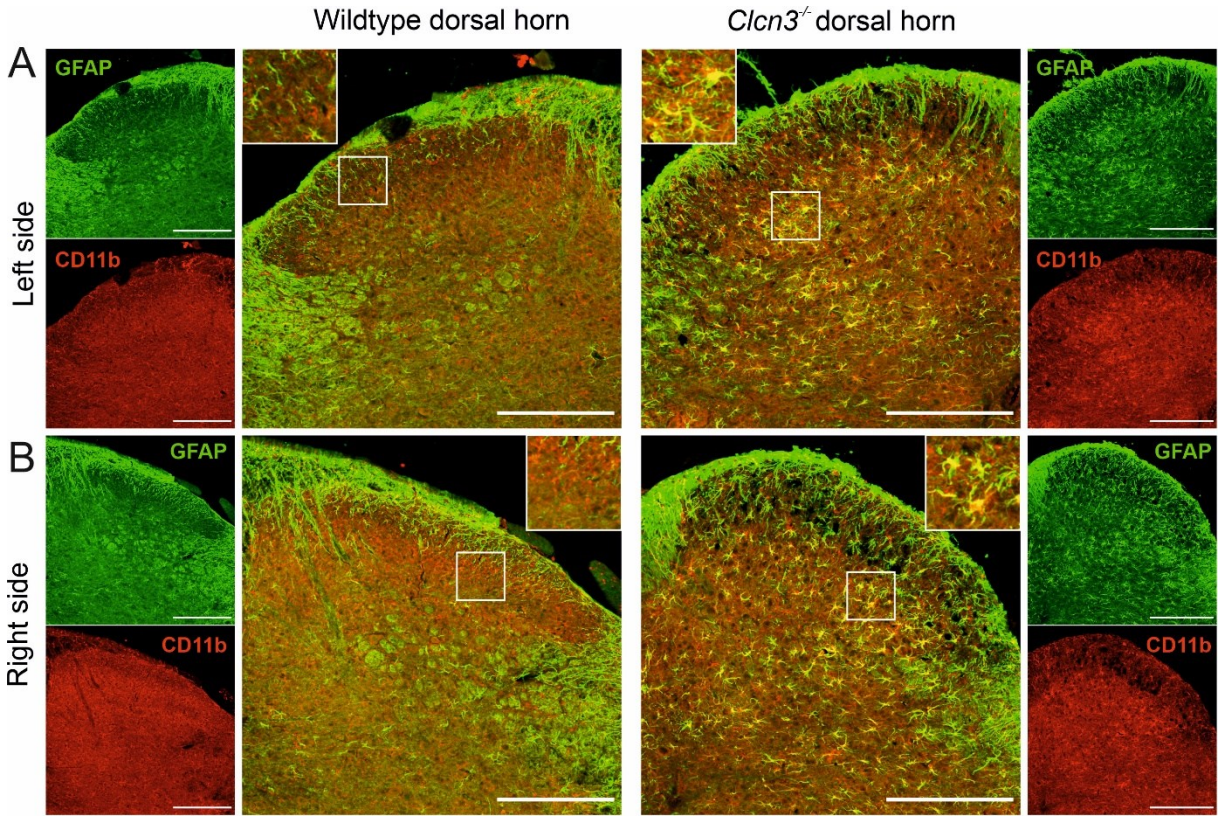

Figure 3.15. Representative confocal pictures of astroglia and microglia proliferation in the DHSC in young mice. Left dorsal horn section (A) and right dorsal horn section (**B**) from wildtype and *Clcn3*$^{-/-}$ mice show proliferation of astroglia (GFAP in green) and microglia (CD11b in red) in the gray and white matter. Scale bar 200 µm. At least 6 slices obtained from the lumbar section from the same animal were used. Sections from the same animal were obtained at least 100 µm apart.

3.10 Compiled data

Table 3.1. Behavioral test for acute thermal pain and chemical stimulation in young mice.

Condition	Genotype	Mean±SEM	N° animals	Normality test (Shapiro W.)	Variances (Levene)	Test used	P-value	Signif.
Hot plate test (latency)								
46 °C	WT	20.82±4.39 s	7	Failed	Passed	*T-test	p=0.909	n.s.
	Clcn3$^{-/-}$	19.41±11.25 s	8					
48 °C	WT	22.34±4.97 s	7	Failed	Passed	*T-test	p=0.152	n.s.
	Clcn3$^{-/-}$	13.46±2.83 s	8					
50 °C	WT	20.62±3.13 s	7	Failed	Passed	*T-test	p=0.03	*
	Clcn3$^{-/-}$	11.19±2.19 s	8					
52 °C	WT	16.20±1.52 s	7	Passed	Passed	T-test	p<0.001	***
	Clcn3$^{-/-}$	5.90±1.18 s	8					
Tail-flick test (latency)								
46 °C	WT	11.90±2.16 s	8	Failed	Passed	*T-test	p=0.003	**
	Clcn3$^{-/-}$	3.17±1.29 s	9					
48 °C	WT	4.67±1.60 s	8	Failed	Passed	*T-test	p=0.069	n.s.
	Clcn3$^{-/-}$	1.66±0.29 s	9					
50 °C	WT	1.38±0.20 s	7	Failed	Passed	*T-test	p=0.03	*
	Clcn3$^{-/-}$	0.90±0.09 s	9					

*Welch's unequal variances t-test; n.s. not significant.

Formalin test (licking/flinches)								
1 minute	WT	34.38±4.88	8	Passed	Passed	T-test	p=0.018	*
	Clcn3$^{-/-}$	48.89±2.79	9					
5 minutes	WT	3.88±1.84	8	Passed	Passed	T-test	p=0.017	*
	Clcn3$^{-/-}$	12.22±2.45	9					
10 minutes	WT	1.00±0.46	8	Failed	Passed	*T-test	p=0.001	**
	Clcn3$^{-/-}$	6.44±1.16	9					

Table 3.2. Behavioral test for acute thermal pain and chemical stimulation in adult mice.

Condition	Genotype	Mean±SEM	N° animals	Normality test (Shapiro W.)	Variances (Levene)	Test used	P-value	Signif.
Hot plate test (latency)								
46 °C	WT	13.79±2.33 s	11	Passed	Passed	T-test	p=0.129	n.s.
	Clcn3$^{-/-}$	9.11±1.90 s	13					
48 °C	WT	11.42±2.11 s	11	Failed	Passed	Mann-Whitney	p=0.006	**
	Clcn3$^{-/-}$	5.44±1.25 s	13					
50 °C	WT	15.71±2.11 s	11	Passed	Failed	*T-test	p<0.001	***
	Clcn3$^{-/-}$	5.52±1.17 s	13					
52 °C	WT	7.44±0.62 s	11	Passed	Passed	T-test	p=0.009	**
	Clcn3$^{-/-}$	3.95±0.99 s	13					
Tail-flick test (latency)								
46 °C	WT	19.38±2.46 s	8	Passed	Failed	*T-test	p=0.002	**
	Clcn3$^{-/-}$	7.79±0.83 s	9					
48 °C	WT	9.09±0.66 s	8	Passed	Passed	T-test	p<0.001	***
	Clcn3$^{-/-}$	4.55±0.41 s	9					
50 °C	WT	4.16±0.13 s	8	Passed	Passed	T-test	p<0.001	***
	Clcn3$^{-/-}$	2.13±0.19 s	9					

Formalin test (licking/flinches)								
1 minute	WT	45.00±4.34	6	Passed	Passed	T-test	p=0.058	n.s.
	Clcn3$^{-/-}$	30.25±5.16	8					
5 minutes	WT	15.50±3.33	6	Passed	Failed	*T-test	p=0.03	*
	Clcn3$^{-/-}$	31.75±5.62	8					
10 minutes	WT	9.83±1.96	6	Passed	Failed	*T-test	p=0.016	*
	Clcn3$^{-/-}$	31.88±7.01	8					
15 minutes	WT	20.83±4.50	6	Passed	Failed	*T-test	p=0.06	n.s.
	Clcn3$^{-/-}$	41.12±8.55	8					
20 minutes	WT	24.67±4.39	6	Passed	Passed	T-test	p=0.01	*
	Clcn3$^{-/-}$	51.25±6.76	8					
25 minutes	WT	16.50±3.89	6	Passed	Failed	*T-test	p=0.05	n.s.
	Clcn3$^{-/-}$	35.50±7.77	8					
30 minutes	WT	12.17±3.74	6	Passed	Failed	*T-test	p=0.06	n.s.
	Clcn3$^{-/-}$	33.75±9.34	8					

*Welch's unequal variances t-test; n.s. not significant.

Table 3.3. Statistical analysis of AP parameters from young DRG neurons mice.

AP properties	Genotype	Mean±SEM	N° cells/ cultures	Normality test (Shapiro W.)	Variances (Levene)	Test used	P-value	Signif.
Voltage threshold	Wild type	-33.52±0.95 mV	19 / 4	Passed	Passed	T-test	0.159	n.s.
	Clcn3$^{-/-}$	-30.76±1.28 mV	38 / 4					
AP amplitude	Wild type	89.25±1.49 mV	19 / 4	Passed	Passed	T-test	0.406	n.s.
	Clcn3$^{-/-}$	91.07±1.34 mV	38 / 4					
Half-width	Wild type	3.08±0.30 ms	19 / 4	Passed	Passed	T-test	0.002	**
	Clcn3$^{-/-}$	4.55±0.28 ms	38 / 4					
AHP amplitude	Wild type	23.98±1.23 mV	19 / 4	Passed	Passed	T-test	0.017	*
	Clcn3$^{-/-}$	27.89±0.94 mV	38 / 4					
Current threshold	Wild type	21.16±4.91 pA	19 / 4	Passed	Passed	T-test	0.876	n.s.
	Clcn3$^{-/-}$	24.97±2.99 pA	38 / 4					
Time to peak event	Wild type	57.73±17.59 ms	19 / 4	Failed	Failed	Mann-Whitney	0.044	*
	Clcn3$^{-/-}$	228.51±53.74 ms	38 / 4					
Resting potential	Wild type	-69.42±0.30 mV	19 / 4	Failed	Failed	Mann-Whitney	0.605	n.s.
	Clcn3$^{-/-}$	-68.79±0.35 mV	38 / 4					
Input resistance	Wild type	743.36±50.18 MΩ	19 / 4	Failed	Failed	Mann-Whitney	0.007	**
	Clcn3$^{-/-}$	1017.25±79.59 MΩ	38 / 4					

n.s. not significant.

Table 3.4. Statistical analysis of AP parameters from adult DRG neurons mice.

AP properties	Genotype	Mean±SEM	N° cells/ cultures	Normality test (Shapiro W.)	Variances (Levene)	Test used	P-value	Sig-nif.
Voltage threshold	Wild type	-34.76±1.13 mV	21 / 7	Passed	Passed	T-test	0.023	*
	Clcn3$^{-/-}$	-31.58±0.80 mV	36 / 6					
AP amplitude	Wild type	90.02±2.12 mV	21 / 7	Passed	Passed	T-test	0.051	n.s.
	Clcn3$^{-/-}$	86.74±1.56 mV	36 / 6					
Half-width	Wild type	3.69±0.37 ms	21 / 7	Passed	Passed	T-test	0.914	n.s.
	Clcn3$^{-/-}$	3.73±0.20 ms	36 / 6					
AHP amplitude	Wild type	25.26±1.09 mV	21 / 7	Passed	Passed	T-test	0.189	n.s.
	Clcn3$^{-/-}$	27.00±0.78 mV	36 / 6					
Current threshold	Wild type	39.62±6.13 pA	21 / 7	Passed	Failed	*T-test	0.0016	**
	Clcn3$^{-/-}$	17.67±2.86 pA	36 / 6					
Time to peak	Wild type	23.23±2.66 ms	21 / 7	Failed	Failed	Mann-Whitney	<0.001	***
	Clcn3$^{-/-}$	184.52±40.97 ms	36 / 6					
Resting potential	Wild type	-68.27±0.80 mV	21 / 7	Passed	Passed	T-test	0.504	n.s.
	Clcn3$^{-/-}$	-67.71±0.44 mV	35 / 6					
Input resistance	Wild type	746.15±67.41 MΩ	21 / 7	Failed	Failed	Mann-Whitney	<0.001	***
	Clcn3$^{-/-}$	1144.85±81.95 MΩ	34 / 6					

*Welch's unequal variances t-test; n.s. not significant.

Table 3.5. Sodium currents values from small-diameter DRG neurons from adult mice.

	Genotype	Mean±SEM (pA/fF)	N° cells/ animals	Normality test (Shapiro W.)	Variances (Levene)	Test used	P-value	Signif.
Macros. Na^+ current Max. peak (-20 mV)	Wild type	-245.3±29.0	24/5	Passed	Passed	t-test	$p<0.05$	*
	Clcn3$^{-/-}$	-313.9±28.0	24/8					
TTX-R Max. peak (-10 mV)	Wild type	-76.6±8.2	24/5	Failed	Passed	Mann-Whitney	<0.001	***
	Clcn3$^{-/-}$	-43.0±6.6	24/8					
TTX-S Max. peak (-20 mV)	Wild type	-210.3±28.0	21/5	Passed	Passed	t-test	$p=0.154$	n.s.
	Clcn3$^{-/-}$	-263.6±23.7	21/8					
Total Na^+ current Half-max act	Wild type	-27.9±2.2	24/5	Failed	Passed	Mann-Whitney	$p=0.244$	n.s.
	Clcn3$^{-/-}$	-32.4±1.7	24/8					
TTX-R Half-max act	Wild type	-19.9±1.2	24/5	Passed	Passed	t-test	$p=0.019$	*
	Clcn3$^{-/-}$	-24.6±1.6	24/8					
TTX-S Half-max act	Wild type	-33.2±1.7	21/5	Passed	Passed	t-test	$p=0.807$	n.s.
	Clcn3$^{-/-}$	-33.8±1.9	21/8					
TTX-R Half-max inact.	Wild type	-43.5±1.9	18/5	Failed	Passed	Mann-Whitney	$p=0.017$	*
	Clcn3$^{-/-}$	-47.8±1.9	22/8					
TTX-S Half-max inact.	Wild type	-84.3±1.3	17/5	Passed	Passed	t-test	$p=0.693$	n.s.
	Clcn3$^{-/-}$	-85.3±1.9	24/8					

Table 3.6. Potassium currents values from small-diameter DRG neurons from adult mice.

	Genotype	Mean±SEM (pA/pF)	N° cells/ cultures	Normality test (Shapiro W.)	Variances (Levene)	Test used	P-value	Signif.
Macros. K^+ current Max. peak 60 mV	Wild type	746.5±54.7	16/5	Passed	Passed	t-test	$p=0.002$	**
	Clcn3$^{-/-}$	1058.0±72.4	20/3					
4AP-R	Wild type	381.1±36.8	14/5	Passed	Failed	*T-test	$P<0.001$	***

Max. peak 60 mV	*Clcn3*$^{-/-}$	684.5±64.2	18/3					
4AP-S Max. peak 60 mV	Wild type	343.6±39.3	14/5	Passed	Passed	t-test	p>0.05	n.s.
	Clcn3$^{-/-}$	396.9±43.1	18/3					
KIR current max. peak (-160 mV)	Wild type	-26.5±8.1	15/3	Passed	Passed	t-test	p>0.05	n.s.
	Clcn3$^{-/-}$	-29.8±9.6	24/4					

*Welch's unequal variances t-test; n.s. not significant.

Table 3.7. Immunohistochemical analysis of neuronal viability in the DRG and DHSC.

	Genotype	Mean±SEM	N° cells/ cultures	Normality test (Shapiro W.)	Variances (Levene)	Test used	P-value	Sig-nif.
Dorsal root ganglia								
Neuronal population NeuN	Wild type	188.63±18.38	19	Passed	Passed	t-test	p=0.226	n.s.
	Clcn3$^{-/-}$	214.59±11.59	22					
Neuronal population IB4+ (%)	Wild type	32.46±2.57%	19	Passed	Passed	t-test	p=0.34	n.s.
	Clcn3$^{-/-}$	29.31±2.07%	22					
Neuronal population CGRP+ (%)	Wild type	10.76±1.50%	19	Passed	Failed	Mann-Whitney	p=0.16	n.s.
	Clcn3$^{-/-}$	16.54±2.62%	22					
Neuronal population IB4-; CGRP- (%)	Wild type	56.79±3.73%	19	Passed	Passed	t-test	p=0.617	n.s.
	Clcn3$^{-/-}$	54.16±3.62%	22					

n.s. not significant.

Dorsal horn of the spinal cord								
Neuronal population NeuN	Wild type	270.59±9.70	29	Failed	Passed	*T-test	p=0.18	n.s.
	Clcn3$^{-/-}$	255.70±5.46	33					
CCL2 expression IR area %	Wild type	0.005±0.002	28	Failed	Failed	Mann-Whitney	p<0.001	***
	Clcn3$^{-/-}$	0.034±0.008	33					
CCL2 expression Mean Fluoresc. int. (a.u.)	Wild type	0.089±0.003	28	Passed	Failed	Mann-Whitney	p<0.001	***
	Clcn3$^{-/-}$	0.114±0.004	33					
GFAP expression Area %	Wild type	0.031±0.003	23	Failed	Passed	*T-test	p<0.001	***
	Clcn3$^{-/-}$	0.059±0.003	29					
CD11b expression Area %	Wild type	0.032±0.003	23	Failed	Passed	*T-test	p<0.001	***
	Clcn3$^{-/-}$	0.048±0.003	29					

*Welch's unequal variances t-test; n.s. not significant.

Table 3.8. Statistical analysis of the AP parameters from adult DRG neurons from *Clcn3*^{E281Q}, *Clcn4*$^{-/-}$ and double mutant *Clcn3*^{E281Q}/*Clcn4*$^{-/-}$ mice.

AP properties	Genotype	Mean	N° cells/ cultures	Normality test (Shapiro W.)	Variances (Levene)	Test used	P-value	Signif.
Voltage threshold	*Clcn3*^{E281Q}	-32.76±0.97 mV	31 / 3	Failed	Passed	K-W Anova	χ^2>0.05	n.s.
	Clcn4$^{-/-}$	-32.24±0.71 mV	25 / 3					
	Clcn3^{E281Q}/*Clcn4*$^{-/-}$	-34.44±0.51 mV	49 / 7					
AP amplitude	*Clcn3*^{E281Q}	89.46±1.60 mV	31 / 3	Failed	Passed	K-W Anova	χ^2>0.05	n.s.
	Clcn4$^{-/-}$	90.23±1.05 mV	25 / 3					
	Clcn3^{E281Q}/*Clcn4*$^{-/-}$	93.49±0.75 mV	49 / 7					
AHP amplitude	*Clcn3*^{E281Q}	24.79±1.12 mV	30 / 3	Failed	Passed	K-W Anova	χ^2>0.05	n.s.
	Clcn4$^{-/-}$	26.05±1.17 mV	25 / 3					
	Clcn3^{E281Q}/*Clcn4*$^{-/-}$	26.27±0.62 mV	49 / 7					

Current threshold	*Clcn3*^{E281Q}	27.29±2.66 pA	31 / 3	Passed	Failed	K-W Anova	χ^2>0.05	n.s.
	Clcn4$^{-/-}$	32.08±5.63 pA	25 / 3					
	Clcn3^{E281Q}/*Clcn4*$^{-/-}$	29.71±2.85 pA	49 / 7					
Time to peak	*Clcn3*^{E281Q}	72.80±34.86 ms	31 / 3	Failed	Passed	K-W Anova	χ^2=0.09	n.s.
	Clcn4$^{-/-}$	47.61±17.13 ms	25 / 3					
	Clcn3^{E281Q}/*Clcn4*$^{-/-}$	37.32±5.58 ms	49 / 7					
Resting potential	*Clcn3*^{E281Q}	-69.35±0.19 mV	31 / 3	Failed	Failed	K-W Anova	χ^2>0.05	n.s.
	Clcn4$^{-/-}$	-69.38±0.24 mV	25 / 3					
	Clcn3^{E281Q}/*Clcn4*$^{-/-}$	-69.04±0.27 mV	49 / 7					
Input resistance	*Clcn3*^{E281Q}	703.78±30.88 MΩ	31 / 3	Failed	Passed	K-W Anova	χ^2>0.05	n.s.
	Clcn4$^{-/-}$	735.98±52.04 MΩ	25 / 3					
	Clcn3^{E281Q}/*Clcn4*$^{-/-}$	821.52±36.41 MΩ	49 / 7					

Chapter 4. Discussion

4.1 Physiological importance of intracellular chloride proton exchangers in nociception

Recent studies have highlighted the importance of chloride/proton exchangers in the nervous system. While some of the members of this family display none or mild effects in knock-out murine models, genetic ablation of two isoforms ClC-7 and ClC-3, have a severe impact on neurotransmission. This work focused on the role of ClC-3. This intracellular exchanger is mainly localized to the membrane of lysosomes, endosomes, and vesicles in neurons and a variety of other cell types. ClC-3 has been proposed to control pH and [Cl^-] (Guzman et al., 2014; Guzman et al., 2015; Jentsch and Pusch, 2018). Moreover, genetic ablation is associated with, changes in neuronal excitability at the postsynaptic site (Wang et al., 2006) as well as to control in neurotransmitter release at the presynaptic site (Guzman et al., 2014; Riazanski et al., 2011). More recently, ClC-3 has been suggested to play a critical role in hyperalgesia, due to the altered behavioral response to pain in knock-out mice, possibly caused by a pathological pain sensation (Pang et al., 2016).

Hyperalgesia is a chronic condition, in which the subject perceives increased pain to a stimulus that normally provokes pain, as a result of a lesion in the skin or a perturbation of the nociceptive system with peripheral or central sensitization (IASP Task Force on Taxonomy, 1994). This work focuses on the importance of the chloride/proton exchanger 3 in the nociceptive pathway through the DRG neurons and spinal cord of *Clcn3*$^{-/-}$ mice. Behavioral pain tests, whole-cell patch-clamp recordings from dissociated DRG neurons, and immunohistochemical analysis revealed hyperalgesia, changes in the electrogenic properties of the DRG neurons, and advanced inflammatory response in the dorsal horn of the spinal cord in *Clcn3*$^{-/-}$ mice.

4.2 Acute pain tests show hyperalgesia in *Clcn3*$^{-/-}$ mouse

We examined pain perception in a *Clcn3*$^{-/-}$ mouse model using a hot plate, tail-flick, and formalin tests. Results from pain-related behavior to thermal pain at both ages showed no differences in temperatures below 48°C in the hot plate test and below 46°C in the tail-flick test. This threshold in temperatures indicates that the *Clcn3*$^{-/-}$ animals do not display allodynia or

pain induced by an innocuous stimulus (Figure 3.1 and 3.2). Noxious heating of the skin evokes the activation of A-type and C-type thermoreceptors with a high threshold temperature. Heat temperature thresholds are regulated by heat-sensitive transient receptor potential ion channels of the vanilloid subtype (TRPV1 and TRPV3), which activate at around 43-44°C (Marics et al., 2014; Yeomans and Proudfit, 1996). Both thermal tests were useful to demonstrate hyperalgesia in *Clcn3*$^{-/-}$ mice, but the tail-flick test was more accurate and showed lower variability among the three phenotypes evaluated.

The clear reduction in the thermal threshold in *Clcn3*$^{-/-}$ mice differs from the previous results of another group, who found no significant differences in paw withdrawal latencies to heat, but only decreased paw withdrawal threshold to mechanical stimuli (Pang et al., 2016). The reason for this apparent discrepancy might be the different experimental strategies used to avoid the so-called "learning-effect" that is typically associated with such experiments (Suaudeau et al., 2005). Pang and colleagues used an automated hot plate device that measured the paw licking, rearing, and jumping automatically. The experiment was carried out in triplicate at intervals of 15 minutes. However, it has been reported that latencies of reactions may vary if mice are exposed multiple times in less than 24 hours (Suaudeau et al., 2005). In this work, in order to minimize the learning-effect, animals were placed for at least two hours in empty cages before they were exposed to the plate or water at room temperature. Once the animals were conditioned, they were exposed randomly to four different temperatures 46°C, 48°C, 50°C, and 52°C in both tests. Each temperature was measured once per day with at least one hour between measurements. These conditions permitted differentiation between the *Clcn3*$^{-/-}$ and the wild type at noxious temperatures (50°C and 52°C) in young and adult mice.

The Von-Frey test for mechanical sensitivity was initially used but without conclusive results, and withdrawal/licking latencies to cold allodynia were not evaluated. Instead, injection of 0.5% of formalin was used to assess inflammatory nociceptive pain. *Clcn3*$^{-/-}$ young mice showed an enhanced response in the early phase of this experiment at 1-, 5- and 10-minutes post-injection. This reaction involves the activation of C-type nociceptors and the release of mediators that promote peripheral sensitization such as ATP, glutamate, kinins (including bradykinin), histamine, serotonin, cytokines, and tropic factors (Amaya et al., 2013; Hunskaar and Hole, 1987). However, we did not observe a second phase reaction to an inflammatory process in wild type animals. Nevertheless, both phases were observed in adult mutant mice;

first, the early acute period (5- to 10-minutes long), followed by a decay phase (20- to 40-minutes). *Clcn3*$^{+/-}$ also displayed increased late response when compared to the wild type. This late phase is dominated by an inflammatory response in the tissue and functional changes in the dorsal horn of the spinal cord, providing more valid data for clinical pain than monophasic mechanical or thermal stimuli (Hunskaar and Hole, 1987; Tjølsen et al., 1992). The increase in the activity during the second phase suggests a progression in the central sensitization within the dorsal horn, that changes the elicited sensory response and releases pro-inflammatory mediators to the spinal cord (Mika et al., 2013; Ren and Dubner, 2008; Vallejo et al., 2010).

4.3 ClC-3 modulates the electrical properties of sensory neurons

Pain sensation is based on the conversion of external noxious stimuli into internal electrical inputs by nociceptors that are then processed by the CNS. Several mechanisms are activated to avoid further damage, permitting an involuntary behavior of pain avoidance (Emery and Ernfors, 2020; IASP Task Force on Taxonomy, 1994). The electrical properties of the nociceptors are changed in *Clcn3*$^{-/-}$, particularly in adult animals. The average frequencies of action potentials in DRG neurons are significantly increased in *Clcn3*$^{-/-}$ adult mice, but not in young ones. The increase in AP numbers might be due to a higher input resistance (R_{in}), a lower current threshold, or a higher voltage threshold (Figure 3.4). Pang et al. (2016) found differences in the properties of action potentials of small-diameter DRG neurons from *Clcn3*$^{-/-}$ mice; they reported a prominent change of around ~10 mV towards more hyperpolarized potentials in the voltage threshold. In contrast, we observed a shift of 3 mV towards more positive potentials in mutant neurons.

The AP threshold reflects changes in the properties of the voltage-gated sodium channels (VGSC) (Hu et al., 2009), especially of isoforms responsible for setting the membrane potential subthreshold such as $Na_v1.6$, $Na_v1.7$, and $Na_v1.9$. Uninjured neurons likely increase the AP threshold as a feedback regulatory mechanism upon noxious stimulus. A similar effect is observed in nociceptive DRG neurons: upon electrical stimulation and perfusion of capsaicin, the threshold for generating second AP is increased due to inhibition of the VGSC (Liu et al., 2001).

Pang et al. (2016) found more pronounced differences in the rheobase between wild type and mutant cells (WT 365±37 pA vs *Clcn3*$^{-/-}$ 171±28 pA) than observed in this work (WT 39.62±6.13 pA vs *Clcn3*$^{-/-}$ 17.67±2.86 pA). This discrepancy is most likely caused by the

protocol for the action potential generation used in both experiments. A shorter current injection (about 15 ms in their work) evokes action potentials at higher stimulus input, while a longer stimulus duration (1 s in this work) evokes AP with a lower stimulus input; the chronaxie represents the relationship between the stimulus duration and the rheobase (Brocker and Grill, 2013). A decreased rheobase is also observed in the mouse model of chronic constriction of the DRGs (Fan et al., 2011).

Parameters such as voltage threshold, resting membrane potential (RMP), and R_{in}, from both research, suggest increased excitability of small-diameter DRG neurons in the absence of ClC-3, as observed in the lower excitability index (EI) calculated for *Clcn3*$^{-/-}$ neurons. A higher R_{in} is also associated with late-spiking (LS) neurons in other regions of the brain. It has been observed that LS neurons display a slowly-developing inward potassium current at subthreshold potentials that might delay the AP initiation (McGann et al., 2001). Despite that inward-rectifier potassium currents were not different in the *Clcn3*$^{-/-}$ neurons, an increase in the slowly inactivating potassium conductance at more positive potentials might delay the onset of the APs. The obtained data lie within the range of AP parameters published and compiled in the database NeuroElectro Project, for murine dorsal root ganglia (Tripathy and Gerkin, 2013). These findings support the hypothesis that alterations of VGSC, voltage-dependent K^+ channels, and others, like hyperpolarization-activated cyclic nucleotide-gated channels, may underlie the increased DRG neuronal excitability in the absence of ClC-3 (Liu et al., 2001; Pang et al., 2016; Stemkowski and Smith, 2012).

4.4 ClC-3 regulates the density of voltage-gated channels in the plasma membrane of murine DRG neurons

4.4.1 Voltage-gated sodium channels densities are altered in *Clcn3*$^{-/-}$ neurons

Sensory neurons become hyperexcitable in peripheral inflammatory conditions or neuropathic pain caused by genetic diseases or nerve injury; and electrophysiological examination of DRG neurons suggested changes in the expression or the biophysical properties of Na^+ currents (Meents et al., 2019; Stemkowski and Smith, 2012). In agreement with this notion, dissociated DRG neurons from *Clcn3*$^{-/-}$ exhibited slightly increased total Na^+ peak current (WT -245.28±29.0 pA/pF vs *Clcn3*$^{-/-}$ -313.86±28.0 pA/pF, Figure 3.8C), a robust and significant reduction in the TTX-resistant current mediated by $Na_v1.8$ and $Na_v1.9$ (WT -76.56±8.1 pA/pF vs *Clcn3*$^{-/-}$ -43.02±6.6 pA/pF, Figure 3.8C) with no apparent changes in

the TTX-sensitive $Na_v1.7$ (WT -210.3±28.0 pA/pF vs *Clcn3*$^{-/-}$ -263.5±23.7 pA/pF, Figure 3.8E). Misregulation of $Na_v1.7$ and/or $Na_v1.8$ in DRG neurons has been reported both in humans with neuropathic pain (Li et al., 2018) and models of induced neuropathies (Bernal, 2018; Fan et al., 2011; Li et al., 2018). As a consequence of an axotomy of peripheral nerves (Sleeper et al., 2000), as well as in rats with bone cancer pain (Miao et al., 2010), the expression levels of functional TTX-resistant sodium channels are significantly reduced. Peripheral axotomy also alters the electrophysiological properties of neurons in the petrosal ganglion (Gallego et al., 1987). Besides, total protein levels of the sodium channel $Na_v1.8$ do not differ from the wild-type condition, excluding the possibility that the disruption of ClC-3 interferes with the *de novo* synthesis of the TTX-resistant sodium channels. Altogether, these observations are compatible with a function of ClC-3 in regulating the trafficking pathway of VGSC, more specifically the TTX-resistant sodium channels $Na_v1.8$/$Na_v1.9$, or their auxiliary β-subunits. It has been found that β-1 subunit increases the current densities of $Na_v1.8$ and shifts its activation to more negative potentials, while β-3 subunit decreases its current densities, but leaving the gating properties unaffected (Zhao et al., 2011). Similar to other membrane proteins, VGSCs are translated in the rough ER and transported to the plasma membrane via vesicles (Swanwick et al., 2010). Clathrin, clathrin-associated protein-1A (CAP-1A), annexin 2 light chain p11, and β-subunit 3 are accessory subunits associated with the trafficking of $Na_v1.8$ to the plasma membrane (Liu et al., 2005; Okuse et al., 2002; Swanwick et al., 2010). Thus, a direct effect of ClC-3 in the trafficking pathway of one of these proteins may account for the observed effect in *Clcn3*$^{-/-}$ cells.

Clcn3$^{-/-}$ results resemble the peripheral axotomy model, where an increase in TTX-sensitive and a decrease in TTX-resistant currents are observed (Cummins and Waxman, 1997; Sleeper et al., 2000). Changes in the sodium current densities provide the basis for the altered electrical properties observed in *Clcn3*$^{-/-}$ and peripheral nerve injury models. It has been proposed that $Na_v1.8$ channels produce the majority of the inward current during the action potential upstroke in the nociceptive DRG neuron (Blair and Bean, 2002) and that $Na_v1.9$-mediated current might contribute to the resting potential and to setting the sub-threshold of the AP generation (Herzog et al., 2001; Meents et al., 2019). Furthermore, TTX-S currents are thought to contribute only to the initial response, setting the AP threshold and the rheobase in sensory neurons (Cummins and Waxman, 1997).

We did not observe changes in the voltage-dependence of the total sodium current nor of the TTX-S sodium current. In contrast, the TTX-R mediated channels from *Clcn3*$^{-/-}$ neurons showed a slight leftward shift in the voltage-dependence of activation. Slightly changed TTX-R inactivation curves were also observed in *Clcn3*$^{-/-}$ when compared to the control condition, producing a small shift of 4.3 mV on the half-maximal for the steady-state channel inactivation to more hyperpolarized potentials (WT, -43.5±1.0 mV vs *Clcn3*$^{-/-}$ -47.3±1.4 mV, Figure 3.9). TTX-resistant $Na_v1.8$ or $Na_v1.9$ sodium channels have distinctive characteristics, $Na_v1.9$ activates at more negative potentials than any other VGSC (-58 mV in rat DRG neuron), and the currents generated inactivate on a very slow time course (>100 ms) (Padilla et al., 2007). Therefore, an unbalance in membrane expression between those two sodium channels might contribute to the enhanced excitability of the neurons and the observed increased pain reaction in the *Clcn3*$^{-/-}$ mice. Changes in sodium channel expression were observed in rats under chronic constriction injury. These animals showed a decrease in the $Na_v1.8$ current densities in injured DRG neurons and a shift in the voltage-dependence of activation by 5.3 mV to depolarized potentials, while the steady-state inactivation was shifted by 10 mV to hyperpolarized potentials (Li et al., 2015).

The changes observed in the sodium current densities from the small-diameter DRG neurons from *Clcn3*$^{-/-}$ mice might be caused by inflammatory mediators, including NFG, prostaglandin E2, adenosine, and serotonin (Fan et al., 2011; Wood, 2008). For example, prostaglandin E2 and serotonin decrease the current threshold for excitation of nociceptors (Cardenas et al., 2001). The release of such mediators is dysregulated in animal models of neuropathic or inflammatory pain (Fang et al., 2002), and it is likely that *Clcn3*$^{-/-}$ mice also present a dysregulation in the release of pro-inflammatory mediators within the dorsal root due to the absence of ClC-3, that leads to an alteration of the VGSC expression (Liu et al., 2010a). Taken together, these results contribute to the understanding of the enhanced excitability observed in the *Clcn3*$^{-/-}$ mice, where a significant change in the TTX-R current densities might change the electrical properties of the AP observed in the DRG neurons.

4.4.2 DRG neurons exhibit larger potassium currents in *Clcn3*$^{-/-}$ mice

The electrical properties of the neurons are also determined by voltage-gated potassium channels (K_v). Upon depolarization, sodium channel activation mediates the rising phase of the action potential. When the cell reaches K_v channel threshold potential (between +30 to +50 mV),

K_v activation drives potassium ions out of the cell and mediates the decay phase of the AP (Busserolles et al., 2020). This work shows evidence for a ClC-3 dependent regulation of K_v membrane expression. *Clcn3*$^{-/-}$ small-diameter DRG neurons exhibited an increase in the total K_v potassium peak current (Figure 3.11), a phenotype that was essentially caused by the slow inactivating potassium currents. Different expression levels of voltage-gated K^+ currents have been associated with various animal models of chronic pain. For example, an increase in the total K^+ currents (I_K and I_A) in small-sized DRG neurons has been observed in a rat model of inflammatory pain after *in vivo* application of zymosan, an inflammatory agent typically used to induce neuropathic pain (Wang et al., 2007). Moreover, DRG neurons from a bone cancer pain rat model have also shown an upregulation of K_v1.4 and K_v4.3 channels and an increase in the amplitudes and densities of A-type K^+ currents (Duan et al., 2012). These observations resemble those from the *Clcn3*$^{-/-}$ animal model, in which the I_{Total} and the slowly inactivating K^+ currents were significantly increased.

Alterations of neuronal potassium currents might contribute to changes in the action potential properties of the different nociceptors. Under normal conditions, it has been documented that IB4-positive neurons display larger K_v currents, a longer onset of action potentials, and a reduced rheobase upon application of 4-AP than the IB4-negative ones (Vydyanathan et al., 2005). In this context, ClC-3 deletion might cause a selective loss of IB4-negative neurons in the dorsal root ganglia, leaving IB4-positive neurons unaffected, however, the percentage of this neuronal type in *Clcn3*$^{-/-}$ is not altered (Figure 3.12). Similar results were found for CGRP positive neurons in knock-out animals. Therefore, the observed changes in the AP properties are not caused by a selective loss of neurons in the dorsal root ganglia.

DRGs express a wide range of potassium channels, K_v1.2, 1.4, 2.2 3.4, 4.2, and 4.3, and many of them might be altered in hyperalgesia (Duan et al., 2012; Kim et al., 2002; Rasband et al., 2001). Additionally, different pain models show diverse changes in the potassium current densities hampering to point out a direct role of K_v in the regulation of the AP properties, however, a reduction in the rheobase was consistently observed. An increase in the AP threshold and the input resistance, as well as an increase in the repetitive firing, were present in most of the cases (Fan et al., 2011; Pang et al., 2016; Tan et al., 2006; Wang et al., 2007; Xu et al., 2006). These results are comparable with the changes in the AP properties from the DRGs evaluated in this work. Neurons from *Clcn3*$^{-/-}$ mice showed decreased rheobase, increased input resistance,

and increased firing frequencies, but an increase in the AP threshold was observed, most probably because this parameter is determined mostly by VGSC (Blair and Bean, 2002; Hu et al., 2009). It is not clear whether there is a unique and direct role of the different potassium channels in AP properties of sensory neurons and further research is needed.

4.5 Chloride transport activity of ClC-3 is not required for the regulation of cell excitability in DRG neurons

ClC-3 functions as a Cl^-/H^+ exchanger in intracellular organelles. ClC-3 was proposed to provide a chloride shunt in endosomes, to facilitate acidification by V-type ATPases (Jentsch and Pusch, 2018; Okamoto et al., 2008). It has been thought to play an important role in synaptic transmission in the CNS, but a recent discovery dismisses the presence of this transporter in synaptic vesicles (Taoufiq et al., 2020), suggesting that ClC-3 might regulate neuronal communication at a different level. Additionally, ClC-4 which does not have sorting signals, associates with ClC-3 to leave the endoplasmic reticulum (ER) and to be exported to different endosomes adding further complexity (Guzman et al., 2017). Here, evaluation of the electrical properties of the DRG neurons in a double mutant *Clcn3*^{E281Q}/*Clcn4*$^{-/-}$ mouse model revealed new insights into the role of ClC-3 in regulating neuronal excitability. Unexpectedly, the passive and the active properties of the small-diameter DRG neurons from double mutant *Clcn3*^{E281Q}/*Clcn4*$^{-/-}$ mouse are not different from the wild type. Similar results were found in control single mutants *Clcn3*^{E281Q} and *Clcn4*$^{-/-}$ DRG neurons. These results provide the first experimental evidence of a role of ClC-3 that is independent of the chloride/proton activity.

Clcn3^{E281Q} knock-in has no obvious phenotype unlike *Clcn3*$^{-/-}$, in this case, ClC-3E281Q can interact with other membrane proteins like ClC-4 which compensates for the loss of its transport activity. *Clcn4*$^{-/-}$ appears healthy but its absence in *Clcn3*^{E281Q}/*Clcn4*$^{-/-}$ mouse causes similar or even stronger neurodegeneration than that observed in the *Clcn3*$^{-/-}$. A similar mouse model to *Clcn3*^{E281Q}, carrying the E224A mutation in the "gating glutamate" that uncouples Cl^- currents from H^+ countertransport (*Clcn3*$^{unc/unc}$), allows the ClC protein to mediate channel-like Cl^- conductances without appreciable H^+ transport. *Clcn3*$^{unc/unc}$ knock-in mice did not show an evident phenotype, however, when ClC-4 is knocked-out in the *Clcn3*$^{unc/unc}$/*Clcn4*$^{-/-}$, animals display a neurodegenerative process in the hippocampus at the third postnatal week (Weinert et al., 2020). These two mice models, the *Clcn3*^{E281Q}/*Clcn4*$^{-/-}$ and *Clcn3*$^{unc/unc}$/*Clcn4*$^{-/-}$, illustrate

the importance of the Cl^-/H^+ transport activity for neuronal survival in the central nervous system.

It is still unclear how ClC-3E281Q alone can affect the current densities from sodium and potassium channels. ClC-3 is known to reside in intracellular compartments but can also be found transiently on the plasma membrane as part of its trafficking itinerary. ClC-3 possesses clathrin-binding motifs in its amino terminus (Stauber and Jentsch, 2010; Zhao et al., 2007), and neutralization of these motifs retain the protein into the plasma membrane. This suggests that similar that ClC-5, ClC-3 might be also involved in endocytosis. Endocytosis is impaired in *Clcn5*$^{-/-}$'s kidney proximal tubular cells by an unknown mechanism (Christensen et al., 2003). Most of the ion channels are sorted via the secretory pathway (Griffith, 2001; Swanwick et al., 2010), and ion channels have a variety of sorting signals and binding partners that target them to the plasma membrane, or keep them in the ER (assembled channels with improper subunit stoichiometry) (Griffith, 2001; Stockklausner and Klöcker, 2003). For example, it is known that clathrin, CAP-1A, p11, and β-subunit 3 are accessory subunits associated with the trafficking of $Na_v1.8$ to the plasma membrane (Liu et al., 2005; Okuse et al., 2002; Swanwick et al., 2010). ClC-3 might be present in the same clathrin-coated vesicle as other ion channels, facilitating endocytosis and guiding vesicles to lysosomes (ClC-3b) or recycling endosomes (ClC-3c) (Guzman et al., 2015). ClC-3 protein devoid of Cl^-/H^+ activity in *Clcn3*^{E281Q}/*Clcn4*$^{-/-}$ mice is fully capable to maintain interaction with its partner proteins. In this regard, the wild type phenotype observed in DRG neurons from double mutant *Clcn3*^{E281Q}/*Clcn4*$^{-/-}$ mice supports the view of a mechanism independent of the Cl^-/H^+ transport for ClC-3.

Figure 4.1 illustrates the endosomal compartments where ClC-3 has been found. ClC-3 is a chloride/proton exchanger that has been localized into recycling endosomes, lysosomes, and LDC (Deriy et al., 2009; Guzman et al., 2015; Li et al., 2009). Neurotransmitter-containing vesicles are fused with the plasma membrane in the regulated secretory pathway. After exocytosis, clathrin-coated vesicles are endocytosed and retrieved through the early endosome to the trans-Golgi network (Ceridono et al., 2011). Since voltage-gated ion channels are also sorted from the ER to the plasma membrane through vesicles, and impairment in this pathway might underly altered expression levels in the DRG neurons.

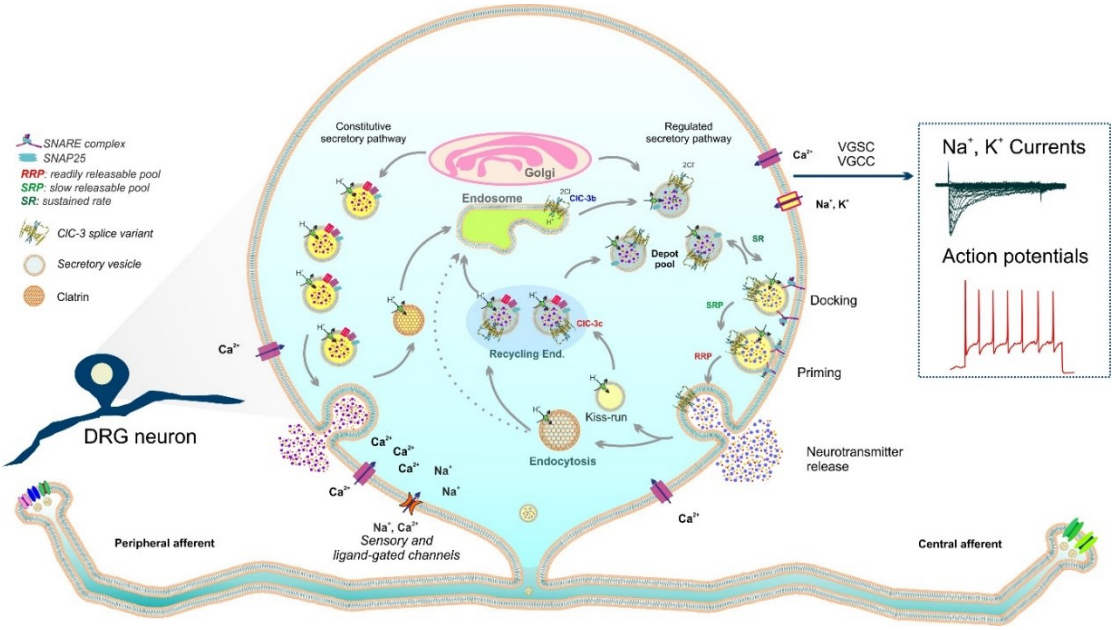

Figure 4.1. Estimated localization of ClC chloride/proton exchanger 3 in the regulated secretory pathway of the dorsal root ganglion neuron.

4.6 Ablation of ClC-3 does not affect neuronal viability in the dorsal root ganglion and dorsal horn of the spinal cord

ClC-3 deletion leads to massive neuronal loss in hippocampal and retinal tissue (Stobrawa et al., 2001). In contrast, immunohistochemical analysis of the dorsal root ganglia as well as of the dorsal horn of the spinal cord (DHSC) from *Clcn3*$^{-/-}$ mouse shows no changes in the number of neurons (Figure 3.12 and 3.13). A few studies on neuronal population in the DHSC have shown conflicting results about the origin of neuropathic pain. The first hypothesis describes the death of GABAergic neurons as the basis for loss of inhibition in the dorsal horn (Moore et al., 2002). This was proposed after measuring $GABA_A$ receptor-mediated IPSCs in CCI and SNI models and after observing apoptotic cell death in the superficial DHSC one-week after SNI. Meisner et al. (2010) also showed loss of GABAergic inhibitory interneurons in the superficial DHSC in *gad1*:GFP mice after spinal cord injury (SCI). In contrast, Polgár et al. (2004) did not find neuronal loss in the lamina I, II, and III in rats that exhibited thermal hyperalgesia in the CCI model. They suggest that a substantial neuronal death is not necessary for the development of thermal hyperalgesia and other mechanisms, such as alterations of anion gradients in the dorsal horn neurons would have an excitatory action in nociception. In line with this notion, the *Clcn3*$^{-/-}$ animal model does not show signs of neuronal loss in the DHSC

(Figure 3.13) suggesting that other mechanisms must be responsible for the observed hyperalgesia.

Central sensitization can also be caused by altered expression of the potassium-chloride transporter 2 (KCC2) or Na-K-Cl cotransporter (NKCC1), that modify the chloride equilibrium homeostasis and the GABAergic inhibitory synaptic transmission (Biber and Boddeke, 2014; Coull et al., 2005; Tan et al., 2020). Furthermore, upregulation of CCL2-CCR2 has been proposed to cause neuronal dysfunction through the phosphoinositide-3-kinase (PI3K)/Akt signaling pathway (Gosselin et al., 2005), and it has been demonstrated that CCL2 concentration-dependently increased TTX-resistant $Na_v1.8$ current densities in DRG neurons, accompanied by a shift in the activation and steady-state inactivation curves of $Na_v1.8$ (Belkouch et al., 2011). Interestingly, *Clcn3*$^{-/-}$ mice exhibit a significant increase in the expression of CCL2 within the neuronal processes in the DHSC. In contrast to the previous studies, the TTX-resistant Na_v currents were significantly reduced in this animal model, excluding the possibility that alteration of Na_v currents is CCl2 mediated but rather emphasizes the ClC-3-mediated trafficking of Na_v channels.

4.7 Functional changes in the DHSC and the role of glial cells in central sensitization in *Clcn3*$^{-/-}$ mice

Functional and morphological changes in glial cells in the peripheral tissue as well as in the CNS characterize some models of neuropathic and inflammatory pain. These changes are modulated by the release of neurotransmitters from neurons and inflammatory mediators such as glutamate, ATP, Substance P, CGRP, NFG, prostaglandin E2, adenosine, serotonin (Fan et al., 2011; Ferrari et al., 2014; Wood, 2008) and CC-chemokine ligand 2 (CCL2) (Wang et al., 2010; Xie et al., 2018; Zhu et al., 2014). Consequently, satellite glial cells proliferate resulting in central sensitization, the release of pro-inflammatory cytokines/interleukins, and migration of macrophages (Mika et al., 2013; Vallejo et al., 2010). Interestingly, *Clcn3*$^{-/-}$ adult mice show a significant increase in the expression levels of CCL2 in the DHSC (Figure 3.13). Higher expression of this mediator is usually accompanied by higher protein levels of its receptor in the DRG after chronic constriction injury (CCI), spinal nerve ligation (SNL), and chronic compression of the DRG (CCD) (Wang et al., 2010) and in the spinal cord (Komiya et al., 2020; Zhu et al., 2014), (Komiya et al., 2020; Zhu et al., 2014), promoting central sensitization and

inflammatory pain (Xie et al., 2018). Together this evidence suggests that upregulation of CCL2 in *Clcn3*$^{-/-}$ mouse might lead to hyperalgesia.

Immunohistochemical analysis of the DHSC reveals astroglia and microglia activation in the spinal cord from *Clcn3*$^{-/-}$ mice. Adult and young *Clcn3*$^{-/-}$ mice exhibit an increase in the number of reactive microglia and astroglia not only within the dorsal horn (layers I, II, III, and IV) (Figures 3.14 and 3.15) but also in the ventral horn, as shown by the scar-forming astrocytes and hypertrophy, which is the process extension that mediates neuroinflammation (Li et al., 2019b). To this point, it is difficult to assess whether changes in the electrical properties of the DRG neurons lead to changes in central sensitization, or the absence of ClC-3 in the spinal cord might play a feedback process in nociception. However, the identification of reactive microglia in young mice and the almost-normal electrical properties of the DRG neurons suggest an early effect in the central sensitization that might contribute to the enhanced nociception in the *Clcn3*$^{-/-}$ mice. Reactive microglia and astroglia might also explain the reduction in the density of pyramidal cells in the hippocampus previously described (Stobrawa et al., 2001; Yoshikawa et al., 2002). Activated neuroinflammatory microglia induce the activation of A1-type astrocytes by secreting Il-1α, TNF, and C1q. This type of astrocytes in turn releases neurotoxins that induce rapid death of neurons and oligodendrocytes, for a subset of neurons from the CNS, like pyramidal, cortical, and some motor neurons, but not for preganglionic and gamma motor neurons (Li et al., 2019b; Liddelow et al., 2017), therefore it is most likely that other regions in the ascending spinothalamic pathway, that modulated pain signaling might also be affected.

To summarize, these findings strongly support an important role of ClC-3 in nociception. The impact of ClC-3 deletion in hyperalgesia is demonstrated by the altered high-threshold thermal, inflammatory sensation and by the enhanced neuronal excitability due to the altered electrical properties of the DRG neurons as a consequence of changes in Na^+ and K^+ current densities. Finally, mutant animals show central sensitization because of the increased expression of CCL2, which induces the activation of astroglia and microglia in the spinal cord. Figure 4.2 summarizes these findings and points out other possible areas in the brain that might be affected in the ascending-descending somatosensory pathway, which will provide more information about the complete role of ClC-3 in pain sensation.

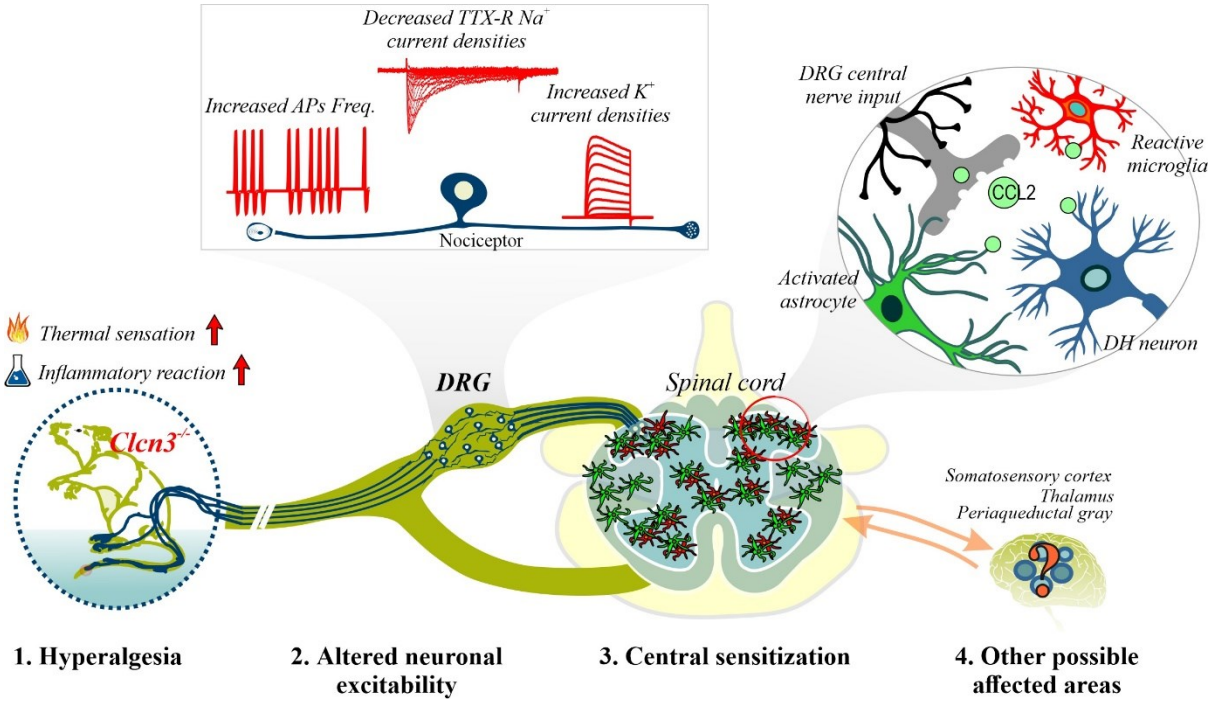

Figure 4.2. Changes in the pain signaling pathway in the *Clcn3*$^{-/-}$ mouse model. 1. Enhanced noxious stimuli in high-threshold thermal and inflammatory perception evidence hyperalgesia in adult mice. 2. Enhanced neuronal excitability due to changes in the ionic current densities and action potential generation. 3. Increased in the number of reactive microglia and activated astroglia indicates central sensitization in young and adult mice. 4. Possible affected parts of the ascending-descending somatosensory pathway.

Chapter 5. Conclusions

ClC-3 is an intracellular chloride/proton exchanger that is important for neuronal survival in the hippocampus and the retina (Stobrawa et al., 2001), and recent studies have linked several members of the intracellular ClC members to nociception (Pang et al., 2016; Poët et al., 2006; Polovitskaya et al., 2020). Although it has been postulated to play a role in synaptic transmission in the CNS (Guzman et al., 2014; Riazanski et al., 2011), a recent report suggests that the chloride/proton exchange rather than the chloride conductance is important for the physiological role of ClC-3 in the CNS (Weinert et al., 2020). The experiments reported in this thesis demonstrate that the genetic ablation of ClC-3 impairs high-thermal and inflammatory nociception. The data obtained from cultured nociceptive DRG neurons from adult mice reveal a developmental progression in neuronal excitability, observed in age-dependent alteration of action potential properties. Changes in DRG excitability are associated with decreased densities of $Na_v1.8$/ $Na_v1.9$ TTX-resistant channels and increased densities of voltage-gated potassium channels. Although my research focuses on the changes in AP and alterations in the voltage-gated K^+ and Na^+ channels, it should be noted that other ion channels may also play roles in sensory neurons from *Clcn3*$^{-/-}$, these might include the capsaicin receptor (Liu et al., 2001), hyperpolarization-activated cation channels (Djouhri et al., 2018), and voltage-gated calcium channels (Abdulla and Smith, 2001).

The data collected in this project revealed for the first time an additional function of ClC-3 that is independent of its chloride/proton activity. Here, I hypothesize that ClC-3 regulates the trafficking of voltage-gated K^+ and Na^+ channels by a protein-protein interaction mechanism. Additionally, ClC-3 might play a role in central sensitization and neuroprotection by regulating the release of neurotransmitters and mediators such as CCL2, responsible for the activation of astroglia and microglia. My work illustrates the impact of ClC-3 in nociception and highlights the importance of understanding the role of intracellular chloride/proton exchangers in the development of pain. ClC-3 might represent a novel target for analgesics with a promising therapeutic utility in neuropathic or inflammatory pain conditions.

6. Acknowledgments

I would like to acknowledge Dr. Professor Christoph Fahlke whom I am grateful for providing me this opportunity to pursue my Ph.D. in the Institute for Biological Information Processes 1 (IBI-1) in this very interesting topic. Here I found the support needed during all this time and the good working conditions in his labs.

I am very grateful to Dr. Raul E. Guzman for his invaluable support expertise and patience. To him and to Prof. Christoph Fahlke I owe all the acquired knowledge in this exciting field of neurosciences. Also, to Prof. Jesus Olivero Verbel for believing in me.

To my colleagues and friends Dr. Claudia Alleva, Dr. Yulia Kolobkova, Bettina Kolen, Andrei Kostritskii, Francisco Castilla, Kateryna Ryndia, Carène Benasolo, and the Ph.D. students with whom I shared most of the time and made the living abroad more bearable.

To all the researchers and staff from the IBI-1 that support and advise me every time I needed, Anita Eckert, Dr. Stefanie Bungert-Plümke, Dr. Patricia Hidalgo, Arne Franzen, and Nadine Jordan.

To the researchers from the Institute of Neuroscience and Medicine, Medical Imaging Physics (INM-4), Dr. Antje Willuweit, Carina Balduin, Michael Schöneck, and Verena Graf. And to Dr. Ute Becherer and Margarete Klose, from the CIPMM, Cellular Neurophysiology, Saarland University who showed me the DRG neuronal culture, and to Dr. Angelika Lampert from the Institute of Physiology, RWTH Aachen University who provided helpful discussion.

También a mis padres Juan Sierra e Iris Márquez, y mis hermanos, familiares y amigos del Cenfes que creyeron en que podría cumplir este sueño, aun estando lejos de ellos.

'Do not fear, for I am with you;
Do not anxiously look about you, for I am your God.
I will strengthen you, surely I will help you,
Surely I will uphold you with My righteous right hand.'
Isaiah 41:10 (NASV)

But those who trust the Lord
will find new strength.
They will be strong like eagles
soaring upward on wings;
they will walk and run
without getting tired.
Isaiah 40:31 (CEV)

7. References

Abbadie, C., B.K. Taylor, M.A. Peterson, and A.I. Basbaum. 1997. Differential contribution of the two phases of the formalin test to the pattern of c-fos expression in the rat spinal cord: studies with remifentanil and lidocaine. *Pain*. 69:101-110.

Abdulla, F.A., and P.A. Smith. 2001. Axotomy- and Autotomy-Induced Changes in Ca2+and K+ Channel Currents of Rat Dorsal Root Ganglion Neurons. *Journal of Neurophysiology*. 85:644-658.

Accardi, A., and C. Miller. 2004. Secondary active transport mediated by a prokaryotic homologue of ClC Cl- channels. *Nature*. 427:803-807.

Alekov, A.K., and C. Fahlke. 2009. Channel-like slippage modes in the human anion/proton exchanger ClC-4. *The Journal of general physiology*. 133:485-496.

Alexandrou, A.J., A.R. Brown, M.L. Chapman, M. Estacion, J. Turner, M.A. Mis, et al. 2016. Subtype-Selective Small Molecule Inhibitors Reveal a Fundamental Role for Nav1.7 in Nociceptor Electrogenesis, Axonal Conduction and Presynaptic Release. *Plos One*. 11.

Alloui, A., K. Zimmermann, J. Mamet, F. Duprat, J. Noël, J. Chemin, et al. 2006. TREK-1, a K+ channel involved in polymodal pain perception. *The EMBO Journal*. 25:2368-2376.

Amaya, F., Y. Izumi, M. Matsuda, and M. Sasaki. 2013. Tissue injury and related mediators of pain exacerbation. *Curr Neuropharmacol*. 11:592-597.

Aria, M.M. 2020. Chapter 1 - Bioelectricity and excitable membranes. *In* Electrophysiology Measurements for Studying Neural Interfaces. M.M. Aria, editor. Academic Press. 1-23.

Belkouch, M., M.A. Dansereau, A. Réaux-Le Goazigo, J. Van Steenwinckel, N. Beaudet, A. Chraibi, et al. 2011. The chemokine CCL2 increases Nav1.8 sodium channel activity in primary sensory neurons through a Gβγ-dependent mechanism. *J Neurosci*. 31:18381-18390.

Bennett, D.L., and C.G. Woods. 2014. Painful and painless channelopathies. *The Lancet. Neurology*. 13:587-599.

Bernal, L. 2018. Insights into the Contribution of Voltage-Gated Sodium Channel 1.7 to Paclitaxel-Induced Neuropathy. *Journal of Neuroscience*. 38:6025-6027.

Berta, T., O. Poirot, M. Pertin, R.R. Ji, S. Kellenberger, and I. Decosterd. 2008. Transcriptional and functional profiles of voltage-gated Na+ channels in injured and non-injured DRG neurons in the SNI model of neuropathic pain. *Mol Cell Neurosci*. 37:196-208.

Biber, K., and E. Boddeke. 2014. Neuronal CC chemokines: the distinct roles of CCL21 and CCL2 in neuropathic pain. *Frontiers in Cellular Neuroscience*. 8.

Blair, N.T., and B.P. Bean. 2002. Roles of tetrodotoxin (TTX)-sensitive Na+ current, TTX-resistant Na+ current, and Ca2+ current in the action potentials of nociceptive sensory neurons. *J Neurosci*. 22:10277-10290.

Borisovska, M., Y. Zhao, Y. Tsytsyura, N. Glyvuk, S. Takamori, U. Matti, et al. 2005. v-SNAREs control exocytosis of vesicles from priming to fusion. *EMBO J*. 24:2114-2126.

Borsani, G., E.I. Rugarli, M. Taglialatela, C. Wong, and A. Ballabio. 1995. Characterization of a Human and Murine Gene (CLCN3) Sharing Similarities to Voltage-Gated Chloride Channels and to a Yeast Integral Membrane Protein. *Genomics*. 27:131-141.

Bost, A., A.H. Shaib, Y. Schwarz, B.A. Niemeyer, and U. Becherer. 2017. Large dense-core vesicle exocytosis from mouse dorsal root ganglion neurons is regulated by neuropeptide Y. *Neuroscience*. 346:1-13.

Brevet, M., N. Haren, H. Sevestre, P. Merviel, and H. Ouadid-Ahidouch. 2009. DNA methylation of K(v)1.3 potassium channel gene promoter is associated with poorly

differentiated breast adenocarcinoma. *Cellular physiology and biochemistry : international journal of experimental cellular physiology, biochemistry, and pharmacology*. 24:25-32.

Brocker, D.T., and W.M. Grill. 2013. Chapter 1 - Principles of electrical stimulation of neural tissue. *In* Handbook of Clinical Neurology. Vol. 116. A.M. Lozano and M. Hallett, editors. Elsevier. 3-18.

Busserolles, J., X. Gasull, and J. Noël. 2020. Potassium Channels and Pain. *In* The Oxford Handbook of the Neurobiology of Pain. P.J.N. Wood, editor. Oxford University Press.

Cardenas, L.M., C.G. Cardenas, and R.S. Scroggs. 2001. 5HT increases excitability of nociceptor-like rat dorsal root ganglion neurons via cAMP-coupled TTX-resistant Na(+) channels. *J Neurophysiol*. 86:241-248.

Catterall, W.A. 2013. Ion Channel Protein Superfamily. *In* Encyclopedia of Biological Chemistry (Second Edition). W.J. Lennarz and M.D. Lane, editors. Academic Press, Waltham. 648-652.

Ceridono, M., S. Ory, F. Momboisse, S. Chasserot-Golaz, S. Houy, V. Calco, et al. 2011. Selective recapture of secretory granule components after full collapse exocytosis in neuroendocrine chromaffin cells. *Traffic*. 12:72-88.

Chen, T.-Y. 2004. Structure and function of ClC channels. *Annual Review of Physiology*. 67:809-839.

Cheng, H.T. 2010. Spinal cord mechanisms of chronic pain and clinical implications. *Curr Pain Headache Rep*. 14:213-220.

Christensen, E.I., O. Devuyst, G. Dom, R. Nielsen, P. Van der Smissen, P. Verroust, et al. 2003. Loss of chloride channel ClC-5 impairs endocytosis by defective trafficking of megalin and cubilin in kidney proximal tubules. *Proceedings of the National Academy of Sciences of the United States of America*. 100:8472-8477.

Clark, R.A., M. Shoaib, K.N. Hewitt, S.C. Stanford, and S.T. Bate. 2011. A comparison of InVivoStat with other statistical software packages for analysis of data generated from animal experiments. *Journal of Psychopharmacology*. 26:1136-1142.

Conner, L.B., P. Alvarez, O. Bogen, and J.D. Levine. 2016. Role of Kv4.3 in Vibration-Induced Muscle Pain in the Rat. *The Journal of Pain*. 17:444-450.

Coull, J.A.M., S. Beggs, D. Boudreau, D. Boivin, M. Tsuda, K. Inoue, et al. 2005. BDNF from microglia causes the shift in neuronal anion gradient underlying neuropathic pain. *Nature*. 438:1017-1021.

Cummins, T.R., and S.G. Waxman. 1997. Downregulation of tetrodotoxin-resistant sodium currents and upregulation of a rapidly repriming tetrodotoxin-sensitive sodium current in small spinal sensory neurons after nerve injury. *Journal of Neuroscience*. 17:3503-3514.

Cummins, T.R., S.G. Waxman, and J.N. Wood. 2019. Sodium Channels and Pain. *In* The Oxford Handbook of the Neurobiology of Pain. J.N. Wood, editor. Oxford University Press.

D'amour, F.E., and D.L. Smith. 1941. A method for determining loss of pain sensation. *J Pharmacol Exp Ther*. 72:74-79.

D'Mello, R., and A.H. Dickenson. 2008. Spinal cord mechanisms of pain. *British Journal of Anaesthesia*. 101:8-16.

Deriy, L.V., E.A. Gomez, D.A. Jacobson, X. Wang, J.A. Hopson, X.Y. Liu, et al. 2009. The Granular Chloride Channel ClC-3 Is Permissive for Insulin Secretion. *Cell Metabolism*. 10:316-323.

Devor, M. 1999. Unexplained peculiarities of the dorsal root ganglion. *Pain*. 82:S27-S35.

Dib-Hajj, S.D., T.R. Cummins, J.A. Black, and S.G. Waxman. 2010. Sodium Channels in Normal and Pathological Pain. *Annu Rev Neurosci*. 33:325-347.

Djouhri, L., and S.N. Lawson. 2004. Aβ-fiber nociceptive primary afferent neurons: a review of incidence and properties in relation to other afferent A-fiber neurons in mammals. *Brain Research Reviews*. 46:131-145.

Djouhri, L., T. Smith, A. Ahmeda, M. Alotaibi, and X. Weng. 2018. Hyperpolarization-activated cyclic nucleotide-gated channels contribute to spontaneous activity in L4 C-fiber nociceptors, but not Aβ-non-nociceptors, after axotomy of L5-spinal nerve in the rat in vivo. *Pain*. 159:1392-1402.

Djouhri, L., A. Zeidan, S.A. Abd El-Aleem, and T. Smith. 2020. Cutaneous Aβ-Non-nociceptive, but Not C-Nociceptive, Dorsal Root Ganglion Neurons Exhibit Spontaneous Activity in the Streptozotocin Rat Model of Painful Diabetic Neuropathy in vivo. *Frontiers in Neuroscience*. 14.

Du, X., and N. Gamper. 2013. Potassium channels in peripheral pain pathways: expression, function and therapeutic potential. *Curr Neuropharmacol*. 11:621-640.

Duan, K.-Z., Q. Xu, X.-M. Zhang, Z.-Q. Zhao, Y.-A. Mei, and Y.-Q. Zhang. 2012. Targeting A-type K+ channels in primary sensory neurons for bone cancer pain in a rat model. *Pain*. 153:562-574.

Dubin, A.E., and A. Patapoutian. 2010. Nociceptors: the sensors of the pain pathway. *The Journal of Clinical Investigation*. 120:3760-3772.

Dutzler, R. 2006. The ClC family of chloride channels and transporters. *Current Opinion in Structural Biology*. 16:439-446.

Emery, E.C., and P. Ernfors. 2020. Dorsal root ganglion neuron types and their functional specialization. *In* The Oxford Handbook of the Neurobiology of Pain. P.J.N. Wood, editor. Oxford University Press.

Fan, N., D.F. Donnelly, and R.H. LaMotte. 2011. Chronic compression of mouse dorsal root ganglion alters voltage-gated sodium and potassium currents in medium-sized dorsal root ganglion neurons. *Journal of neurophysiology*. 106:3067-3072.

Fang, X., L. Djouhri, J.A. Black, S.D. Dib-Hajj, S.G. Waxman, and S.N. Lawson. 2002. The Presence and Role of the Tetrodotoxin-Resistant Sodium Channel Na(v)1.9 (NaN) in Nociceptive Primary Afferent Neurons. *The Journal of Neuroscience*. 22:7425.

Favre, I., E. Moczydlowski, and L. Schild. 1995. Specificity for block by saxitoxin and divalent cations at a residue which determines sensitivity of sodium channel subtypes to guanidinium toxins. *The Journal of general physiology*. 106:203-229.

Ferrari, L.F., C.M. Lotufo, D. Araldi, M.A. Rodrigues, L.P. Macedo, S.H. Ferreira, and C.A. Parada. 2014. Inflammatory sensitization of nociceptors depends on activation of NMDA receptors in DRG satellite cells. *Proceedings of the National Academy of Sciences*. 111:18363.

Fischer, B.D., C. Ho, I. Kuzin, A. Bottaro, and M.E. O'Leary. 2017. Chronic exposure to tumor necrosis factor in vivo induces hyperalgesia, upregulates sodium channel gene expression and alters the cellular electrophysiology of dorsal root ganglion neurons. *Neuroscience Letters*. 653:195-201.

Gallego, R., I. Ivorra, and A. Morales. 1987. Effects of central or peripheral axotomy on membrane properties of sensory neurones in the petrosal ganglion of the cat. *J Physiol*. 391:39-56.

Gensch, T., V. Untiet, A. Franzen, P. Kovermann, and C. Fahlke. 2015. Determination of Intracellular Chloride Concentrations by Fluorescence Lifetime Imaging. *In* Advanced

Time-Correlated Single Photon Counting Applications. Vol. 111. B. W., editor. Springer, Cham.
Gianesello, L., M. Ceol, L. Bertoldi, L. Terrin, G. Priante, L. Murer, et al. 2020. Genetic Analyses in Dent Disease and Characterization of CLCN5 Mutations in Kidney Biopsies. *Int J Mol Sci*. 21:516.
Gilbert, D., C. Franjic-Würtz, K. Funk, T. Gensch, S. Frings, and F. Möhrlen. 2007. Differential maturation of chloride homeostasis in primary afferent neurons of the somatosensory system. *International Journal of Developmental Neuroscience*. 25:479-489.
Goldberg, Y.P., J. MacFarlane, M.L. MacDonald, J. Thompson, M.P. Dube, M. Mattice, et al. 2007. Loss-of-function mutations in the Nav1.7 gene underlie congenital indifference to pain in multiple human populations. *Clinical genetics*. 71:311-319.
Goldin, A.L., R.L. Barchi, J.H. Caldwell, F. Hofmann, J.R. Howe, J.C. Hunter, et al. 2000. Nomenclature of Voltage-Gated Sodium Channels. *Neuron*. 28:365-368.
Gosselin, R.D., C. Varela, G. Banisadr, P. Mechighel, W. Rostene, P. Kitabgi, and S. Melik-Parsadaniantz. 2005. Constitutive expression of CCR2 chemokine receptor and inhibition by MCP-1/CCL2 of GABA-induced currents in spinal cord neurones. *Journal of Neurochemistry*. 95:1023-1034.
Gradogna, A., and M. Pusch. 2010. Molecular Pharmacology of Kidney and Inner Ear CLC-K Chloride Channels. *Front Pharmacol*. 1:130-130.
Griffith, L.C. 2001. Potassium channels: The importance of transport signals. *Current Biology*. 11:R226-R228.
Gschwandtner, M., R. Derler, and K.S. Midwood. 2019. More Than Just Attractive: How CCL2 Influences Myeloid Cell Behavior Beyond Chemotaxis. *Frontiers in Immunology*. 10.
Günther, W., A. Lüchow, F. Cluzeaud, A. Vandewalle, and T.J. Jentsch. 1998. ClC-5, the chloride channel mutated in Dent's disease, colocalizes with the proton pump in endocytotically active kidney cells. *Proceedings of the National Academy of Sciences*. 95:8075.
Günther, W., N. Piwon, and T.J. Jentsch. 2003. The ClC-5 chloride channel knock-out mouse - an animal model for Dent's disease. *Pflugers Arch*. 445:456-462.
Gutman, G.A., K.G. Chandy, J.P. Adelman, J. Aiyar, D.A. Bayliss, D.E. Clapham, et al. 2003. International Union of Pharmacology. XLI. Compendium of voltage-gated ion channels: potassium channels. *Pharmacological reviews*. 55:583-586.
Guzman, R.E., A.K. Alekov, M. Filippov, J. Hegermann, and C. Fahlke. 2014. Involvement of ClC-3 chloride/proton exchangers in controlling glutamatergic synaptic strength in cultured hippocampal neurons. *Frontiers in Cellular Neuroscience*. 8.
Guzman, R.E., S. Bungert-Plümke, A. Franzen, and C. Fahlke. 2017. Preferential association with ClC-3 permits sorting of ClC-4 into endosomal compartments. *The Journal of biological chemistry*. 292:19055-19065.
Guzman, R.E., M. Grieschat, C. Fahlke, and A.K. Alekov. 2013. ClC-3 Is an Intracellular Chloride/Proton Exchanger with Large Voltage-Dependent Nonlinear Capacitance. *ACS Chemical Neuroscience*. 4:994-1003.
Guzman, R.E., E. Miranda-Laferte, A. Franzen, and C. Fahlke. 2015. Neuronal ClC-3 splice variants differ in subcellular localizations, but mediate identical transport functions. *Journal of Biological Chemistry*. 290:25851-25862.
Hains, B.C., and S.G. Waxman. 2006. Activated microglia contribute to the maintenance of chronic pain after spinal cord injury. *The Journal of neuroscience : the official journal of the Society for Neuroscience*. 26:4308-4317.

Han, C., M. Estacion, J. Huang, D. Vasylyev, P. Zhao, S.D. Dib-Hajj, and S.G. Waxman. 2015. Human Na(v)1.8: enhanced persistent and ramp currents contribute to distinct firing properties of human DRG neurons. *J Neurophysiol*. 113:3172-3185.

Herzog, R.I., T.R. Cummins, and S.G. Waxman. 2001. Persistent TTX-resistant Na+ current affects resting potential and response to depolarization in simulated spinal sensory neurons. *J Neurophysiol*. 86:1351-1364.

Hodgkin, A.L., and A.F. Huxley. 1990. A quantitative description of membrane current and its application to conduction and excitation in nerve. 1952. *Bull Math Biol*. 52:25-71; discussion 25-23.

Hoerauf, W.W., V.A. Cazares, A. Subramani, and E.L. Stuenkel. 2015. Efficient transfection of dissociated mouse chromaffin cells using small-volume electroporation. *Cytotechnology*. 67:573-583.

Hu, H., S.A. Haas, J. Chelly, H. Van Esch, M. Raynaud, A.P.M. de Brouwer, et al. 2016. X-exome sequencing of 405 unresolved families identifies seven novel intellectual disability genes. *Mol Psychiatry*. 21:133-148.

Hu, W., C. Tian, T. Li, M. Yang, H. Hou, and Y. Shu. 2009. Distinct contributions of Nav1.6 and Nav1.2 in action potential initiation and backpropagation. *Nature Neuroscience*. 12:996-1002.

Hunskaar, S., and K. Hole. 1987. The formalin test in mice: dissociation between inflammatory and non-inflammatory pain. *Pain*. 30:103-114.

IASP Task Force on Taxonomy. 1994. Part III: Pain Terms, A Current List with Definitions and Notes on Usage. *In* Classification of Chronic Pain. H. Merskey and N. Bogduk, editors. IASP Press, Seattle. 209-214.

Illias, A.M., A.C. Gist, H. Zhang, A.K. Kosturakis, and P.M. Dougherty. 2018. Chemokine CCL2 and its receptor CCR2 in the dorsal root ganglion contribute to oxaliplatin-induced mechanical hypersensitivity. *Pain*. 159:1308-1316.

Ishihara, K. 2018. External K(+) dependence of strong inward rectifier K(+) channel conductance is caused not by K(+) but by competitive pore blockade by external Na(). *The Journal of general physiology*. 150:977-989.

Jentsch, T.J., and M. Pusch. 2018. CLC Chloride Channels and Transporters: Structure, Function, Physiology, and Disease. *Physiological Reviews*. 98:1493-1590.

Jentsch, T.J., K. Steinmeyer, and G. Schwarz. 1990. Primary structure of Torpedo marmorata chloride channel isolated by expression cloning in Xenopus oocytes. *Nature*. 348:510-514.

Kaneko, H., I. Putzier, S. Frings, and T. Gensch. 2002. Determination of intracellular chloride concentration in dorsal root ganglion neurons by fluorescence lifetime imaging. *In* Current Topics in Membranes. Vol. 53. Academic Press. 167-189.

Kawasaki, E., N. Hattori, E. Miyamoto, T. Yamashita, and C. Inagaki. 1999. Single-cell RT-PCR demonstrates expression of voltage-dependent chloride channels (ClC-1, ClC-2 and ClC-3) in outer hair cells of rat cochlea. *Brain Research*. 838:166-170.

Khan, A., S. Khan, and Y.S. Kim. 2019. Insight into Pain Modulation: Nociceptors Sensitization and Therapeutic Targets. *Current drug targets*. 20:775-788.

Kim, D.S., J.O. Choi, H.D. Rim, and H.J. Cho. 2002. Downregulation of voltage-gated potassium channel α gene expression in dorsal root ganglia following chronic constriction injury of the rat sciatic nerve. *Molecular Brain Research*. 105:146-152.

Ko, E.-A., Y.-W. Kim, D. Lee, J. Choi, S. Kim, Y. Seo, et al. 2019. Expression of potassium channel genes predicts clinical outcome in lung cancer. *Korean J Physiol Pharmacol*. 23:529-537.

Komiya, H., H. Takeuchi, Y. Ogawa, Y. Hatooka, K. Takahashi, A. Katsumoto, et al. 2020. CCR2 is localized in microglia and neurons, as well as infiltrating monocytes, in the lumbar spinal cord of ALS mice. *Molecular Brain*. 13:64.

Kornak, U., D. Kasper, M.R. Bösl, E. Kaiser, M. Schweizer, A. Schulz, et al. 2001. Loss of the ClC-7 Chloride Channel Leads to Osteopetrosis in Mice and Man. *Cell*. 104:205-215.

Körner, J., J. Meents, J.-P. Machtens, and A. Lampert. 2018. β1 subunit stabilises sodium channel Nav1.7 against mechanical stress. *The Journal of physiology*. 596:2433-2445.

Lampert, A., A.O. O'Reilly, P. Reeh, and A. Leffler. 2010. Sodium channelopathies and pain. *Pflugers Arch*. 460:249-263.

Lamprecht, M.R., D.M. Sabatini, and A.E. Carpenter. 2007. CellProfiler: free, versatile software for automated biological image analysis. *BioTechniques*. 42:71-75.

Lan, X., X. Han, Q. Li, Q.-W. Yang, and J. Wang. 2017. Modulators of microglial activation and polarization after intracerebral haemorrhage. *Nat Rev Neurol*. 13:420-433.

Laumet, G., J. Garriga, S.-R. Chen, Y. Zhang, D.-P. Li, T.M. Smith, et al. 2015. G9a is essential for epigenetic silencing of K+ channel genes in acute-to-chronic pain transition. *Nature Neuroscience*. 18:1746-1755.

Lawson, S.N., and P.J. Waddell. 1991. Soma neurofilament immunoreactivity is related to cell size and fibre conduction velocity in rat primary sensory neurons. *J Physiol*. 435:41-63.

Lazarus, M.S., and Z.J. Huang. 2011. Distinct maturation profiles of perisomatic and dendritic targeting GABAergic interneurons in the mouse primary visual cortex during the critical period of ocular dominance plasticity. *J Neurophysiol*. 106:775-787.

Lein, E.S., M.J. Hawrylycz, N. Ao, M. Ayres, A. Bensinger, A. Bernard, et al. 2007. Genome-wide atlas of gene expression in the adult mouse brain. *Nature*. 445:168-176.

Lemes, J.B.P., T. de Campos Lima, D.O. Santos, A.F. Neves, F.S. de Oliveira, C.A. Parada, and C.M. da Cruz Lotufo. 2018. Participation of satellite glial cells of the dorsal root ganglia in acute nociception. *Neuroscience Letters*. 676:8-12.

Li, D.-Q., X. Jing, A. Salehi, S.C. Collins, M.B. Hoppa, A.H. Rosengren, et al. 2009. Suppression of Sulfonylurea- and Glucose-Induced Insulin Secretion In Vitro and In Vivo in Mice Lacking the Chloride Transport Protein ClC-3. *Cell Metabolism*. 10:309-315.

Li, G., X. Liu, J. Du, J. Chen, F. She, C. Wu, and C. Li. 2015. Positive shift of Nav1.8 current inactivation curve in injured neurons causes neuropathic pain following chronic constriction injury. *Mol Med Rep*. 12:3583-3590.

Li, L., S.-S. Lv, C. Wang, H. Yue, and Z.-L. Zhang. 2019a. Novel CLCN7 mutations cause autosomal dominant osteopetrosis type II and intermediate autosomal recessive osteopetrosis. *Mol Med Rep*. 19:5030-5038.

Li, T., X. Chen, C. Zhang, Y. Zhang, and W. Yao. 2019b. An update on reactive astrocytes in chronic pain. *Journal of neuroinflammation*. 16:140.

Li, X.-Y., and H. Toyoda. 2015. Role of leak potassium channels in pain signaling. *Brain Research Bulletin*. 119:73-79.

Li, Y., R.Y. North, L.D. Rhines, C.E. Tatsui, G. Rao, D.D. Edwards, et al. 2018. DRG Voltage-Gated Sodium Channel 1.7 Is Upregulated in Paclitaxel-Induced Neuropathy in Rats and in Humans with Neuropathic Pain. *The Journal of neuroscience : the official journal of the Society for Neuroscience*. 38:1124-1136.

Liddelow, S.A., K.A. Guttenplan, L.E. Clarke, F.C. Bennett, C.J. Bohlen, L. Schirmer, et al. 2017. Neurotoxic reactive astrocytes are induced by activated microglia. *Nature*. 541:481-487.

Liu, C., T.R. Cummins, L. Tyrrell, J.A. Black, S.G. Waxman, and S.D. Dib-Hajj. 2005. CAP-1A is a novel linker that binds clathrin and the voltage-gated sodium channel Na(v)1.8. *Mol Cell Neurosci*. 28:636-649.

Liu, C., Q. Li, Y. Su, and L. Bao. 2010a. Prostaglandin E2 Promotes Nav1.8 Trafficking via Its Intracellular RRR Motif Through the Protein Kinase A Pathway. *Traffic*. 11:405-417.

Liu, L., M. Oortgiesen, L. Li, and S.A. Simon. 2001. Capsaicin Inhibits Activation of Voltage-Gated Sodium Currents in Capsaicin-Sensitive Trigeminal Ganglion Neurons. *Journal of Neurophysiology*. 85:745-758.

Liu, Y., C. Schirra, L. Edelmann, U. Matti, J. Rhee, D. Hof, et al. 2010b. Two distinct secretory vesicle–priming steps in adrenal chromaffin cells. *The Journal of Cell Biology*. 190:1067.

Lloyd, S.E., S.H. Pearce, S.E. Fisher, K. Steinmeyer, B. Schwappach, S.J. Scheinman, et al. 1996. A common molecular basis for three inherited kidney stone diseases. *Nature*. 379:445-449.

Marics, I., P. Malapert, A. Reynders, S. Gaillard, and A. Moqrich. 2014. Acute heat-evoked temperature sensation is impaired but not abolished in mice lacking TRPV1 and TRPV3 channels. *PLoS One*. 9:e99828.

Maritzen, T., D.J. Keating, I. Neagoe, A.A. Zdebik, and T.J. Jentsch. 2008. Role of the Vesicular Chloride Transporter ClC-3 in Neuroendocrine Tissue. *The Journal of Neuroscience*. 28:10587.

Mathie, A., and E.L. Veale. 2009. Neuronal Potassium Channels. *In* Encyclopedia of Neuroscience. M.D. Binder, N. Hirokawa, and U. Windhorst, editors. Springer Berlin Heidelberg, Berlin, Heidelberg. 2792-2797.

McGann, J.P., J.R. Moyer, and T.H. Brown. 2001. Predominance of Late-Spiking Neurons in Layer VI of Rat Perirhinal Cortex. *The Journal of Neuroscience*. 21:4969.

McQuin, C., A. Goodman, V. Chernyshev, L. Kamentsky, B.A. Cimini, K.W. Karhohs, et al. 2018. CellProfiler 3.0: Next-generation image processing for biology. *PLOS Biology*. 16:e2005970.

Meents, J.E., E. Bressan, S. Sontag, A. Foerster, P. Hautvast, C. Rösseler, et al. 2019. The role of Nav1.7 in human nociceptors: insights from human induced pluripotent stem cell-derived sensory neurons of erythromelalgia patients. *Pain*. 160:1327-1341.

Meents, J.E., and A. Lampert. 2016. Studying Sodium Channel Gating in Heterologous Expression Systems. *In* Advanced Patch-Clamp Analysis for Neuroscientists. A. Korngreen, editor. Springer New York, New York, NY. 37-65.

Meisner, J.G., A.D. Marsh, and D.R. Marsh. 2010. Loss of GABAergic interneurons in laminae I-III of the spinal cord dorsal horn contributes to reduced GABAergic tone and neuropathic pain after spinal cord injury. *Journal of neurotrauma*. 27:729-737.

Mendell, L.M. 2014. Constructing and deconstructing the gate theory of pain. *Pain*. 155:210-216.

Menetski, J., S. Mistry, M. Lu, J.S. Mudgett, R.M. Ransohoff, J.A. DeMartino, et al. 2007. Mice overexpressing chemokine ligand 2 (CCL2) in astrocytes display enhanced nociceptive responses. *Neuroscience*. 149:706-714.

Miao, X.-R., X.-F. Gao, J.-X. Wu, Z.-J. Lu, Z.-X. Huang, X.-Q. Li, et al. 2010. Bilateral downregulation of Nav1.8 in dorsal root ganglia of rats with bone cancer pain induced by inoculation with Walker 256 breast tumor cells. *BMC Cancer*. 10:216.

Mika, J., M. Zychowska, K. Popiolek-Barczyk, E. Rojewska, and B. Przewlocka. 2013. Importance of glial activation in neuropathic pain. *European journal of pharmacology*. 716:106-119.

Mohammad-Panah, R., R. Harrison, S. Dhani, C. Ackerley, L.J. Huan, Y. Wang, and C.E. Bear. 2003. The chloride channel ClC-4 contributes to endosomal acidification and trafficking. *The Journal of biological chemistry*. 278:29267-29277.

Moore, K.A., T. Kohno, L.A. Karchewski, J. Scholz, H. Baba, and C.J. Woolf. 2002. Partial Peripheral Nerve Injury Promotes a Selective Loss of GABAergic Inhibition in the Superficial Dorsal Horn of the Spinal Cord. *The Journal of Neuroscience*. 22:6724.

Moulin, P., T. Igarashi, P. Van Der Smissen, J.-P. Cosyns, P. Verroust, R.V. Thakker, et al. 2003a. Altered polarity and expression of H^+-ATPase without ultrastructural changes in kidneys of Dent's disease patients. *Kidney International*. 63:1285-1295.

Moulin, P., T. Igarashi, P. Van der Smissen, J.P. Cosyns, P. Verroust, R.V. Thakker, et al. 2003b. Altered polarity and expression of H+-ATPase without ultrastructural changes in kidneys of Dent's disease patients. *Kidney Int*. 63:1285-1295.

Ogura, T., T. Furukawa, T. Toyozaki, K. Yamada, Y.-J. Zheng, Y. Katayama, et al. 2002. ClC-3B, a novel ClC-3 splicing variant that interacts with EBP50 and facilitates expression of CFTR-regulated ORCC. *The FASEB Journal*. 16:863-865.

Oh, U., and J. Jung. 2020. Chloride Channels in Nociceptors. *In* The Oxford Handbook of the Neurobiology of Pain. P.J.N. Wood, editor. Oxford University Press.

Okamoto, F., H. Kajiya, K. Toh, S. Uchida, M. Yoshikawa, S. Sasaki, et al. 2008. Intracellular ClC-3 chloride channels promote bone resorption in vitro through organelle acidification in mouse osteoclasts. *American Journal of Physiology-Cell Physiology*. 294:C693-C701.

Okkenhaug, H., K.H. Weylandt, D. Carmena, D.J. Wells, C.F. Higgins, and A. Sardini. 2006. The human ClC‐4 protein, a member of the CLC chloride channel/transporter family, is localized to the endoplasmic reticulum by its N‐terminus. *The FASEB Journal*. 20:2390-2392.

Okuse, K., M. Malik-Hall, M.D. Baker, W.Y. Poon, H. Kong, M.V. Chao, and J.N. Wood. 2002. Annexin II light chain regulates sensory neuron-specific sodium channel expression. *Nature*. 417:653-656.

Padilla, F., M.-L. Couble, B. Coste, F. Maingret, N. Clerc, M. Crest, et al. 2007. Expression and localization of the Nav1.9 sodium channel in enteric neurons and in trigeminal sensory endings: Implication for intestinal reflex function and orofacial pain. *Mol Cell Neurosci*. 35:138-152.

Palmer, E.E., T. Stuhlmann, S. Weinert, E. Haan, H. Van Esch, M. Holvoet, et al. 2018. De novo and inherited mutations in the X-linked gene CLCN4 are associated with syndromic intellectual disability and behavior and seizure disorders in males and females. *Mol Psychiatry*. 23:222-230.

Pan, J., X.J. Lin, Z.H. Ling, and Y.Z. Cai. 2015. Effect of down-regulation of voltage-gated sodium channel Nav1.7 on activation of astrocytes and microglia in DRG in rats with cancer pain. *Asian Pacific journal of tropical medicine*. 8:405-411.

Pang, R.-P., M.-X. Xie, J. Yang, K.-F. Shen, X. Chen, Y.-X. Su, et al. 2016. Downregulation of ClC-3 in dorsal root ganglia neurons contributes to mechanical hypersensitivity following peripheral nerve injury. *Neuropharmacology*. 110:181-189.

Pedersen, T.H., A. Riisager, F.V. de Paoli, T.-Y. Chen, and O.B. Nielsen. 2016. Role of physiological ClC-1 Cl- ion channel regulation for the excitability and function of working skeletal muscle. *The Journal of general physiology*. 147:291-308.

Peters, C.M., and J.C. Eisenach. 2010. Contribution of the chemokine (C-C motif) ligand 2 (CCL2) to mechanical hypersensitivity after surgical incision in rats. *Anesthesiology*. 112:1250-1258.

Picollo, A., and M. Pusch. 2005. Chloride/proton antiporter activity of mammalian CLC proteins ClC-4 and ClC-5. *Nature*. 436:420-423.

Piwon, N., W. Günther, M. Schwake, M.R. Bösl, and T.J. Jentsch. 2000. ClC-5 Cl--channel disruption impairs endocytosis in a mouse model for Dent's disease. *Nature*. 408:369-373.

Poët, M., U. Kornak, M. Schweizer, A.A. Zdebik, O. Scheel, S. Hoelter, et al. 2006. Lysosomal storage disease upon disruption of the neuronal chloride transport protein ClC-6. *Proceedings of the National Academy of Sciences*. 103:13854.

Polgár, E., S. Gray, J.S. Riddell, and A.J. Todd. 2004. Lack of evidence for significant neuronal loss in laminae I–III of the spinal dorsal horn of the rat in the chronic constriction injury model. *Pain*. 111.

Polovitskaya, M.M., C. Barbini, D. Martinelli, F.L. Harms, F.S. Cole, P. Calligari, et al. 2020. A Recurrent Gain-of-Function Mutation in CLCN6, Encoding the ClC-6 Cl−/H+-Exchanger, Causes Early-Onset Neurodegeneration. *The American Journal of Human Genetics*. 107:1062-1077.

Priestley, J.V. 2009. Neuropeptides: Sensory Systems. *In* Encyclopedia of Neuroscience. L.R. Squire, editor. Academic Press, Oxford. 935-943.

Ramahi, A.A., and R.L. Ruff. 2014. Membrane Potential. *In* Encyclopedia of the Neurological Sciences (Second Edition). M.J. Aminoff and R.B. Daroff, editors. Academic Press, Oxford. 1034-1035.

Rasband, M.N., E.W. Park, T.W. Vanderah, J. Lai, F. Porreca, and J.S. Trimmer. 2001. Distinct potassium channels on pain-sensing neurons. *Proceedings of the National Academy of Sciences*. 98:13373.

Ren, K., and R. Dubner. 2008. Neuron-glia crosstalk gets serious: role in pain hypersensitivity. *Curr Opin Anaesthesiol*. 21:570-579.

Riazanski, V., L.V. Deriy, P.D. Shevchenko, B. Le, E.A. Gomez, and D.J. Nelson. 2011. Presynaptic CLC-3 determines quantal size of inhibitory transmission in the hippocampus. *Nature Neuroscience*. 14:487-494.

Rickheit, G., L. Wartosch, S. Schaffer, S.M. Stobrawa, G. Novarino, S. Weinert, and T.J. Jentsch. 2010. Role of ClC-5 in renal endocytosis is unique among ClC exchangers and does not require PY-motif-dependent ubiquitylation. *The Journal of biological chemistry*. 285:17595-17603.

Rueden, C.T., J. Schindelin, M.C. Hiner, B.E. DeZonia, A.E. Walter, E.T. Arena, and K.W. Eliceiri. 2017. ImageJ2: ImageJ for the next generation of scientific image data. *BMC Bioinformatics*. 18:529.

Rush, A.M., T.R. Cummins, and S.G. Waxman. 2007. Multiple sodium channels and their roles in electrogenesis within dorsal root ganglion neurons. *J Physiol-London*. 579:1-14.

Schindelin, J., I. Arganda-Carreras, E. Frise, V. Kaynig, M. Longair, T. Pietzsch, et al. 2012. Fiji: an open-source platform for biological-image analysis. *Nature Methods*. 9:676-682.

Seitz, V., P. Stötzner, D. Labuz, and H. Machelska. 2021. Patch Clamp Analysis of Opioid-Induced Kir3 Currents in Mouse Peripheral Sensory Neurons Following Nerve Injury. *In* Opioid Receptors: Methods and Protocols. S.M. Spampinato, editor. Springer US, New York, NY. 127-137.

Simon, D.B., R.S. Bindra, T.A. Mansfield, C. Nelson-Williams, E. Mendonca, R. Stone, et al. 1997. Mutations in the chloride channel gene, CLCNKB, cause Bartter's syndrome type III. *Nature genetics*. 17:171-178.

Sleeper, A.A., T.R. Cummins, S.D. Dib-Hajj, W. Hormuzdiar, L. Tyrrell, S.G. Waxman, and J.A. Black. 2000. Changes in Expression of Two Tetrodotoxin-Resistant Sodium Channels and Their Currents in Dorsal Root Ganglion Neurons after Sciatic Nerve Injury But Not Rhizotomy. *The Journal of Neuroscience*. 20:7279.

Smith, A.J., and J.D. Lippiat. 2010. Direct endosomal acidification by the outwardly rectifying CLC-5 Cl(-)/H(+) exchanger. *J Physiol*. 588:2033-2045.

Smith, A.J., A.A. Reed, N.Y. Loh, R.V. Thakker, and J.D. Lippiat. 2009. Characterization of Dent's disease mutations of CLC-5 reveals a correlation between functional and cell biological consequences and protein structure. *American journal of physiology. Renal physiology*. 296:F390-397.

Stauber, T., and T.J. Jentsch. 2010. Sorting Motifs of the Endosomal/Lysosomal CLC Chloride Transporters*. *Journal of Biological Chemistry*. 285:34537-34548.

Steinmeyer, K., B. Schwappach, M. Bens, A. Vandewalle, and T.J. Jentsch. 1995. Cloning and functional expression of rat CLC-5, a chloride channel related to kidney disease. *The Journal of biological chemistry*. 270:31172-31177.

Stemkowski, P.L., and P.A. Smith. 2012. Long-term IL-1β exposure causes subpopulation-dependent alterations in rat dorsal root ganglion neuron excitability. *J Neurophysiol*. 107:1586-1597.

Stobrawa, S.M., T. Breiderhoff, S. Takamori, D. Engel, M. Schweizer, A.A. Zdebik, et al. 2001. Disruption of ClC-3, a Chloride Channel Expressed on Synaptic Vesicles, Leads to a Loss of the Hippocampus. *Neuron*. 29:185-196.

Stockklausner, C., and N. Klöcker. 2003. Surface Expression of Inward Rectifier Potassium Channels Is Controlled by Selective Golgi Export *. *Journal of Biological Chemistry*. 278:17000-17005.

Stucky, C.L. 2007. IB4-Positive Neurons, Role in Inflammatory Pain. *In* Encyclopedia of Pain. R.F. Schmidt and W.D. Willis, editors. Springer Berlin Heidelberg, Berlin, Heidelberg. 952-955.

Suaudeau, C., J.-C. do-Rego, and J. Costentin. 2005. Modifications in avoidance reactions of mice, on a second exposure to the hot plate, resist to various amnesia-inducing treatments. *Cognitive Brain Research*. 25:339-347.

Sugiura, Y., C.L. Lee, and E.R. Perl. 1986. Central projections of identified, unmyelinated (C) afferent fibers innervating mammalian skin. *Science*. 234:358.

Suzuki, T., T. Rai, A. Hayama, E. Sohara, S. Suda, T. Itoh, et al. 2006. Intracellular localization of ClC chloride channels and their ability to form hetero-oligomers. *Journal of cellular physiology*. 206:792-798.

Swanwick, R.S., A. Pristerá, and K. Okuse. 2010. The trafficking of Na(V)1.8. *Neuroscience letters*. 486:78-83.

Tan, C.-Y., Y.-P. Wang, Y.-Y. Han, B.-H. Lu, W. Ji, L.-C. Zhu, et al. 2020. Expression and effect of sodium-potassium-chloride cotransporter on dorsal root ganglion neurons in a rat model of chronic constriction injury. *Neural Regen Res*. 15:912-921.

Tan, Z.Y., D.F. Donnelly, and R.H. LaMotte. 2006. Effects of a chronic compression of the dorsal root ganglion on voltage-gated Na+ and K+ currents in cutaneous afferent neurons. *J Neurophysiol*. 95:1115-1123.

Taoufiq, Z., M. Ninov, A. Villar-Briones, H.Y. Wang, T. Sasaki, M.C. Roy, et al. 2020. Hidden proteome of synaptic vesicles in the mammalian brain. *Proceedings of the National Academy of Sciences of the United States of America*. 117:33586-33596.

Taylor, B.K., M.A. Peterson, and A.I. Basbaum. 1995. Persistent cardiovascular and behavioral nociceptive responses to subcutaneous formalin require peripheral nerve input. *J Neurosci*. 15:7575-7584.

Thacker, M.A., A.K. Clark, T. Bishop, J. Grist, P.K. Yip, L.D. Moon, et al. 2009. CCL2 is a key mediator of microglia activation in neuropathic pain states. *Eur J Pain*. 13:263-272.

Thakker, R.V. 1998. Chloride channel mutations in hypercalciuric kidney stone disease. *Clinical and Experimental Nephrology*. 2:194-198.

Tjølsen, A., O.-G. Berge, S. Hunskaar, J.H. Rosland, and K. Hole. 1992. The formalin test: an evaluation of the method. *Pain*. 51.

Todd, A., and F. Wang. 2020. Central Nervous System Pain Pathways. *In* The Oxford Handbook of the Neurobiology of Pain. P.J.N. Wood, editor. Oxford University Press.

Tripathy, S.J., and R.C. Gerkin. 2013. NeuroElectro Project. *In* Encyclopedia of Computational Neuroscience. D. Jaeger and R. Jung, editors. Springer New York, New York, NY. 1-3.

Tsantoulas, C., and S.B. McMahon. 2014. Opening paths to novel analgesics: the role of potassium channels in chronic pain. *Trends in neurosciences*. 37:146-158.

Usoskin, D., A. Furlan, S. Islam, H. Abdo, P. Lönnerberg, D. Lou, et al. 2015. Unbiased classification of sensory neuron types by large-scale single-cell RNA sequencing. *Nat Neurosci*. 18:145-153.

Vainchtein, I.D., G. Chin, F.S. Cho, K.W. Kelley, J.G. Miller, E.C. Chien, et al. 2018. Astrocyte-derived interleukin-33 promotes microglial synapse engulfment and neural circuit development. *Science*. 359:1269-1273.

Vallejo, R., D.M. Tilley, L. Vogel, and R. Benyamin. 2010. The role of glia and the immune system in the development and maintenance of neuropathic pain. *Pain practice : the official journal of World Institute of Pain*. 10:167-184.

Veeramah, K.R., L. Johnstone, T.M. Karafet, D. Wolf, R. Sprissler, J. Salogiannis, et al. 2013. Exome sequencing reveals new causal mutations in children with epileptic encephalopathies. *Epilepsia*. 54:1270-1281.

Vydyanathan, A., Z.Z. Wu, S.R. Chen, and H.L. Pan. 2005. A-type voltage-gated K+ currents influence firing properties of isolectin B4-positive but not isolectin B4-negative primary sensory neurons. *J Neurophysiol*. 93:3401-3409.

Wacker, M.J., and M.P. Godard. 2005. Analysis of One-Step and Two-Step Real-Time RT-PCR Using SuperScript III. *Journal of Biomolecular Techniques : JBT*. 16:266-271.

Walker, J.M. 1996. The Bicinchoninic Acid (BCA) Assay for Protein Quantitation. *In* The Protein Protocols Handbook. J.M. Walker, editor. Humana Press, Totowa, NJ. 11-14.

Wang, C.-H., L.-J. Zou, Y.-L. Zhang, Y.-F. Jiao, and J.-H. Sun. 2010. The excitatory effects of the chemokine CCL2 on DRG somata are greater after an injury of the ganglion than after an injury of the spinal or peripheral nerve. *Neuroscience Letters*. 475:48-52.

Wang, J.-G., J.A. Strong, W. Xie, and J.-M. Zhang. 2007. Local inflammation in rat dorsal root ganglion alters excitability and ion currents in small-diameter sensory neurons. *Anesthesiology*. 107:322-332.

Wang, X.Q., L.V. Deriy, S. Foss, P. Huang, F.S. Lamb, M.A. Kaetzel, et al. 2006. CLC-3 Channels Modulate Excitatory Synaptic Transmission in Hippocampal Neurons. *Neuron*. 52:321-333.

Weinert, S., N. Gimber, D. Deuschel, T. Stuhlmann, D. Puchkov, Z. Farsi, et al. 2020. Uncoupling endosomal CLC chloride/proton exchange causes severe neurodegeneration. *The EMBO Journal*. 39:e103358.

Wood, J.N. 2008. 5.07 - Sodium Channels. *In* The Senses: A Comprehensive Reference. R.H. Masland, T.D. Albright, T.D. Albright, R.H. Masland, P. Dallos, D. Oertel, S. Firestein, G.K. Beauchamp, M. Catherine Bushnell, A.I. Basbaum, J.H. Kaas, and E.P. Gardner, editors. Academic Press, New York. 89-95.

Wright, J., M.M. Morales, J. Sousa-Menzes, D. Ornellas, J. Sipes, Y. Cui, et al. 2008. Transcriptional adaptation to Clcn5 knockout in proximal tubules of mouse kidney. *Physiological Genomics*. 33:341-354.

Xie, R.-G., Y.-J. Gao, C.-K. Park, N. Lu, C. Luo, W.-T. Wang, et al. 2018. Spinal CCL2 Promotes Central Sensitization, Long-Term Potentiation, and Inflammatory Pain via CCR2: Further Insights into Molecular, Synaptic, and Cellular Mechanisms. *Neuroscience Bulletin*. 34:13-21.

Xu, G.-Y., J.H. Winston, M. Shenoy, H. Yin, and P.J. Pasricha. 2006. Enhanced excitability and suppression of A-type K+ current of pancreas-specific afferent neurons in a rat model of chronic pancreatitis. *American Journal of Physiology-Gastrointestinal and Liver Physiology*. 291:G424-G431.

Yang, Y., J. Huang, M.A. Mis, M. Estacion, L. Macala, P. Shah, et al. 2016. Nav1.7-A1632G Mutation from a Family with Inherited Erythromelalgia: Enhanced Firing of Dorsal Root Ganglia Neurons Evoked by Thermal Stimuli. *The Journal of Neuroscience*. 36:7511.

Yeomans, D.C., and H.K. Proudfit. 1996. Nociceptive responses to high and low rates of noxious cutaneous heating are mediated by different nociceptors in the rat: electrophysiological evidence. *Pain*. 68.

Yoshikawa, M., S. Uchida, J. Ezaki, T. Rai, A. Hayama, K. Kobayashi, et al. 2002. CLC-3 deficiency leads to phenotypes similar to human neuronal ceroid lipofuscinosis. *Genes to Cells*. 7:597-605.

Zhao, J., M.E. O'Leary, and M. Chahine. 2011. Regulation of Nav1.6 and Nav1.8 peripheral nerve Na+ channels by auxiliary β-subunits. *Journal of Neurophysiology*. 106:608-619.

Zhao, Z., X. Li, J. Hao, J.H. Winston, and S.A. Weinman. 2007. The ClC-3 chloride transport protein traffics through the plasma membrane via interaction of an N-terminal dileucine cluster with clathrin. *The Journal of biological chemistry*. 282:29022-29031.

Zhu, X., S. Cao, M.D. Zhu, J.Q. Liu, J.J. Chen, and Y.J. Gao. 2014. Contribution of chemokine CCL2/CCR2 signaling in the dorsal root ganglion and spinal cord to the maintenance of neuropathic pain in a rat model of lumbar disc herniation. *The journal of pain : official journal of the American Pain Society*. 15:516-526.

8. Publications

During my Ph.D. studies I contributed to the following peer-reviewed publications:

Maddalena Comini*, **Juan Sierra-Marquez***, Gustavo A. Guzman, Arne Franzen, Antje Willuweit, Patricia Hidalgo, Christoph Fahlke, Raul E. Guzman. **CLC anion/proton exchangers regulate secretory vesicle filling and maturation in chromaffin cells**. Submitted to *EMBO reports*, in revision.

* These authors contributed equally

Author´s contribution statement: I contributed to the patch-clamp measurements, depolarization, and high K^+-induced secretion and amperometric experiments and analyzed the data.

2. He, Hailan; Guzman, Raul E; Cao, Dezhi; **Sierra-Marquez, Juan**; Yin, Fei; Fahlke, Christoph; Peng, Jing; Stauber, Tobias. **The molecular and phenotypic spectrum of CLCN4-related epilepsy**. Submitted to *Epilepsia,* in revision.

Author´s contribution statement: I contributed to the confocal colocalization experiments.

9. Abbreviations

CCD	Chronic compression of the DRG
CCI	Chronic constriction injury
CCL2	C-C Motif Chemokine Ligand 2
CCR2	C-C Motif Chemokine receptor 2
CGRP	Calcitonin gene-related peptide
CNS	Central nervous system
DHSC	Dorsal horn of the spinal cord
DRG	Dorsal root ganglia
GABA	Gamma aminobutyric acid
IB4	Isolectin B4
IL	Interleukin
KCC2	Potassium-chloride cotransporter 2
LAMP1	Lysosomal-associated membrane protein 1
LANUV	Landesamt für Natur, Umwelt und Verbraucherschutz
LDCV	Large-dense core vesicles
mEPSPs	Miniature excitatory postsynaptic potentials
mIPSC	Miniature inhibitory postsynaptic currents
NBA	Neurobasal medium
NCL	Neuronal ceroid lipofuscinosis
NHE3	Sodium/proton exchanger 3
NKCC1	Sodium-potassium-chloride cotransporter 1
NMDA	N-methyl-D-aspartate
NPT2a	Sodium/phosphate cotransporter 2a
PAG	Periaqueductal gray
PNS	Peripheral nervous system
PVDF	Polyvinylidene fluoride
RAB11	Ras-related protein 11
SNI	Spared nerve injury
TEMED	N,N,N′,N′-Tetramethylethylenediamine
TfR	Transferrin receptor
TRP	Transient receptor potential cation channel
TRPV1	Transient receptor potential cation channel subfamily Vanilloid member 1
TTX-R	Tetrodotoxin resistance
TTX-S	Tetrodotoxin sensitive
URIDINE	1-ß-D-Ribofuranosyluracil, Uracil-1-ß-Dribofuranoside
VAMP3	Vesicle-associated membrane protein 3
VAMP4	Vesicle-associated membrane protein 4
VGSC	Voltage-gated sodium channels

Eidesstattliche Versicherung

Ich versichere an Eides statt, dass die Dissertation von mir selbstständig und ohne unzulässige fremde Hilfe unter Beachtung der „Grundsätze zur Sicherung guter wissenschaftlicher Praxis an der Heinrich-Heine-Universität Düsseldorf“ erstellt worden ist.

Jülich, März 2021 Juan David Sierra Marquez